ÇUKUROVA UNIVERSITY
INSTITUTE OF NATURAL AND APPLIED SCIENCES

PhD THESIS

Mehmet Oğuz TAŞCI

THE GROUND EFFECT ON THE VORTICAL FLOW FORMATION AND THE AERODYNAMIC CHARACTERISTICS OF SLENDER AND DOUBLE DELTA WINGS

DEPARTMENT OF MECHANICAL ENGINEERING

ADANA-2022

ÇUKUROVA UNIVERSITY
INSTITUTE OF NATURAL AND APPLIED SCIENCE

THE GROUND EFFECT ON THE VORTICAL FLOW FORMATION AND THE AERODYNAMIC CHARACTERISTICS OF SLENDER AND DOUBLE DELTA WINGS

Mehmet Oğuz TAŞCI

PhD THESIS

DEPARTMENT OF MECHANICAL ENGINEERING

We certify that the thesis titled above was reviewed and approved for the award of the degree of the Philosophy of Doctorate by the board of jury on 30/03/2022.

………………………	………………………......	…………………………….........
Prof. Dr. Beşir ŞAHİN	Prof. Dr. Hüseyin AKILLI	Assoc.Prof. Dr. Bülent YANIKTEPE
SUPERVISOR	MEMBER	MEMBER
………………..............................	……………………………………..	
Assoc. Prof. Dr. Çetin CANPOLAT	Assoc. Prof. Dr. Tahir DURHASAN	
MEMBER	MEMBER	

PhD Thesis is written at the Department of Mechanical Engineering, Institute of Natural and AppliedSciences of Çukurova University.
Registration Number:

Prof. Dr. Sadık DİNÇER
Director
Institute of Natural and Applied Sciences

This study is supported by Çukurova University Scientific Research Project Unit.
Project no: FDK-2019-11368

ABSTRACT

PhD THESIS

THE GROUND EFFECT ON THE VORTICAL FLOW FORMATION AND THE AERODYNAMIC CHARACTERISTICS OF SLENDER AND DOUBLE DELTA WINGS

Mehmet Oğuz TAŞCI

ÇUKUROVA UNIVERSITY
INSTITUTE OF NATURAL AND APPLIED SCIENCES
DEPARTMENT OF MECHANICAL ENGINEERING

Supervisor : Prof. Dr. Beşir ŞAHİN
Year: 2022, Pages: 131
Jury : Prof. Dr. Beşir ŞAHİN
: Prof. Dr. Hüseyin AKILLI
: Assoc. Prof. Dr. Bülent YANIKTEPE
: Assoc. Prof. Dr. Çetin CANPOLAT
: Assoc. Prof. Dr. Tahir DURHASAN

The ground effect (GE) on the formation of the vortical flow over a slender and a double delta wing having a sweep angle of Λ=70° and 70°/40° was examined using Particle Image Velocimetry (PIV) and dye flow visualization methods in this study. Qualitatively and quantitatively measured results are shown for angles of attack, α=15° and 25° for double delta wing, and α=25° and 35° for slender delta wing in the side and cross-flow planes to reveal the details of the flow structure. The distance, *h* between the surfaces of the ground and the delta wing, which is normalized with the chord length of the double delta wing, *c*, was selected as *h/c*=0.1, 0.25 0.55, and the ground-free case (GFE). Also, the experiments were conducted at the chordwise location over the cross-flow plane at *x/c*=0.8 which was normalized with the chord length of the double delta wing, *c*. The Reynolds number was set as $Re=2\text{x}10^4$ for dye visualization and PIV experiments. For the experiments in the wind tunnel, the Reynolds number was taken as $Re=1\text{x}10^5$ within the various angles of attack 5°≤α≤45° and ground distances from GFE to *h/c*=0.55, 0.25, 0.10. The results demonstrate that the magnitudes of the vortices progressively diminish when the delta wing moves from the free-stream flow region into the boundary layer region close to the ground surface, *h/c*=0.1. The efficiency of the wing aerodynamics is positively affected by its closeness to the ground due to the dynamic air cushion.

Key Words: Aerodynamic Coefficients, Delta Wing, Ground Effect, Particle Image Velocimetry, Vortex Breakdown

ÖZ

DOKTORA TEZİ

YERİN NARİN VE DUBLE DELTA KANAT ÜZERİNDE OLUŞAN GİRDAPLI AKIŞ YAPISINA VE AERODİNAMİK KARAKTERİSTİĞİNE ETKİSİ

Mehmet Oğuz TAŞCI

ÇUKUROVA ÜNİVERSİTESİ
FEN BİLİMLERİ ENSTİTÜSÜ
MAKİNE MÜHENDİSLİĞİ ANABİLİM DALI

Danışman	: Prof. Dr. Beşir ŞAHİN
	Yıl: 2022, Sayfa: 131
Jüri	: Prof. Dr. Beşir ŞAHİN
	: Prof. Dr. Hüseyin AKILLI
	: Doç. Dr. Bülent YANIKTEPE
	: Doç. Dr. Çetin CANPOLAT
	: Doç. Dr. Tahir DURHASAN

Bu çalışmada, tarama açısı Λ=70° ve 70°/40° olan narin ve duble delta kanat üzerinde girdaplı akışın oluşumundaki zemin etkisi Parçacık Görüntülemeli Hız Ölçme (PIV) ve boya ile akış görselleştirme yöntemleri kullanılarak incelenmiştir. Akış fiziğinin ayrıntılarını ortaya çıkarmak için hücum açıları, duble delta kanat için α=15° ve 25°, ve narin delta kanat için α=25° ve 35° olarak ayarlanmış ve kanat yan ve arka düzlemi boyunca nitel ve nicel olarak ölçülmüş sonuçlar gösterilmiştir. Narin ve duble delta kanatların kiriş uzunluğu, *c* ile normalize edilmiş olan, delta kanat ile zemin yüzeyleri arasındaki mesafe *h/c*=0,1, 0,25 0,55 ve zemin etkisi dışındaki durumlar şeklinde seçilmiştir. Ayrıca deneyler, kanat arka düzlemi üzerinde, duble delta kanadın kiriş uzunluğu ile normalize edilmiş olan *x/c*=0.8'de gerçekleştirilmiştir. Boya görselleştirme ve PIV deneyleri için Reynolds sayısı $Re=2\mathrm{x}10^4$ olarak belirlenmiştir. Rüzgâr tünelinde yapılan deneylerde, $5°\leq\alpha\leq45°$ hücum açıları ve yer etkisiz bölgeden *h/c*=0.55, 0.25, 0.10'a kadar olan yer mesafelerinde Reynolds sayısı, $Re=1\mathrm{x}10^5$ olarak alınmıştır. Sonuçlar, narin ve duble delta kanatlar yer etkisi olmayan bölgeden *h/c*=0.1'e yerleşene kadar hareket ettirilğinde girdapların büyüklüklerinin giderek azaldığını göstermektedir. Kanat aerodinamiğinin verimliliği, dinamik hava yastığı etkisi nedeniyle zemine yaklaşımdan olumlu yönde etkilenir.

Anahtar Kelimeler: Aerodinamik Katsayılar, Delta Kanat, Girdap Çökmesi, Parçacık Görüntülemeli Hız Ölçme Tekniği, Yer Etkisi

EXPANDED ABSTRACT

Delta wings, especially used in high-speed aircraft, are advantageous in terms of both structural and aerodynamics. In addition, the shock waves generated on the nose of the aircraft remain under the leading edge of the delta wing, and due to the structure of the wingtip vortices on the delta wing, the delta wings with high sweep angle, Λ can reach high angles of attack, α. Because of the efficient design structure of the delta wing, the low air friction at high speeds allows the delta wing to move faster and have a higher lift capacity. One of the most important features distinguishing delta-wing aircraft from classic backward swept and rectangular wing airplanes are that there is no slope between the wing and the body. In this wing design, since the speed of the airflow traveling on the delta wing is not more than the speed of the delta wing, the resulting air friction is low. This allows the aircraft to move at higher speeds and higher lift capacity. The shock wave in free-flow occurs when the exceeded speed of sound causes the friction force acting on the wings to increase significantly. The reason why delta wings are mostly preferred in aircraft that can move faster than sound is that they are less affected by the increase in air friction due to the sound wall formed when the aircraft is at sound speed. In other words, it has a very efficient structure for high speeds. This causes an increase in the interest in the delta wings. Another advantage of the structure of the delta wing is that it provides high payload capacity for delta-wing aircraft. Since the delta wing is attached to the body from a long area, it becomes much more robust and durable than the body structure. Since the surface area of the delta wing is integrated with the body, it can have plenty of weapon payload capacity.

The most fundamental difference between slender and non-slender delta wings is the sweep angle. The difference in the sweep angle aerodynamically affects the maneuvering capabilities and operating conditions of the delta wings. For example, slender wings can be operated at high angles of attack and high speeds. However, the non-slender delta wings are suitable for flying at moderate

angles of attack. Also, the slender wings can achieve high lift coefficients at high angles of attack while the non-slender delta wings can reach the maximum lift at low and moderate angles of attack. In addition, the maximum angle of attack to the stall region differs between the slender and the non-slender delta wings. For example, the maximum angle of attack for a non-slender delta wing having Λ=40° before the stall zone is 17° indicated by Tumse et al. (2021), while it is 33° for a slender wing having Λ=70° conducted by Tasci et al. (2020). Another difference between the slender and the non-slender delta wings is the area covered by the leading-edge vortex (LEV) on the wing surface. Although the primary vortices are more rounded and smaller on a slender wing, the primary vortices spread over a wider area on a non-slender delta wing at the same angle of attack as indicated by Lee and Ko (2016). In general, it can be seen that these two delta wing configurations are very different in terms of aerodynamics and flow physics.

It is necessary to investigate the ground effect and how it affects these cases. This phenomenon is often described as "better flying ability". If this phenomenon is needed to describe briefly, it can be explained as: the delta wing starts to descend, but the speed to land is higher than required. When the aircraft enters the ground effect on landing, a lifting condition called "air cushioning" is encountered. The ground effect is strongest in the range of a wingspan above the ground, and the ground effect increases when the proximity to the ground increases. The ground effect causes the lift force, F_L to increase while reducing the drag force, F_D. The main factor in the occurrence of the ground effect is the air vortices formed on the wingtips. The ground effect restricts upwash/downwash and wingtip vortices around the aircraft. As the aircraft approaches the ground, the structural formation of the vortices is also affected. In other words, when the delta wing approaches the ground, the leading-edge vortices at the wingtips cannot grow as much as they are in the free-flow. The reason for this is that the ground prevents the formation of the downstream of the flow. The flow around the delta wing is constantly rotating, but this rotation cannot be completed as the flow hits the ground. The pressure under the delta wing is higher than above, and this creates lifting. The strengthening of the lifting is caused by the interaction between the flow and the wing's surface increases because of the ground effect. Dynamic air cushion is the increase in the gradient of the adverse pressure on the bottom of the delta wing through the chordwise direction because of the air stagnation in the area between the ground surface and the delta wing. Thus, it is seen that the impact of the dynamic air cushion causes the lifting to increase.

The current study qualitatively and quantitatively investigates the vortical flow formation developed over the slender and double delta wings having Λ=70° and Λ=70°/40° under the ground effect (GE) with the change of the ground distance, *h/c*. In this context, the Particle Image Velocimetry (PIV) and dye visualization methods in the water channel and the aerodynamic force measurement in the wind tunnel were carried out. As a result, the aerodynamic features and the vortical flow structures over the delta wing considerably alter due to the intensity of the interaction between the delta wing and the flow over the ground surface. Thus, it is identically vital to survey the ground effect on the aerodynamic features of the delta wing during the take-off and landing positions. Qualitatively and quantitatively measured results are shown for angles of attack, α=15° and 25° for double delta wing, and α=25° and 35° for slender delta wing in the side and cross-flow planes to reveal the details of the flow structure. The distance, *h* between the surfaces of the ground and the delta wing, which is normalized with the chord length of the delta wing, *c*, was selected as *h/c*=0.1, 0.25 0.55, and the ground-free effect (GFE) case. Also, the experiments were conducted at the chordwise location over the cross-flow plane at *x/c*=0.8 which was normalized with the chord length of the delta wing, *c*. The Reynolds number was set as $Re=2x10^4$ for dye visualization and PIV experiments. For the experiments in the wind tunnel, the Reynolds number was taken as $Re=1x10^5$ within the various angles of attack 5°≤α≤45° and ground distances from GFE to *h/c*=0.55, 0.25, 0.10.

This study examined the ground effect on the vortical flow structures over a 70-deg-swept slender delta wing qualitatively and quantitatively using dye flow visualization and Particle Image Velocimetry techniques. The measurements with dye visualization and PIV methods were conducted in the plan-view, side-view, and end-view planes with the angles of attack of α=25° and 35°. Also, the experiments were performed at a normalized chordwise location of x/c=0.8 over the end-view plane. The results demonstrate that leading-edge vortices magnitudes progressively diminish when the delta wing moves from the ground-free effect region until the wing location, h/c=0.1. Also, the rate of inboard flow from the side leading edge towards the central axis of the wing gets higher by the influence of the ground over the suction surface of the delta wing. When the wing altitude is lowered towards the ground surface, the size of the leading-edge vortex core region enlarges for both angles of attack, α=25°, and 35°. The efficiency of the wing aerodynamics is positively affected by its closeness to the ground due to the air cushion effect that occurs as a result of the increase in pressure on the suction surface of the slender wing due to the stagnation of air in the space between the delta wing and ground.

The GE on the formation of the vortical flow over a double delta wing having a sweep angle of Λ=70°/40° was examined using Particle Image Velocimetry (PIV) and dye flow visualization methods in this study. Qualitatively and quantitatively measured results are demonstrated for angles of attack, α=15° and 25° cases in the side and cross-flow planes to reveal the detail of the flow structures. The results demonstrated that the magnitudes of the strake and wing vortices at α=15° and the coiled-up vortex at α=25° progressively diminish when the delta wing moves from the free-stream flow region into the boundary layer region close to the ground surface, h/c=0.1. Also, the rate of the inboard movement towards the wing central axis increases on the pressure surface of the wing as the altitude of the double delta wing is gradually lowered to the ground surface. The strake and the wing vortices merge and become a "coiled-up vortex" by an increase of angles of attack from α=15° to 25°. The lift, $C_{L,}$ and the lift-to-drag ratio, $C_L/C_{D,}$ which defines the aerodynamic performances of the wing, are positively affected as a result of pressure recovery, air stagnation, and airbag dynamics in the area between the wing and ground surfaces when the value of h/c is gradually reduced.

GENİŞLETİLMİŞ ÖZET

Özellikle yüksek hızlı uçaklarda kullanılan delta kanatlar hem yapısal hem de aerodinamik açıdan avantajlıdır. Ayrıca uçağın burnunda oluşan şok dalgaları delta kanadın hücum kenarının altında kalır ve delta kanat üzerindeki kanat ucu girdaplarının yapısı sayesinde yüksek süpürme açısına sahip delta kanatlar, Λ yüksek hücum açılara, α ulaşabilir. Delta kanadın verimli tasarım yapısı nedeniyle yüksek hızlarda düşük hava sürtünmesi delta kanadın daha hızlı hareket etmesini ve daha yüksek kaldırma kapasitesine sahip olmasını sağlar. Delta kanatlı uçakları klasik geriye doğru süpürme ve dikdörtgen kanatlı uçaklardan ayıran en önemli özelliklerden biri kanat ile gövde arasında eğim olmamasıdır. Bu kanat tasarımında delta kanat üzerinde hareket eden hava akımının hızı delta kanadın hızından fazla olmadığı için oluşan hava sürtünmesi düşüktür. Bu, uçağın daha yüksek hızlarda ve daha yüksek kaldırma kapasitesinde hareket etmesini sağlar. Serbest akışta şok dalgası, ses hızının aşılması, uçak kanatlarına etki eden sürtünme kuvvetinin önemli ölçüde artmasına neden olduğunda meydana gelir. Delta kanatların sesten daha hızlı hareket edebilen uçaklarda daha çok tercih edilmesinin nedeni, uçak ses hızındayken oluşan ses duvarı nedeniyle hava sürtünmesindeki artıştan daha az etkilenmeleridir. Yani yüksek hızlar için oldukça verimli bir yapıya sahiptir. Bu da delta kanatlara olan ilginin artmasına neden oluyor. Delta kanat yapısının bir diğer avantajı da delta kanatlı uçaklar için yüksek taşıma kapasitesi sağlamasıdır. Delta kanat gövdeye uzun bir alandan takıldığı için gövde yapısı olarak çok daha sağlam ve dayanıklı hale gelmektedir.

Narin ve narin olmayan delta kanatlar arasındaki en temel fark, süpürme açısıdır. Süpürme açısındaki fark, aerodinamik olarak delta kanatların manevra kabiliyetlerini ve çalışma koşullarını etkiler. Örneğin, narin kanatlar yüksek hücum açılarında ve yüksek hızlarda çalıştırılabilir. Ancak, narin olmayan delta kanatlar, orta hücum açılarında uçmak için uygundur. Ayrıca, narin kanatlar yüksek hücum açılarında yüksek kaldırma katsayılarına ulaşabilirken, narin olmayan delta

kanatlar düşük ve orta hücum açılarında maksimum kaldırmaya ulaşabilir. Ek olarak, hız kaybedip düşme bölgesinde maksimum hücum açısı, narin ve narin olmayan delta kanatlar arasında farklılık gösterir. Örneğin, Taşcı ve ark. (2020) tarafından yürütülen Λ=70° olan narin bir kanat için 33° iken, hız kaybedip düşme bölgesinden önce Λ=40° olan narin olmayan bir delta kanat için maksimum hücum açısı, Tumse ve ark. (2021) tarafından belirtilen 17°'dir. Narin ve narin olmayan delta kanatlar arasındaki diğer bir fark, kanat yüzeyinde hücum kenarı girdabı tarafından kapsanan alandır. Birincil girdaplar narin bir kanatta daha yuvarlak ve daha küçük olmasına rağmen, birincil girdaplar, Lee ve Ko (2016) tarafından belirtildiği gibi aynı hücum açısında, narin olmayan bir delta kanat üzerinde daha geniş bir alana yayılmaktadır. Genel olarak, bu iki delta kanat konfigürasyonunun aerodinamik ve akış fiziği açısından çok farklı olduğu görülebilir.

Zemin etkisinin ne olduğu ve zeminin bu durumları nasıl etkilediğinin araştırılması gerekmektedir. Yer etkisi olgusu, genellikle "daha iyi uçma yeteneği" olarak tanımlanır. Bu olguyu kısaca anlatmak gerekirse şu şekilde açıklanabilir: delta kanat alçalmaya başlar, ancak iniş hızı gerekenden fazladır. İnişte uçak yer etkisine girdiğinde "hava yastıklaması" adı verilen bir kaldırma durumu ile karşılaşılır. Yer etkisi, yerden bir kanat açıklığı menzilde en güçlüsüdür ve yere yakınlık arttığında yer etkisi artar. Yer etkisi, kaldırma kuvvetinin, F_L artmasına neden olurken, sürükleme kuvvetini, F_D azaltır. Yer etkisinin oluşmasındaki ana faktör kanat uçlarında oluşan hava girdaplarıdır. Yer etkisi, uçağın etrafındaki aşağı doğru ve kanat ucu girdaplarını kısıtlar. Uçak yere yaklaştıkça girdapların yapısal oluşumu da etkilenir. Başka bir deyişle, delta kanat yere yaklaştığında, kanat uçlarındaki hücum kenarı girdapları serbest akışta olduğu kadar büyüyemez. Bunun nedeni, zeminin akışın mansabının oluşmasını engellemesidir. Bir başka deyişle, delta kanadın etrafındaki akış sürekli dönüyor ancak akış yere çarptığı için bu dönüş tamamlanamıyor. Delta kanadın altındaki basınç yukarıdakinden daha fazladır ve bu da kaldırma oluşturur. Akış ile kanat yüzeyi arasındaki etkileşimin artmasının neden olduğu kaldırma kuvvetinin zemin etkisiyle arttığı görülmüştür.

Dinamik hava yastığı, zemin yüzeyi ile delta kanat arasındaki alandaki hava durgunluğu nedeniyle, kiriş yönünde delta kanadın alt kısmındaki ters basıncın gradyanındaki artıştır. Böylece dinamik hava yastığının etkisinin kaldırmanın artmasına neden olduğu görülmektedir.

Mevcut çalışma, yer etkisi altında Λ=70° ve 70°/40° olan narin ve düble delta kanatlar üzerinde zemin mesafesinin (*h/c*) değişmesi ile gelişen girdaplı akış oluşumunu nitel ve nicel olarak araştırmaktadır. Bu kapsamda su kanalında Parçacık Görüntülemeli Hız Ölçümü (PIV) ve boya görselleştirme yöntemleri ile rüzgâr tünelinde aerodinamik kuvvet ölçümü gerçekleştirilmiştir. Sonuç olarak, delta kanat üzerindeki aerodinamik özellikler ve girdaplı akış yapıları, delta kanat ve zemin yüzeyindeki akış arasındaki etkileşimin yoğunluğu nedeniyle önemli ölçüde değişmektedir. Bu nedenle, kalkış ve iniş pozisyonları sırasında delta kanadın aerodinamik özellikleri üzerindeki yer etkisinin araştırılması da hayati önem taşımaktadır. Akışın ayrıntılarını ortaya çıkarmak için hücum açıları, düble delta kanat için α=15° ve 25° ve narin delta kanat için α=25° ve 35° için yan ve kanat arka akış düzlemlerinde nitel ve nicel olarak ölçülen sonuçlar gösterilmiştir. Delta kanadın kiriş uzunluğu, *c* ile normalize edilen, delta kanat ile zemin yüzeyleri arasındaki mesafe, *h*, *h/*c=0,1, 0,25 0,55 ve zemin etkisiz durum (GFE) olarak seçilmiştir. Ayrıca deneyler, kanat arka eksen akış düzlemi üzerinde, delta kanadın kiriş uzunluğu ile normalize edilen *x/c*=0.8 bölgesinde gerçekleştirilmiştir. Boya görselleştirme ve PIV deneyleri için Reynolds sayısı $Re=2\text{x}10^4$ olarak belirlenmiştir. Rüzgâr tünelindeki deneyler için, 5°≤α≤45° aralığındaki hücum açılarında ve yer etkisi olmayan bölgeden *h/c*=0.55, 0.25, 0.10'a kadar olan yer mesafelerinde Reynolds sayısı $Re=1\text{x}10^5$ olarak alınmıştır.

Bu çalışma, 70 derecelik süpürme açısına sahip narin bir delta kanat üzerindeki girdap akış yapıları üzerindeki zemin etkisini, boya akışı görselleştirme ve Parçacık Görüntü Hız Ölçümü tekniklerini kullanarak niteliksel ve niceliksel olarak incelemiştir. Boya görselleştirme ve PIV yöntemleri ile ölçümler, hücum açıları α=25° ve 35° olan plan görünüm, yan görünüm ve arka görünüm düzlemlerinde gerçekleştirilmiştir. Ayrıca deneyler, arka görünüm düzlemi üzerinde kanat yüzeyinde *x/c*=0.8 olan bir normalleştirilmiş bölgede gerçekleştirilmiştir. Sonuçlar, delta kanat zemin etkisinin olmadığı bölgeden kanat konumu *h/c*=0.1 bölgeye hareket ettiğinde, öncü girdap büyüklüklerinin kademeli olarak azaldığını göstermektedir. Sonuçlar, delta kanadı zeminsiz bölgeden kanat konumuna *h/c*=0.1 hareket ettiğinde, öncü girdap büyüklüklerinin kademeli olarak azaldığını göstermektedir. Ayrıca, yan ön kenardan kanadın merkez eksenine doğru iç akış hızı, zeminin delta kanadın emme yüzeyi üzerindeki etkisiyle yükselir. Kanat yüksekliği zemin yüzeyine doğru alçaltıldığında, hücum kenarı girdap merkez bölgesinin boyutu, α=25° ve 35° olmak üzere her iki hücum açısı için genişler. Kanat aerodinamiğinin verimi, kanatlar arasındaki boşlukta havanın durgunluğu nedeniyle narin kanadın emiş yüzeyindeki basıncın artması sonucu oluşan hava yastığı etkisi nedeniyle yere yakınlığından olumlu yönde etkilenir.

Bu çalışmada, süpürme açısı Λ=70°/40° olan bir çift delta kanat üzerinde girdaplı akışın oluşumu üzerindeki GE, Parçacık Görüntü Hızı (PIV) ve boya akışı görselleştirme yöntemleri kullanılarak incelenmiştir. Akış yapılarının detayını ortaya çıkarmak için hücum açıları, yan ve arka akış düzlemlerinde α=15° ve 25° durumları için nitel ve nicel olarak ölçülen sonuçlar gösterilmiştir. Sonuçlar, delta kanadı serbest akış bölgesinden sınır tabakası bölgesine yakın bölge olan *h/c*=0.1'e doğru hareket ettiğinde, α=15°'deki sıra ve kanat girdaplarının ve α=25°'deki sarmal girdapların büyüklüklerinin giderek azaldığını göstermiştir. Ayrıca, çift delta kanadın yüksekliği kademeli olarak zemin yüzeyine indirildiğinden, kanadın basınç yüzeyinde kanat merkez eksenine doğru, bir başka deyişle, içe doğru hareket hızı artar. Sıra ve kanat girdapları birleşir ve hücum açılarının α=15°'den 25°'ye artmasıyla "sarmal girdap" haline gelir. Kanadın aerodinamik performansını tanımlayan kaldırma, C_L ve kaldırma-sürükleme oranı, C_L/C_D, kanat ile yer arasındaki bölgedeki basınç geri kazanımı, hava durgunluğu ve hava yastığı dinamikleri sonucunda *h/c* değeri kademeli olarak azaldığında yüzeyler olumlu yönde etkilenir.

ACKNOWLEDGEMENTS

I would like to thank my supervisor Prof. Dr. Beşir ŞAHİN who continuously supported and guided my thesis work. Also, I would like to express my gratitude to Prof. Dr. Hüseyin AKILLI for his support and encouragement as the Head of the Mechanical Engineering Department.

I would like to thank Assist. Prof. Dr. Hürrem AKBIYIK and Research Assistant Sergen TÜMSE for their invaluable assistance during my experiments.

I would like to express my special thanks to my wife, Gözde TAŞCI who was with me during my Ph.D. studies, sharing my sadness and joy, and giving me strength with her presence and mentorship.

I sincerely thank to Prof. Dr. Yahya Erkan AKANSU, Prof. Dr. Coşkun ÖZALP and Assoc. Prof. Dr. Bülent YANIKTEPE for allowing me use the labrotaries, and Assoc Prof. Dr. İyas KARASU, Assoc. Prof. Dr. Tahir DURHASAN Lecturer Ertuğrul ŞEKEROĞLU, Laboratory technician Sefa MERAL, M.Sc. Students Ezgi AKBUDAK and Ömer KENAN for their help during my journey.

For their great patience and support during my PhD study, my sincere thanks go to my dearest family. I express my deepest gratitude, especially to my mother and father, and to all family members who have continuously encouraged me along the way of my Ph.D. studies.

Lastly, I am grateful to the Çukurova University Scientific Research Project Office for their financial support under contract no: FDK-2019-11368. I am grateful to the Department of Energy Systems Engineering of Osmaniye Korkut Ata University for allowing the use of PIV and flow visualization experiments and the Mechanical Engineering Department of Nigde Omer Halisdemir University for allowing the use of wind tunnels. I am thankful to be granted by TÜBİTAK (The Scientific and Technological Research Council of Turkey), and YOK through a Doctoral Researcher Program with scholarship numbers 2211-C, and 100/2000.

Thank you so much to everyone who shared this journey with me.

CONTENT **PAGES**

LIST OF FIGURES **PAGES**

NOMENCLATURE

c	: Chord of the delta wing
h	: The distance between the ground and trailing edge of the
h/c	delta wing
z/s	: Normalized ground distance
y/s	: Normalized vertical distance
	: Normalized horizontal distance
x, y, z	: Streamwise, transverse, and vertical coordinate directions
Re	: Reynolds number
St	: Strouhal number
s	: Span of the delta wing
U_∞	: Freestream velocity
C_L	: Lift Coefficient
C_D	: Drag coefficient
C_L/ C_D	: Lift-to-Drag ratio
C_P	: Pressure coefficient
F_L	: Lift force
F_D	: Drag force
u, v, w	: Streamwise, spanwise and vertical components of velocity
α	: Angle of attack
β	: Yaw angle
Λ	: Sweep angle
Δ	: Difference in the value of a physical quantity
Λ	: Wavelength
ρ	: Density of fluid
ω	: Vorticity

GE	: Ground Effect
GFE	: Ground-Free Effect
GFC	: Ground-Free Case
VB	: Vortex Breakdown
LEV	: Leading-Edge Vortex
DPS	: Density of Power Spectrum
PIV	: Particle Image Velocimetry
RMS	: Root-Mean-Square
WIG	: Wing In Ground
CCD	: Charge-Coupled Device
Nd: YAG	: Neodymium-Doped Yttrium Aluminum Garnet

1. INTRODUCTION

1.1. Delta Wings

Delta wings used in aviation, designed for utilization at high speeds, have various benefits in structure and aerodynamics. For example, the shock waves occurring at the delta wing-tip with a high sweep angle, Λ, stay below the leading edge of the delta wing, which allows the aircraft to attain high angles of attack, α as indicated by Gursul (2005). Low air friction at high speeds, which is due to the efficiency of the delta wing design, is beneficial for the delta wing to move faster and to have higher lift capacity (Gursul et al., 2005).

Straight wings are advantageous in terms of creating a high lift force at low speed. However, these straight wings are not suitable for high-speed aircraft. Since the airflow acting on straight wings with a higher aspect ratio is greater, the friction force created by the air in straight wings is greater than in delta wings. Today, the delta wing design can be considered the advanced form of the classic backward swept and rectangular wing design. One of the most important features that distinguish delta-wing aircraft from classic backward swept and rectangular wing airplanes is that there is no slope between the wing and the body as seen in Figure 1.1. In this wing design, since the speed of the airflow traveling on the delta wing is not more than the speed of the delta wing, the resulting air friction is low. This allows the aircraft to move at higher speeds and higher lift capacity as pointed out by Gursul (2003). The shock wave in free-flow occurs when the exceeded speed of sound causes the friction force acting on the wings to increase significantly. The reason why delta wings are mostly preferred in aircraft that can move faster than sound is that they are less affected by the increase in air friction due to the sound wall formed when the aircraft is at sound speed. In other words, it has a very efficient structure for high speeds. This causes an increase in the interest in the delta wings as also stated by Gursul (2003). Another advantage of the structure of the delta wing is that it provides high payload capacity for delta-wing aircraft.

Since the delta wing is attached to the body from a long area, it becomes much more robust and durable than the body structure.

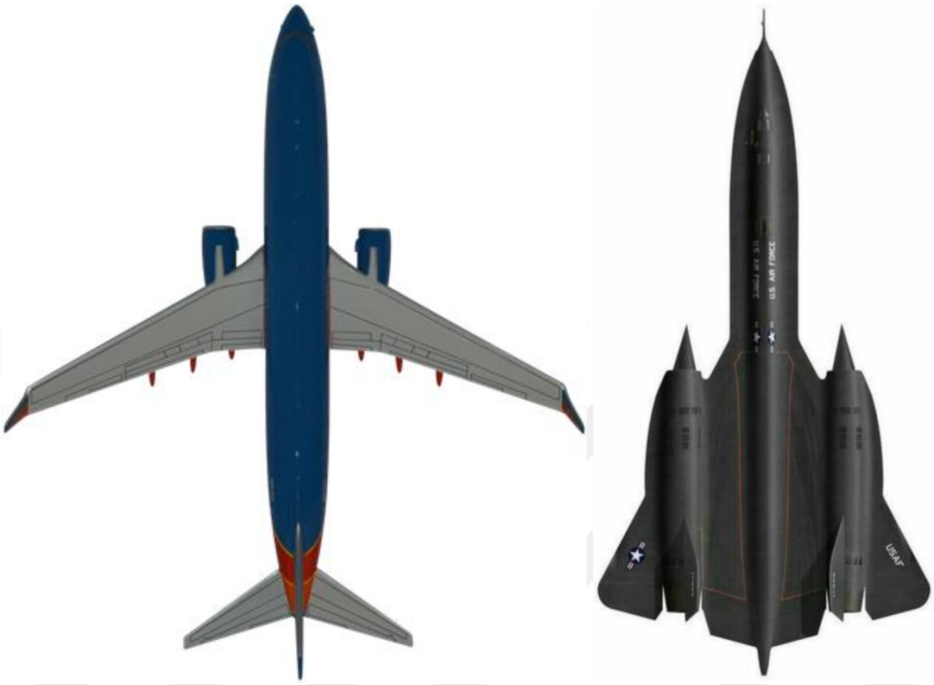

Figure 1.1. The difference in the configurations between a classic backward airplane (Boing 737) and a delta wing aircraft (Lockheed SR71 Blackbird)

The most fundamental difference between slender and non-slender delta wings is the sweep angle, Λ. The details of this classification will be mentioned in the literature survey of the thesis. However, it is useful to include some basic differences between these two wings in the introduction of the thesis. The difference in the sweep angle, Λ aerodynamically affects the maneuvering capabilities and operating conditions of the delta wings. For example, the slender wings can be operated at high angles of attack, α, and high speeds. However, the non-slender delta wings are suitable for flying at moderate angles of attack, α. Also, the slender wings can achieve high lift coefficients, C_L at high angles of attack, α, while the non-slender delta wings can reach the maximum lift, C_L at low and moderate angles of attack, α. In addition, the maximum angle of attack, α to the stall region differs between the slender and the non-slender delta wings. For example, the maximum angle of attack, α for a non-slender delta wing having Λ=40° before the stall zone is 17° indicated by Tumse et al. (2021), while it is 33° for a slender wing having Λ=70° conducted by Tasci et al. (2020). Another difference between the slender and the non-slender delta wings is the area covered by the leading-edge vortex (LEV) on the wing surface. Although the primary vortices are more rounded and smaller on a slender wing, the primary vortices spread over a wider area on a non-slender delta wing at the same angle of attack, α as indicated by Lee and Ko (2016) in Figure 1.2. In general, it can be seen that these two delta wing configurations are very different in terms of aerodynamics and flow physics.

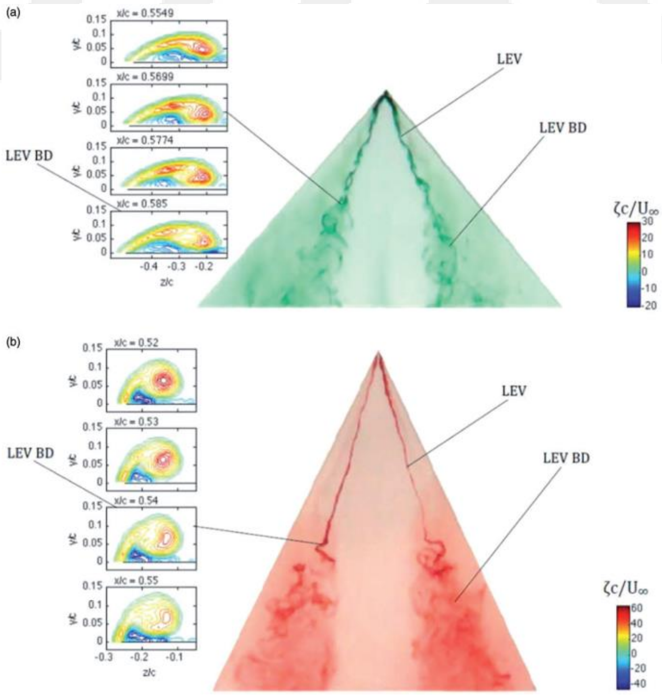

Figure 1.2. The representation of the difference in the shape and the LEV on slender and non-slender delta wings (Lee and Ko, 2016)

1.2. The Ground Effect on a Delta Wing while Landing and Taking-off

It is necessary to investigate the ground effect and how it affects landing and taking-off cases. This phenomenon is often described as "better flying ability". If this phenomenon is needed to describe briefly, it can be explained as: the delta wing starts to descend for landing or flies close to the water surface, there is a flow resistance occurs between the suction surface of the aircraft and the ground or water surface. When the aircraft enters the ground effect, a lifting condition called "air cushioning" is encountered as seen in Figure 1.3. Therefore, the aircraft floats as it does on the runway. This endless gliding happens because of the ground effect. The ground effect is strongest in the range of a wingspan above the ground, and the ground effect increases when the proximity to the ground increases as mentioned by Hainsworth (1988). The ground effect causes the lift force, F_L to increase while reducing the drag force, F_D. The main factor in the occurrence of the ground effect is the air vortices formed on the wingtips. The ground effect restricts downwash and wingtip vortices around the aircraft. As the aircraft approaches the ground, the structural formation of the vortices is also affected. In other words, when the delta wing lowers to the ground, the leading-edge vortices at the wingtips cannot grow as much as they are in the free-flow. The reason for this is that the ground prevents the formation of the downstream of the flow. The flow around the delta wing is constantly rotating, but this rotation cannot be completed as the flow hits the ground. When the flow exits the trailing edge of the delta wing, it angles downward, which is called downstream flow, and this flow is restricted as it approaches the ground. The pressure under the delta wing is higher than above, and this creates lifting. The strengthening of the lifting caused by the interaction between the flow and the wing’s surface increases because of the ground effect as shown in Figure 1.4. Because, the impact of the dynamic air cushion, which is the increase in the gradient of the adverse pressure on the bottom of the delta wing through the chordwise direction because of the air stagnation in the area between the ground and the wing, causes the lifting to increase as indicated by Yun et al. (2010).

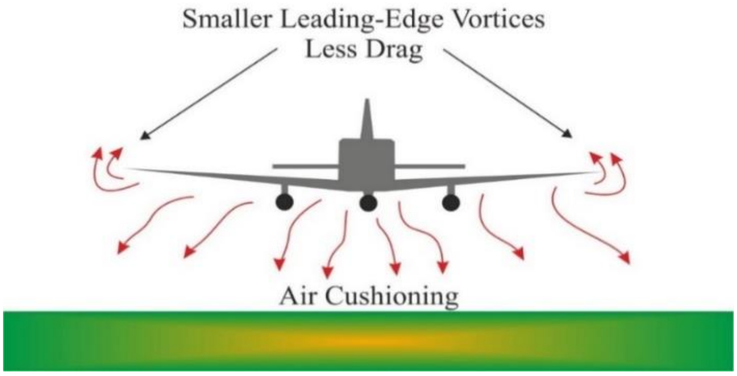

Figure 1.3. The behavior of the leading-edge vortices under the ground effect

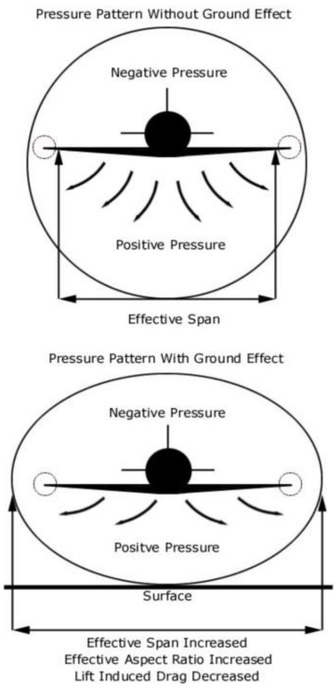

Figure 1.4. The illustration of the formation of the pressure distribution along the spanwise of the airplane with/without the ground effect (The Aviation History Online Museum, 2015)

The required angle of attack, α under the GE is reduced before the wing stalls for a given amount of lift force as seen in Figure 1.5 as a common behavior of the ground effect. The extent of this reduction in stalling α will vary according to the structure of the wing, but not very much different. Also, several differences can affect the amount of the maximum lift coefficient, C_L of a stated wing in ground effect compared to the lift coefficient in free-stream flow. The lift force, F_L of the wing under the ground effect will reach higher values at lower angles of attack compared to the no-ground case, and the possibility of the early stall zone due to an increase in lift force, F_L may occur at a low angle of attack. The early stall zone caused by the higher F_L occurring at the early angle of attack can cause unexpected accidents while landing (NTSB Aircraft Accident Report, AAR-12/02, 2011).

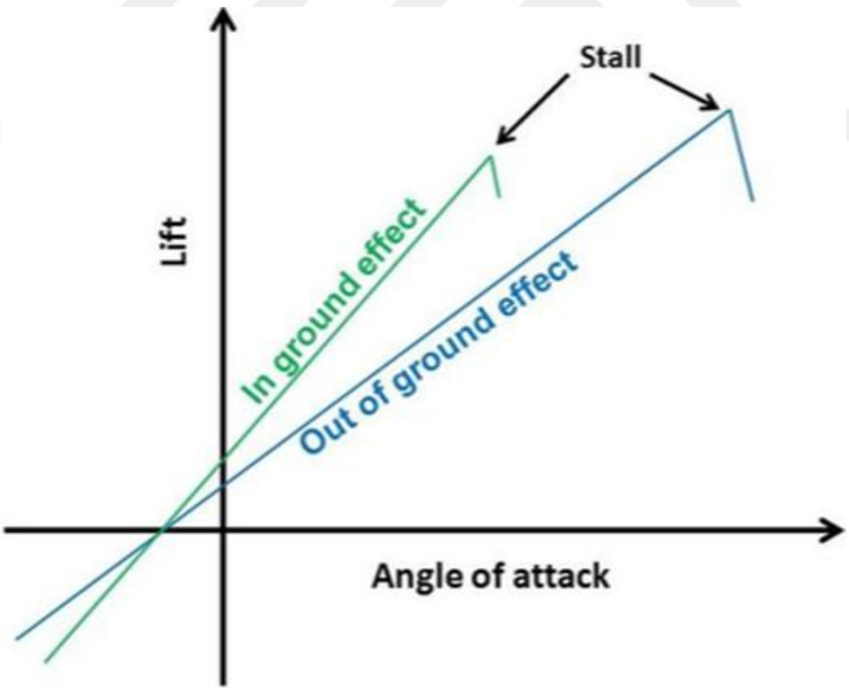

Figure 1.5. The lift vs angle of attack in the case of ground and no-ground (NTSB Aircraft Accident Report, AAR-12/02, 2011)

As the aircraft is affected by the ground effect, the lifting force it is exposed to accelerates, in other words, it starts to resist gravity. In this case, the friction force that the wings are exposed to decreases. Since the friction force is low, there is a decrease in the thrust force that will allow the plane to maintain its speed. In other words, better performance is obtained by using less power. Although the ground affects the entire aircraft, it is most strongly seen on the leading edges of the wing (wingtip vortices). The force that balances drag in straight flight is the trust force. The aircraft requires less thrust, as the total drag decreases due to the ground effect. For instance, the induced drag is reduced by approximately 50% while the delta wing maintains the flight at a height of 1/10 of the span length as seen in Figure 1.6. A vehicle under the influence of the ground can fly at a lower speed or the same speed with less thrust than in the area of no-ground. Similar results are seen in the study of the flight anatomy of brown pelicans under the ground effect by Hainsworth (1988).

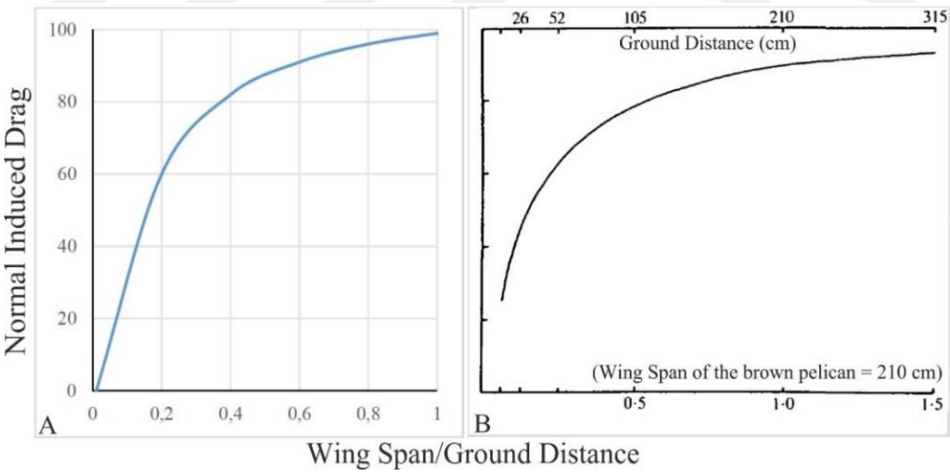

Figure 1.6. The change of normal induced drag concerning chord/ground distance ratio for a) an aircraft and b) a brown pelican (Hainsworth, 1988)

Although only landing has been mentioned so far, a ground effect also creates some effects on the aircraft during take-off. The friction force that the aircraft is exposed to during take-off is less than in the landing due to the ground effect. However, as the aircraft takes off, the drag force, F_D is exposed to increases with the decrease of ground effect. In this case, with the increase in the angle of attack, the vortex encounters the breakdown, and the climbing performance and the speed of the aircraft decrease. To prevent the negativizes, trust force is used and thus a smooth start is obtained.

There is a way to make the ground effect, where planes can be adversely affected, beneficial for commercial and military grades as described by Yun et al. (2010). Aircrafts such as American-made C-5 Galaxy (A) and Russian-made Ekranoplan (B) are designed to fly only with the ground effect which is called Wing in Ground (WIG) planes. So, these planes only fly a few meters above the ground. Since the lifting, which the aircraft is subjected to, is in a perpendicular state to the ground or water surface, they can carry much heavier loads than the normal version backward swept planes as a result of air cushioning. After these first implementations, many futuristic works such as Airfish-8 (WigetWorks) (C) and Boing Pelican Ultra (D) continued on this subject as seen in Figure 1.7.

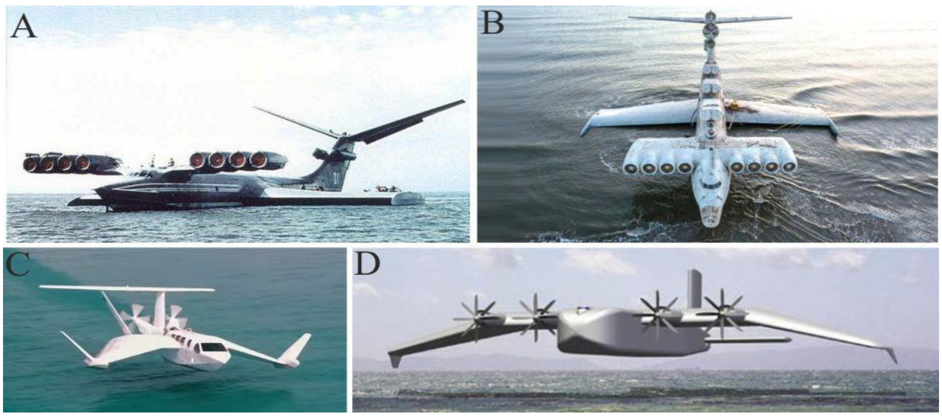

Figure 1.7. The examples of the wing-in-ground (WIG) planes

For an aircraft, the situations experienced in take-off and landing procedures, in general, were evaluated. However, another situation that needs to be taken into account is to examine how the aerodynamic features of the delta wing are affected in cases where turbulence increases. Considering the effect of the wind on take-off and landing, turbulence level is one of the most important conditions for the safety of the aircraft. The turbulence that most affects the aircraft during take-off and landing is low-level wind shear as stated by O'Connor and Kearney (2018). Wind shear can be defined as the unexpected difference in wind speed and/or direction. Low-level wind shear is one of the most important effects on the aerodynamic performance of an aircraft during take-off and landing, which has an adverse effect on the performance of the aircraft, as mentioned by Laynor and Roberts (1975). After the recognition of the existence of the low-level wind shear, it must not be undervalued how important the impact of low-level wind shear may be on a pending aircraft as shared in the reports of Frost (1983), Frost and Bowles (1984). The wind shear may happen at any level, but the low-level wind shear may reason to restrict the ability to control the aircraft during take-off and landing. It is vital to realize the main forces acting on the aircraft during the flight to examine the impact of the turbulence and low-level wind shear. As detailed by ICAO (2005), the thrust force, F_T is delivered by engines, the lift force, F_L is delivered by wings, and the others are the weight, W, and the drag force, F_D of the aircraft as shown in Figure 1.8. The lift must equalize the weight and the thrust must equalize the drag in unaccelerated flight. The resultant force is zero when the forces are in equilibrium on the aircraft and the movement continues in equilibrium until the equilibrium is disrupted according to Newton's First Law during take-off and landing. The low-level wind shear can affect both the flow speed and the angle of attack, α, and also, the lift force, $F_{L,}$ and the drag force, F_D. The low-level wind shear disturbs the equilibrium of the aircraft during take-off and landing. Vertical wind shear reasons changes in the horizontal wind component that can affect the speed of the aircraft during take-off and landing. The change of the horizontal wind can cause a sudden increment or a drop in headwind and tailwind that affects the take-off and the landing of the aircraft. These sudden changes cause an increase in unsteady loading on the aircraft. This is an undesirable situation both structurally and aerodynamically. In light of the information, it is important to examine the effects of low-level wind shear on a delta wing during take-off and landing.

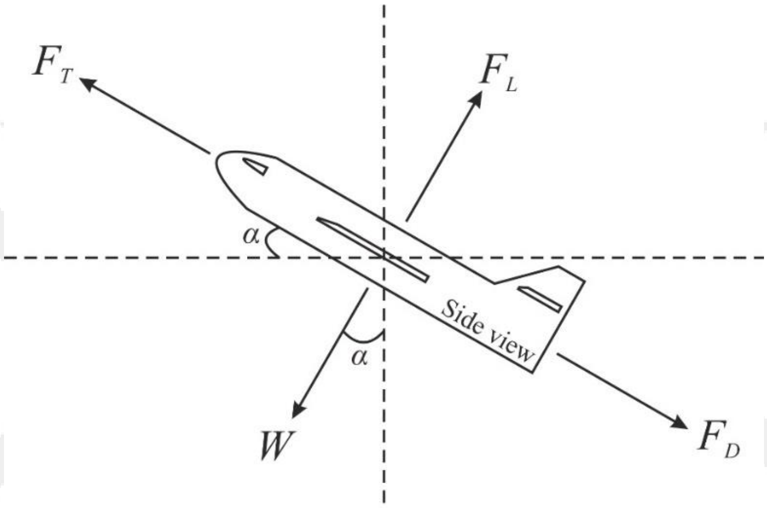

Figure 1.8. Force Distribution on the aircraft during taking-off and landing (ICAO,2005)

1.3. Outline of the Thesis

The current study is aimed to qualitatively and quantitatively examine the change of the vortical flow structure formed downstream of the onset of VB over the suction side of the delta wing under the GE with the variations of *h/c*. In this context, dye visualization and PIV techniques have been employed. Unambiguously, although it is possible to find a few studies about the GE on the structure of the vortical flow field such as Ahmed and Sharma (2005); Musaj and Prince (2008); Prasad and Damodaran (2013); Lee and Ko (2018); Tumse et al. (2019), it can be said that there are not many studies about the GE on the variation of the aerodynamic features and the vortical flow structure over a delta wing with Λ=70°.

This study also qualitatively and quantitatively investigates the vortical flow formation developed over the double delta wing having Λ=70°/40° under the GE with the change of the ground distance, *h/c*, as well as the ground-free case (GFC). In this context, the PIV and dye visualization methods in the water channel and the aerodynamic force measurement in the wind tunnel were carried out. Nevertheless, it is probable to find a few numerical and experimental investigations about the GE on the formation of the vortical flow over the different wing configurations, such as an experimental study of a non-slender delta wing configuration conducted by Tumse et al (2021), a numerical study of a NACA 0012 wing configuration stated by Prasad and Damodaran (2013) and an experimental study of a NACA 0015 wing configuration reported by Ahmed and Sharma (2005). However, because of the lack of literature, it is seen that there are not any experimental investigations related to GE on the change of aerodynamic properties and the formation of the vortical flow field on the double delta wing having Λ=70°/40°.

The point that discriminates the current study from the other published studies is to investigate the GE on the change of the aerodynamic characteristics of the slender and double delta wings with Λ=70° and 70°/40° using qualitative and quantitative techniques. In summary, this study contains groups of dye images, the time-averaged and instantaneous vorticity and streamline patterns, turbulence kinetic energy (TKE), the density of the power spectrum (DPS) analysis of the fluctuations in the vertical direction, and the alteration of the aerodynamic properties of the slender and double delta wings disclose the physics of the vortical flow over the double delta wing comprehensively.

2. PREVIOUS STUDIES

2.1. Vortical Flow Behavior on a Delta Wing

As it is known, vortices are one of the reasons that affect aircraft performance. For instance, the vortices that occurred in certain areas of the fuselage of the aircraft reduce aircraft maneuverability and cause material fatigue. Delta wings have been developed as a primary design element in many combat aircraft by evolving as a result of years of research from past to present. The understanding of vortex behavior, vortex-wing surface interaction, the unstable flow structure, and the flow physics are very important to increase the aerodynamic performance of these special aircrafts (Heron and Myose, 2005).

The vortex breakdown is also a key design parameter that is very influential on the aerodynamic performance and the structure of leading-edge vortices over the delta wings. However, the maneuvering capacity of these wings is limited by the formation of the vortex breakdown (VB), affecting adversely the aircraft's aerodynamic efficiency, which is generally aimed to control or delay for better maneuverability improvement. Delery (1994) defines the VB as the quick extension of the leading-edge vortex (LEV) structure, the substantial change of the velocity component of the vortical flow, and the formation of significant velocity fluctuations. The VB and the vortical flow formation deteriorate the aerodynamic performance of the delta wing; therefore, it is vital to keep the VB under control. The VB can cause a sudden expansion of the vortical flow structure, severe changes in the velocity field, and the presence of large-scale oscillations, as stated by Payne et al (1986). Cui et al (2007) discussed the effect of the VB on the aerodynamic behaviors of an aircraft, such that the VB induces a decrease in the lift, $C_{L,}$ and an increase in drag C_D simultaneously.

The phenomenon of vortex breakdown can be observed in three different types, namely, double helix type (Sarpkaya, 1971), and bubble and spiral types (Gursul and Wang, 2018) as seen in Figure 2.1.

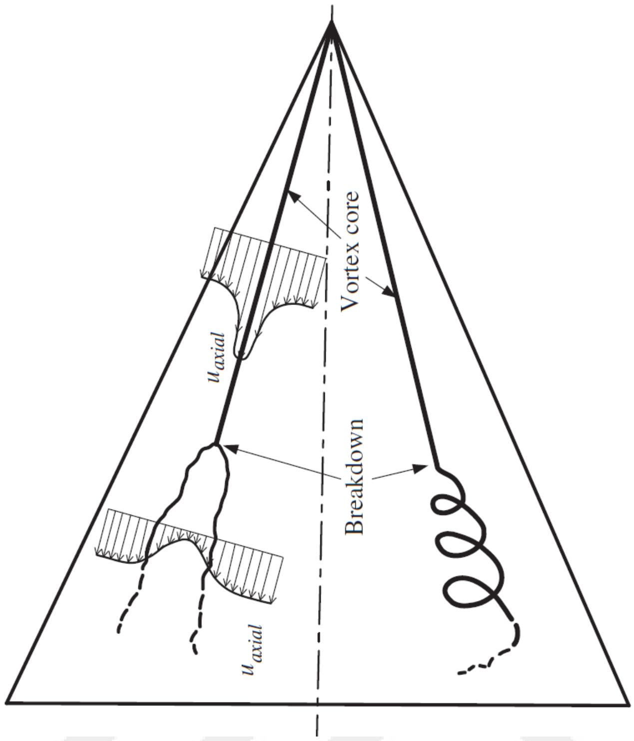

Figure 2.1. The Representation of the vortex breakdown types such as spiral and bubble (Gursul and Wang, 2018)

In the investigation of Gursul et al. (2007), it was expressed that the structure of the vortical flow of a delta wing is made up of two counter-rotating leading-edge vortices. The location of the vortex breakdown is changed as a function of the angle of attack, precisely. The vortex breakdown causes a decrease in the performance of the aircraft and the unsteady flow structure causes the stability of the aircraft to disrupt. Because of that reason, vortex breakdown control plays a very important role. There is a strong relation between sweep angle, Λ, angle of attack, α, and sideslip angle, β. When these parameters change, the vortex breakdown location of the leading-edge vortices easily changes. Besides, the maneuver capacity of these delta wings is restricted by the structure of the vortex breakdown which negatively impacts the aerodynamic performance of the aircraft.

Hence, the control and delaying of the vortex breakdown are essential for better maneuverability. The vortex breakdown and its effect on the performance of the aerodynamic features were studied by several researchers. For detailed information about the vortex breakdown and its impacts on the structure of the vortical flow and the performance of the aerodynamic systems, the published studies may be referred to as Hall (1972), Escudier (1988), Miller and Williamson (1997), Sahin et al. (2001), Lucca-Negro and O'Doherty (2001), Mitchell and Delery (2001), Nelson and Pelletier (2003), Ol and Gharib (2003), Lu and Zhu (2004), Taylor and Gursul (2004), Gursul et al. (2007), Sahin et al. (2012), and Tasci et al. (2021). The vortical flow structure over a delta wing in the crossflow plane was schematically represented in Figure 2.2.

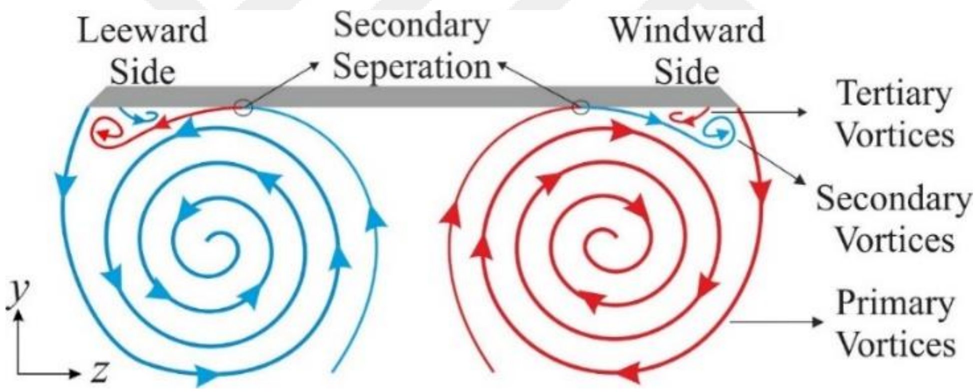

Figure 2.2. The Representation of the vortical flow structure over the slender delta wing in the crossflow plane (TAŞCI et al., 2021)

Important parameters affect the vortex dynamics of a delta wing, such as Reynolds number, *Re*, the angle of attack, *α*, the sweep angle, *Λ*. Since the flow structure is very sensitive in a certain range of Reynolds numbers, *Re*, it is necessary to determine Reynolds numbers that do not affect the vortex breakdown (Yanıktepe, 2006). In the transition regime, the unsteady complex flow structure formation over a delta wing having Λ=75° may occur with the increase in *Re* (Visbal, 2004) as seen in Figure 2.3.

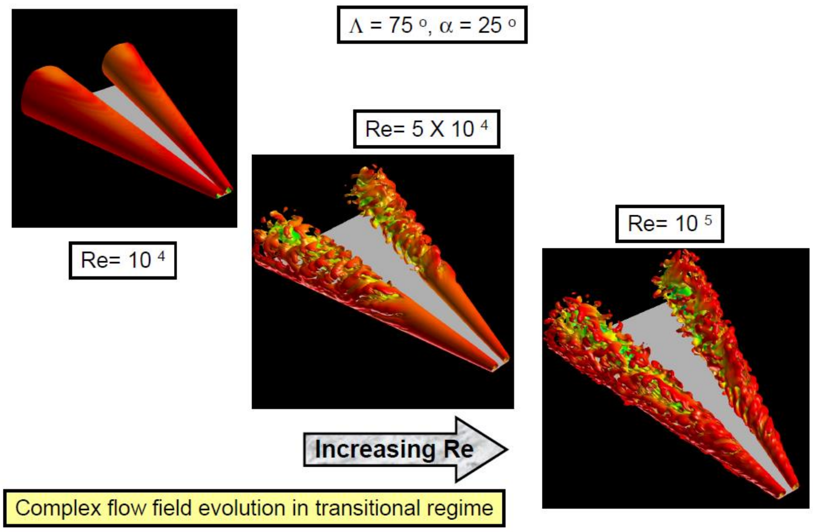

Figure 2.3. The Representation of the unsteady complex flow structure over a delta wing in the transition regime (Visbal, 2004)

An empirical study over a 75-deg-swept slender delta wing was conducted to search the vortex breakdown core in the investigation of Gursul and Xie (1999). It was reported that the root means square (RMS) values at the origin of the vortex breakdown decrease at the lower Reynolds number, *Re*. Because the shear layer does not exhibit the instability of Kelvin-Helmholtz (K-H). But it is observed that after a critical Reynolds number, *Re*, shear layer is possessed by the structure of a vortical flow because of the instability of Kelvin-Helmholtz (K-H).

Delta wings are examined in two types: non-slender and slender, depending on the sweep angle, Λ, which is vital to classify the delta wings (Canpolat et al., 2009). Munro et al. (2005) stated that delta wings are classified as slender when the sweep angle, Λ is larger than or equal to 65°, and otherwise termed non-slender. The double delta wings are created by the combination of slender and non-slender delta wings types, i.e., double diamond wings as reported by Pevitt and Alam (2014). Brett and Ooi (2014) conducted the effect of the sweep angle, Λ on the moderate swept delta wings within the range of $43° \leq \Lambda \leq 65°$, numerically. It was stated that the location of the primary vortices and the reattachment of the leading-edge vortices move outboard when the sweep angle, Λ is increased.

The angle of attack, α is also a vital design parameter that causes the vortical flow structure over a delta wing to occur. However, one of the downsides of the delta wings is that the delta wings need a high angle of attack, α to avoid stalling at low speeds. For this reason, canards are located on the sides of the cockpit in delta-wing aircraft. These canards provide lifting to the aircraft and positively affect the payload capacity. However, besides these advantages, it causes the aircraft to have less maneuverability. When the angle of the canard attachment on the blended wing body is increased, the moment coefficient increases, and its maneuverability decreases (Ali et al., 2012). In addition, delta wings are subject to high drag force, F_D at low altitudes, and flow separation at high angles of attack, α. Since the flight is not stable at low speeds in this wing design, fighter jets move at high speeds while taking off and landing. The change of the vortex breakdown position is very sensitive related to the angle of attack, α. Many comprehensive studies have been conducted on the angle of attack, α. The effect of the angle of attack, α on the structure of the vortical flow over the lambda wing was studied by Yayla et al. (2013). They also qualitatively and quantitatively conducted an experimental study to indicate the structures of the leading-edge vortex breakdown in the cross-flow plane varying angles of attack in the sequence of $7° \leq \alpha \leq 17°$ at the different dimensionless locations, x/c along the central axis of the delta wing which has a 40-deg-swept by using the PIV and the dye visualization technique. It was revealed that the angle of attack, α had a significant effect on the VB location. Lambert and Yarusevych (2019) experimentally investigated the effect of the angle of attack, α on the compatible structures advanced in laminar separation bubbles over NACA-0018 within the range of 0°≤α≤10°. It is pointed out that the sum of primary vortices contained in the merging rises from 13% to 27% as the angle of attack increases from α=5° to 10°, but the size of the laminar separation bubbles decreases.

2.2. Control Methods of Vortex Breakdown

The control of the breakdown location of the leading-edge vortices of the slender delta wings is the most important goal and it is achieved by the alteration of the pressure gradient and the vortex level as stated by Gursul et. al (2007). For the control methods that need to be developed to control unsteady flow structure, vortex breakdowns, and subsequent vortices over the delta wings, it is substantial to examine the structure of the unsteady flow, vortex formation mechanism, and fluid-structure interaction. Recent research has shown that the flow control methods such as active and passive methods can be operated to audit the vortices behind the objects such as cylinders and delta wings. Flow control methods have various aims, such as displacement of vortices by approaching or wandering away from the delta wing surface, increasing vortex intensities, or delaying vortex breakdown. Some active and passive flow control techniques affecting a delta wing may be applied such as various wire control techniques over the delta wing, bleeding or blowing along the leading edge of the delta wings, perturbation or pitching motion techniques, using winglets, flaps, or fins over the delta wings, and flow control via actuators. It is also intended to delay the vortex breakdown occurring on the delta wings to increase the lift force, F_L. For this reason, leading-edge vortices are intended to be controlled using many flow control techniques to define the best control method as indicated by Gursul et al., 2007.

Nowadays, many active control methods are frequently used to understand the vortical flow structure over a delta wing. However, passive control methods are more commonly used in flight aerodynamics to control the vortical flow structure by making changes in the aircraft-wing body. The models such as double delta, diamond, and lambda are customized by adding some parts or extra delta wings to the trailing edge. Canpolat et al. (2017) demonstrated the impact of the structure of the vortical flow over the delta wing having a low sweep angle, Λ adding a part to the trailing edge of the wing handling dye visualization setup. The frame snapping was obtained by stereo-PIV to calculate the values of the time-averaged flow at an angle of attacks ranging from α=7° to 17° and sideslip angles ranging from β=0° to 15°. As seen from Figure 2.4, as the sideslip angle, β is given to the delta wing, the position of the vortex breakdown on the leeward side approaches the wing apex. In addition, the increasing angle of attack, α causes the leading-edge vortices to occur earlier. It was shown that the time-averaged positions of the vortex breakdown for the lambda wings and the delta wings having a low sweep angle, Λ occur near the delta wing surface. The experiments also show that the sideslip angle, β which is also an important parameter, significantly changes the flow structure. When the sideslip angle, β becomes more effective, it is concluded that adding a part to the trailing edge plays a very important role. As the angle of attack, α was slowly increased, the position of the vortex breakdown proceeded to the tip of the wings. In addition, the vortex breakdown occurred closer to the trailing edge of the delta wing compared to the lambda wing. When sideslip angle, β is given to the delta and lambda wings, the symmetrical flow structure is disrupted. The flow structures are almost symmetrical when the sideslip angle, β for both delta wings is 6°. The adding parts to the trailing edge of the delta wing maintained the flow structure over the delta wing when the sideslip angle, β was applied.

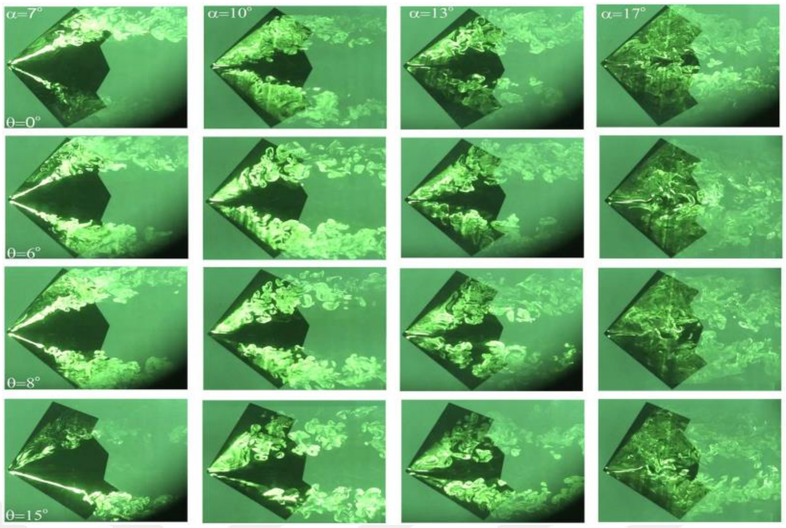

Figure 2.4. The change of the leading-edge vortices under the variation of the sideslip angle, β at a different angle of attacks, α (Canpolat et. al, 2017)

It is seen in the literature survey that there are not many experimental studies about the GE on a slender delta wing. It is also revealed that the published studies from the literature on the various types of double delta wings were carried out. However, it is found that are not many experimental studies about the ground effect on a double delta wing. Therefore, it is important to examine and understand the studies about the ground effect on the delta wings and the studies about the double delta wings, separately.

In addition to some numerical studies, such as Le Sueur (1935), Chawla et al. (1990), Yang et al. (2009), Luo and Chen (2012), Qin et al. (2015 and 2016), Qu et al. (2015), Jia et al. (2015), Velte et al. (2016) and Ko et. al (2020) about the ground effect in recent years, some experimental studies on the ground effect have also gained popularity. The aerodynamic properties of a slender delta wing with a wing-rock motion under the influence of varying ground distances in a low-speed wind tunnel were investigated experimentally by Kawazoe and Morita (2004). As a result of this study in Figure 2.5, the aerodynamic forces increase substantially as the delta wing gets closer to the ground surface. This study concluded that aerodynamic forces increase significantly as the distance of the delta wing to the ground surface decreases. The rolling moment coefficient, $C_{rm,}$ is effectively induced by the ground influences as a function of the angle of attack, α, especially at high angles of attack, α. Ahmet (2007) reported that the vortical flow structures of the NACA 4412 airfoil and its aerodynamic performance alter profoundly when it flies close to the ground boundary at the Reynolds number, $3x10^5$. The experiments were performed in a wind tunnel having a moving belt under the various angles of attack from 0° to 10° and the ground distances from 100% to 5% based on the chord length, *c*. The lift coefficient C_L first drops till the angle of attack of α=4° and then, it rises due to the higher-pressure distribution over the lower side of the airfoil. Their experiments were carried out in a wind tunnel with a moving belt, varying angles of attack from 0° to 10° under effects of ground distances between 100% and 5%.

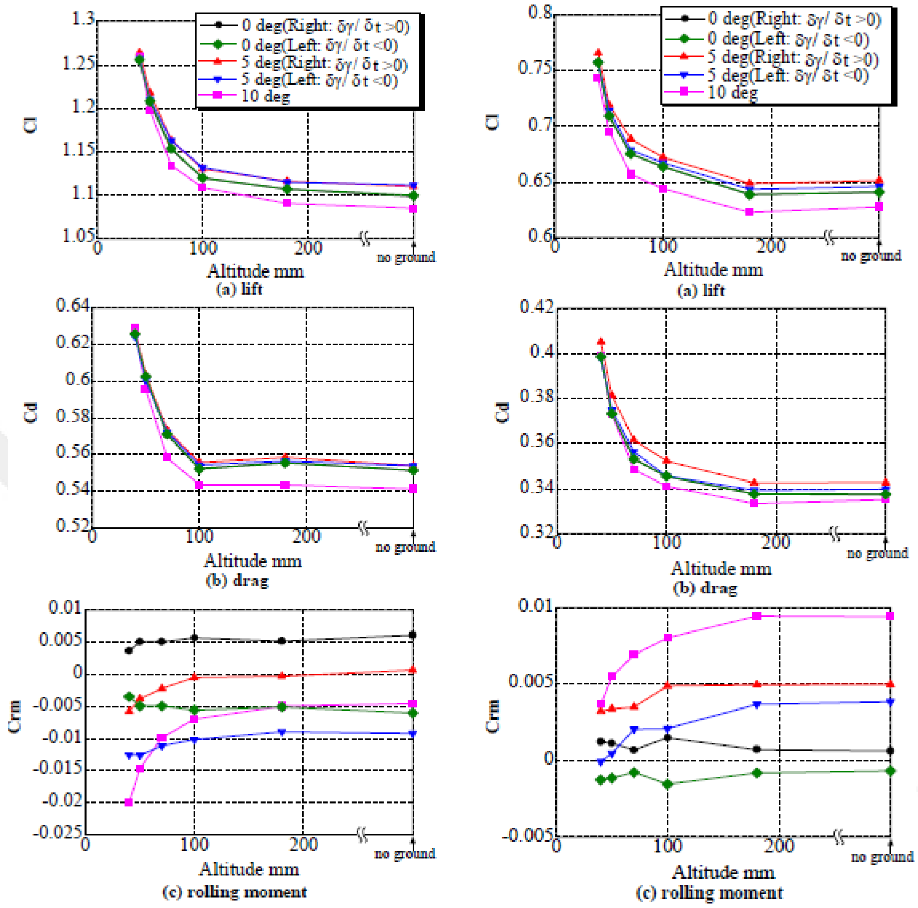

Figure 2.5. The impact of the ground on a) the lift, b) the drag and c) rolling moment coefficients of the wing-rock delta wing (Kawazoe and Morita, 2004)

Musaj and Prince (2008), in their experimental and numerical study in Figure 2.6, showed that an unconventional reverse delta wing with a W-shaped leading edge in the ground effect flow region is not very effective on the aerodynamic properties and thus the drag coefficient, C_D, when the delta wing approaches the ground surface. However, when the wing approaches the ground surface with a ratio of h/c=0.09, the lift coefficient, C_L, and indirectly the lift/drag ratio, C_L/C_D, are found to increase significantly compared to simple plane delta wings. The detected lift increment indicates that the coefficient of drag, C_D, is not subjected to a high rate of deviations with decreasing *h/c*. The main findings of the work suggest that when the reverse deltas wing descends to the flow region where the ground effect exists, strengthened vortices, earlier flow separations, and outboard tip vortex movement occur.

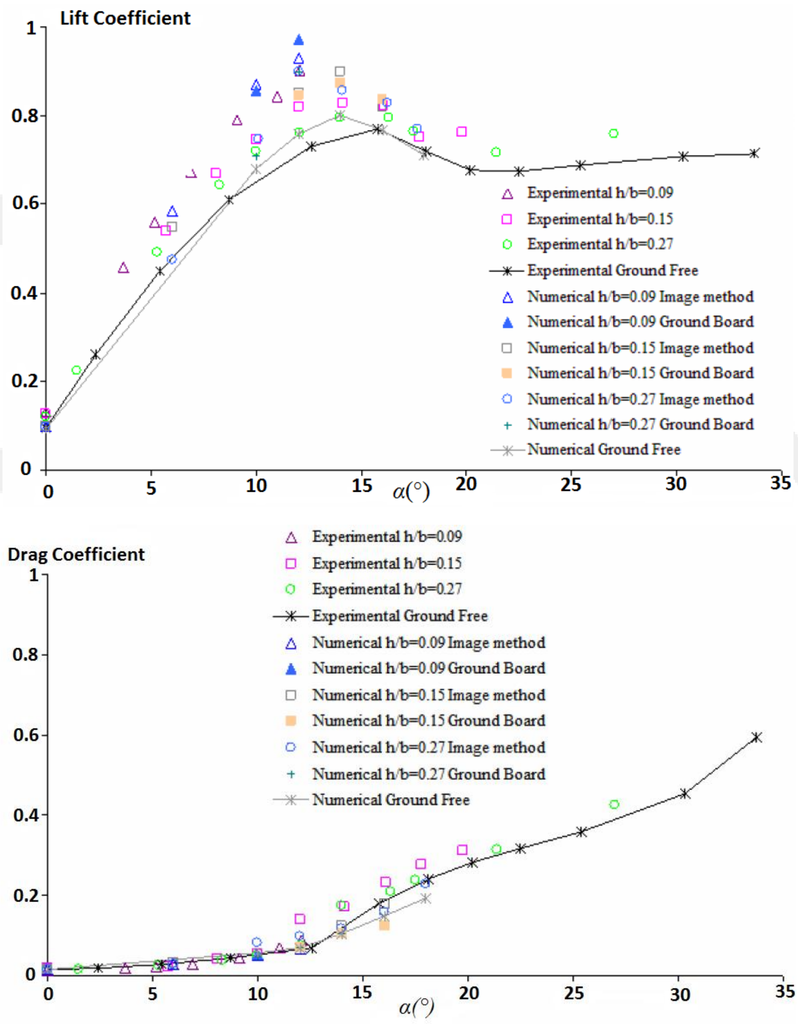

Figure 2.6. The numerical and experimental results of the ground effect on the aerodynamic features of a non-traditional reverse delta wing having W-shaped leading edges (Musaj and Prince, 2008)

Tumse et al. (2021) concluded that drag and lift coefficients, C_D and C_L, of the 40-deg-swept non-slender delta wing get higher at each angle of attack, α when the delta wing approaches the ground. It is found that the highest influential ground distance, h, nondimensionalized with chord length, c, is h/c=0.1 in terms of the performance of the aerodynamic features since the highest C_L/C_D ratio is obtained at h/c=0. 1It can be stated that an increase in aerodynamic performance occurs under the effect of ram pressure causing stagnation of airflow between the delta wing suction side and the ground surface as seen in Figure 2.7.

Figure 2.7. The ground effect on the location of vortex breakdown at α=8° and 11° for h/c=0.1, 0.4, and ground-free case (Tumse et al., 2021)

The influence of the ground on the flow detachment results in flow separations and vortical flow structures of rigid and membrane wings were examined by Bleischwitz (2018) to demonstrate that the GE induces expansion in the size of the tip vortex domain. Also, the movement from the central axis to the leading edge of the wing occurred with the strengthening of the GE. This movement limits the origination and growth of LEV.

The GE on the aerodynamic performance of a reverse delta wing which has several anhedrals was investigated by Lee and He (2018). It was concluded that aerodynamic coefficients, C_L and C_D enlarge with the anhedral positioned close to the ground at the wing trailing edge. Nevertheless, when the ground distance, *h/c* is 0.4 or less, the GE causes a significant increase in C_L. Besides, the increase in the lift force $F_L$was followed by the enhanced rotational speed and the vortex cycles. In summary, it is also stated that there is an outboard movement of the LEVs while the delta wing descends to the ground surface.

Lee and Ko (2018) experimentally investigated the ground effect on the structure of leading-edge vortices and aerodynamic loadings on a delta wing with a sweeping angle of Λ=65°. It is indicated that a significant increase in lift force, $F_{L,}$ and a relative decrease in drag force, $F_{D,}$ are observed when the wing moves close to the ground surface during take-offs and landings. As a result, it was found that both the lift force, $F_{L,}$ and the drag force, $F_{D,}$ increase with decreasing the ground distance. The significant rise in the lift force, F_L at a low angle of attack, *α,* and its rapid decrease with approaching the ground and raising the angle of attack, *α,* are observed. According to their study, the ground effect (GE) causes the development of stall to occur earlier and further magnifies the formation of leading-edge vortices with increased rotational speed and expends dimensions of LEVs. The smaller ground clearance caused the leading-edge vortices to be stronger and the earlier vortex breakdown formation. It is emphasized from the study that the most operational ground effect occurs at the ground distance/wing chord ratio of *h/c*=0.1. The large increase in drag coefficient, $C_{D,}$ and earlier breakdown of the leading-edge vortices can prevent widespread utilization of the delta wings.

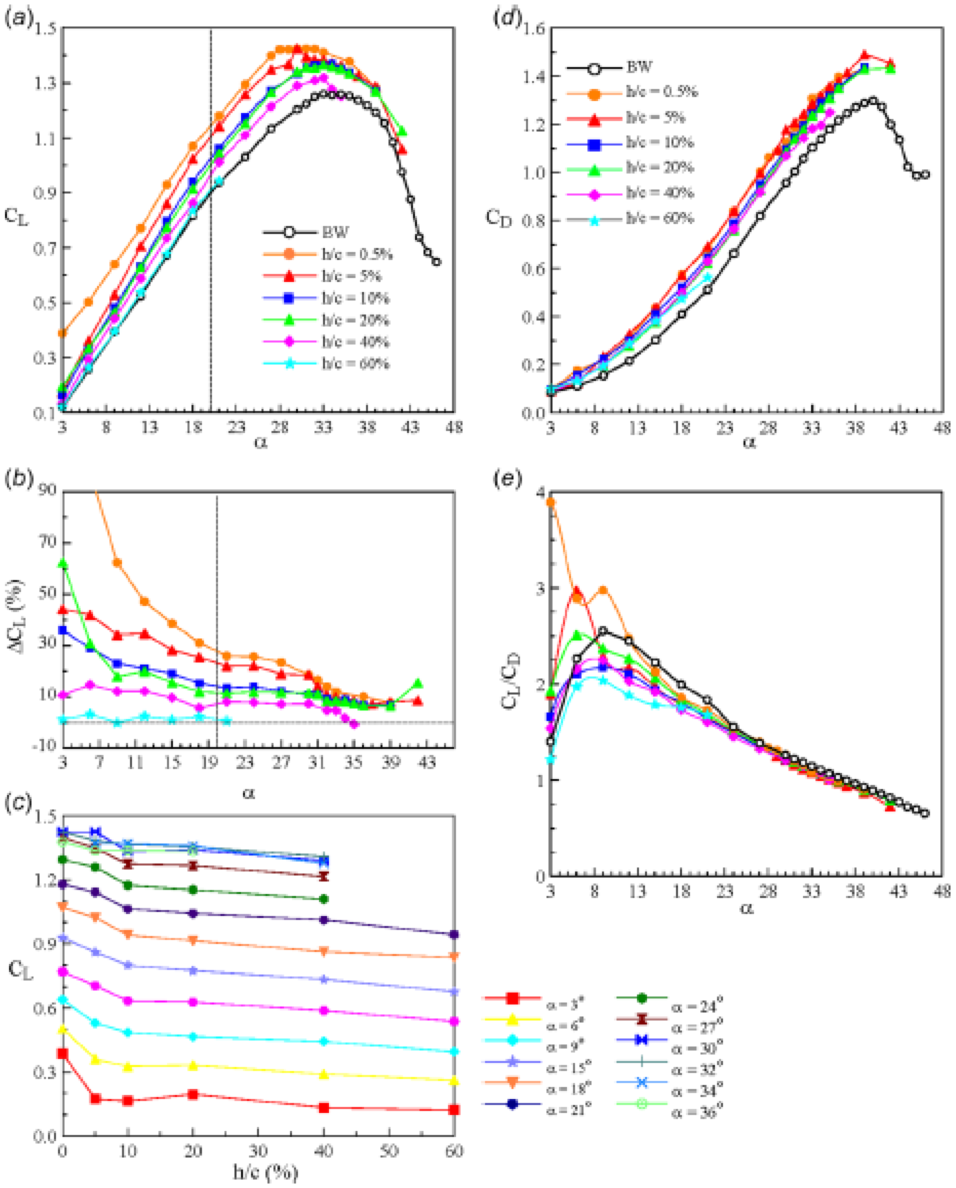

Figure 2.8. The ground effect on the aerodynamic features of the delta wing (Lee and Ko, 2018)

Flow structures and aerodynamic characteristics have distinctive features from the ground-free situation during landing and take-off operations. Despite its importance, the experimental studies related to the wing-ground surface interactions for double delta wings are limited. Before the main discussion, it is essential to review previous studies about the aircraft runway surface effects on the flow characteristics. It should be noted that the aerodynamic properties of a single delta wing and a double delta are also entirely different, in which delta wing-runaway surface interactions are generally studied for single delta wings. Unfortunately, there is no experimental data in the literature, particularly on the double delta wing aerodynamics under the ground effect.

The vortical flow formation over a double delta wing has been investigated to ensure the comprehension of the strake/wing vortices, and the vortex breakdown in the studies of Grismer and Nelson (1995), Pelletier and Nelson (1998), Karasu and Durhasan (2020). In addition, Durhasan and Karasu (2019) investigated the impact of the kink angle on the aerodynamic attitudes of a double delta wing having a 70° swept slender frontal part in the range of angle of attacks of $5° \leq \alpha \leq 35°$ and two Reynolds numbers of $1x10^4$ and $2.5x10^4$ using dye visualization method, qualitatively. It is seen that the interaction between the vortices of the frontal slender part and the posterior part is very high at a low angle of attacks and the kink angle affects very dominantly as shown in Figure 2.9.

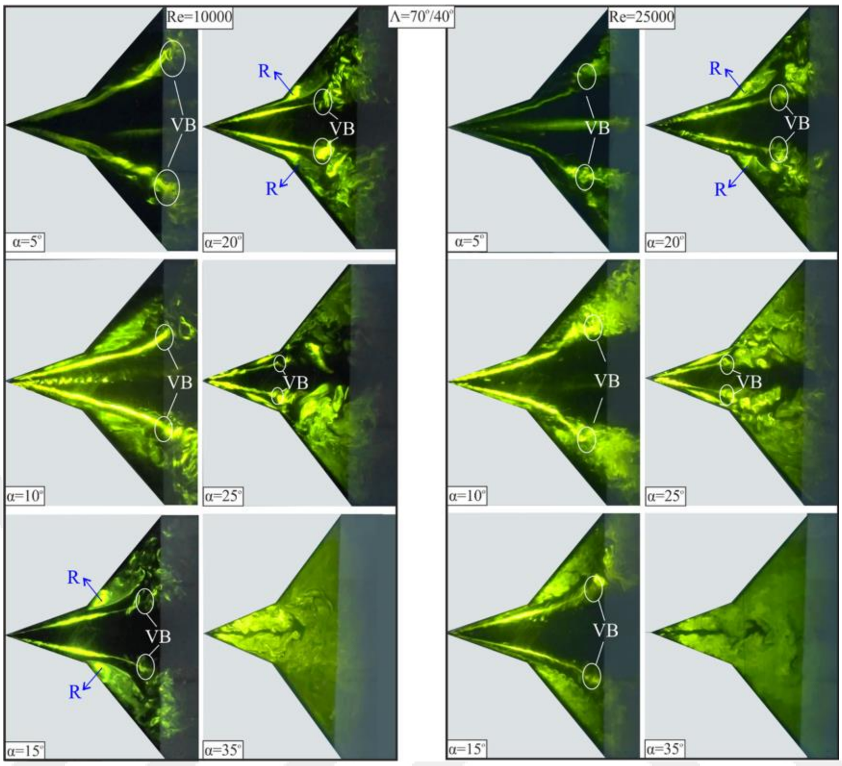

Figure 2.9. The interaction between the leading-edge vortices of the frontal slender part and the posterior part of the double delta wing at different α and *Re* (Durhasan and Karasu, 2019)

The aerodynamics of a cranked double delta wing having rounded and sharp leading edges with sweep angles of Λ=55°/30° were revealed by Manshadi et al (2016). They reported that the magnitude of the power spectrum density (DPS) reaches the highest value in the vortex core. In the case of the rounded leading edge, primary vortices are formed closer to the wing surface with weaker strength. The numerical studies on vortical flow structures of a double delta wing with Λ=80°/65° were performed by Liu et al. (2014) to demonstrate the instantaneous behavior of VB. It is predicted that locations of VB move forward and backward directions in random motion. The mode of VB transforms due to the variation of VB motion. In addition, the coefficients of moment, drag, and lift have a similar trend. In addition, the coefficients of the moment C_M, the drag, C_D, and the lift, C_L have a similar trend. The experimental work on the double delta wing having Λ=70°/50° in a wind tunnel using PIV to observe the binary structure of strake vortices was conducted by Zhang et al. (2016). Before the VB, both strake and wing vortices are wrapped around each other. Also, Zhang et al. (2017) studied a double delta wing having Λ=70°/50° to demonstrate the effect of bleeding and jet blowing. When the jet blowing is applied before the tip of the wing, the strake and wing vortices may be separated. Secondly, employing the jet blowing further downstream is observed to encourage interactions of strake and wing vortices, and hence, these two vortices are combined to form a consistent large vortex.

3. MATERIAL AND METHOD

3.1. Water Channel

Dye visualization and PIV measurements were carried out in the water channel installed in the Fluid Mechanics Laboratory of the Department of Energy Systems Engineering of Osmaniye Korkut Ata University. This water channel has an 8m length, 0.8m width, and 1m depth. It is made of 15 mm thick acrylic glass. There are two reservoirs in the water channel and one of them is located at the entrance and the other one is located at the exit of the water channel. Two centrifugal pumps circulate the water between these two tanks. These pumps have a frequency control unit to adjust the freestream velocity of water in the channel. The water passes through the flow regulator with honeycomb geometry, which is made of small cylindrical tubes before reaching the test section. The flow regulator is located at the 50% duct contraction region. The pump frequency controller was used to adjust the velocity of the free flow in the water channel. The uncertainty of velocity obtained by the PIV technique is conjectured to be within 1% (Ozalp et al., 2003). A schematic representation of the water channel is demonstrated in Figure 3.1.

Figure 3.1. Photographic representation of the water channel

3.2. Dye Flow Visualization and Particle Image Velocimetry (PIV) Experiments

3.2.1. Dye Flow Visualization Experiments

Dye visualization is a qualitative monitoring method to observe the vortical flow features in a well-defined area. In the dye visualization method, some amount of paint is dropped into the fluid flow and the dropped paint acts as a free stream. Dye visualization in the water channel is similar to the smoke visualization in the wind tunnel. It is possible to use ink, food, rhodamine, etc. as a dye. The dye powder is mixed with water at a reasonable ratio and it is released to the water channel via small-diameter circular hoses from the dye reservoirs. In the present experiment, Rhodamine 6G which changes color under the laser sheet was utilized as a dye. The dye experiments were performed in the side, cross-flow, and plan-view planes by using a continuous laser source. As seen in Figure 3.2, delta wings with a sweep angle of Λ=70° and 70°/40°, chord length of C=180mm, the thickness of t=5mm, bevel angle of 45° were used in all quantitative and qualitative experiments. Also, the schematic illustrations of the vortical flow structure over the slender and double delta wings were presented in Figures 3.3 and 3.4. The mirror with an angle of 45° to the flow is located about 900 mm (x/C=5), which is far enough from the flow behind the delta wing. A biaxial and remote-control traverse system was used to place the lasers in the correct position for the experiments. In this way, the abilities to move along the x and z axes are provided. The ground is made of a galvanized flat plate. The length of the ground plate was taken about 2800mm long enough to allow the development of the flow structures under the GE. In the current experiments, the static bases were used in both the water channel as well as a wind tunnel. Jones (2005) reported that the stationary base wall is reasonable if the space between the ground surface and the pressure surface of the delta wing is not very low. SONY HDR-PJ410 video camera was used to record vortical flow structure over the wing and the Play Memories Home program was utilized to capture photos from the videos. During the dye flow visualization experiments, the Reynolds number was taken as Re=2.5x10^4 based on the chord length. The corresponding free stream velocity, U_∞ is 142 mm/s. The angle of attack was chosen as α=15° and 25° for the double delta wing and α=25° and 35° for the slender delta wing at different normalized ground distances such as; h/c=0.55, 0.25, 0.10, and ground-free effect (GFE) case. The GFE (Ground free effect) abbreviation presents the ground-free situation; that is the case that the ground effect diminishes completely, and thus the flow structures or aerodynamic properties are not changed since the ground effects are eliminated at a location, h/c=1.5. The reason for selecting these angles of attack, α, is that the collapse point of the leading-edge vortex occurs near the rear edge of the wing, and thus the position of this collapse point changes sensitively even with the small ground effect for the slender and double delta wings. As seen in Figures 3.5 and 3.6, schematic and photographic illustrations of the setups of the dye visualization and the PIV experiments are presented.

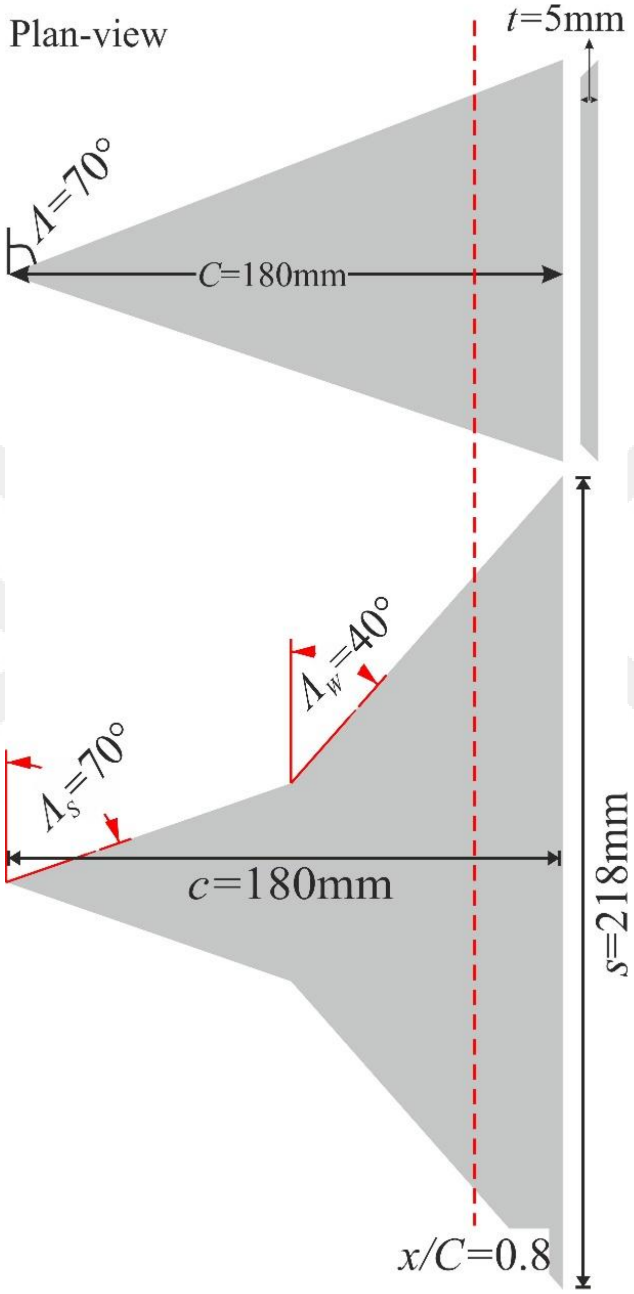

Figure 3.2. Definitions of the dimensions of the slender and the double delta wings

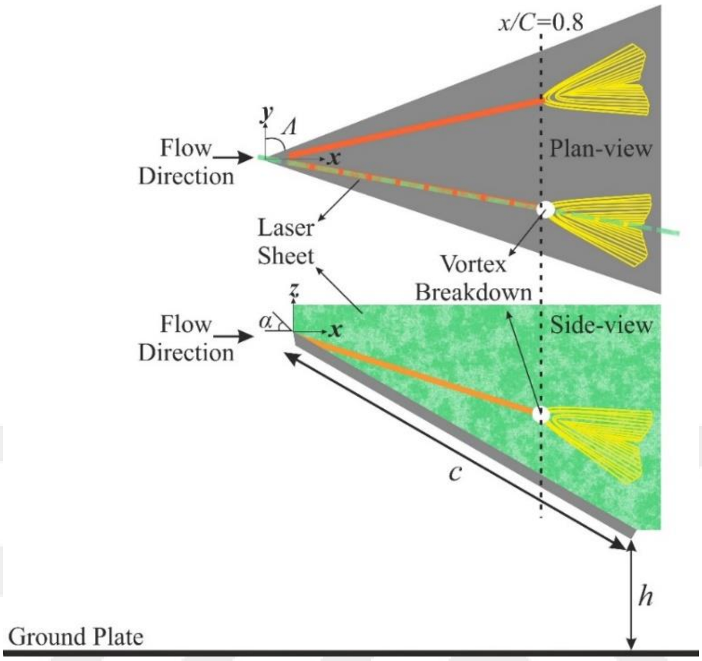

Figure 3.3. The identification of the flow structure over the slender delta wing under the ground effect

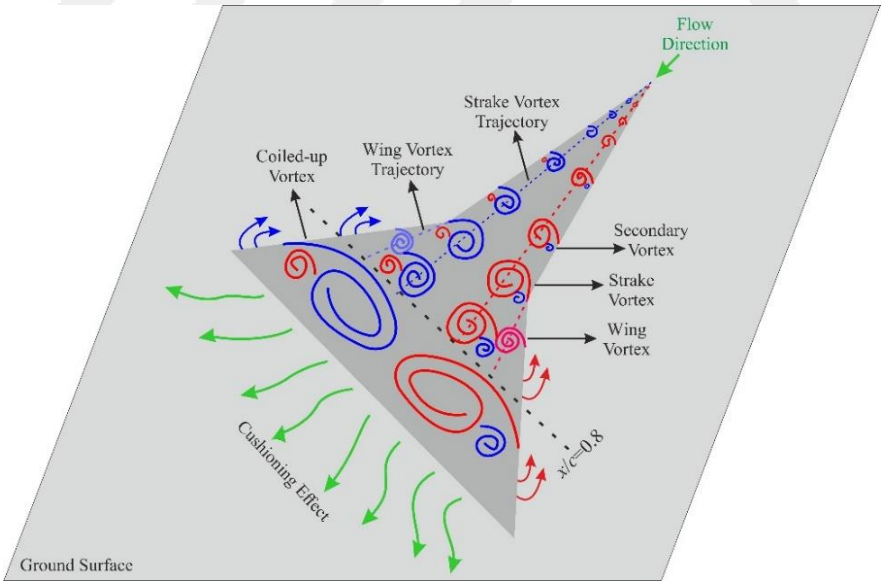

Figure 3.4. Schematic illustration of the vortex types over the double delta wing under the ground effect

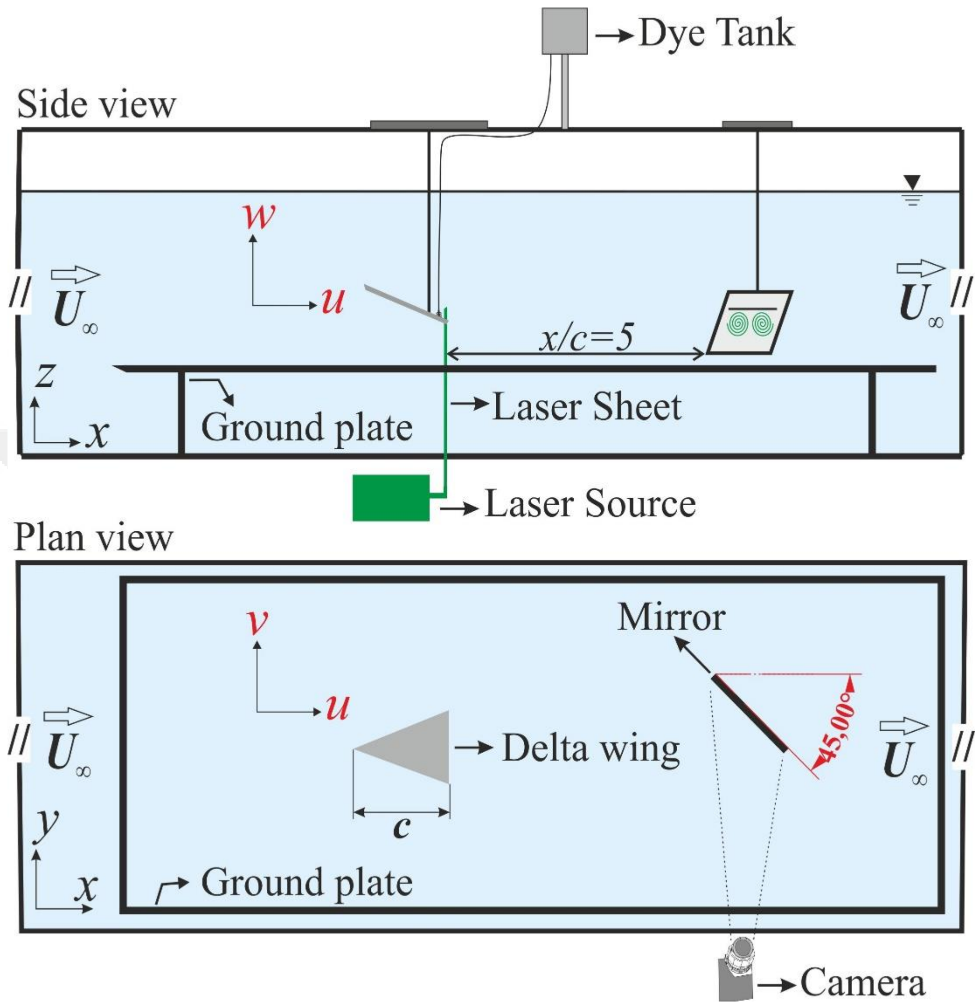

Figure 3.5. Schematic representation of the experimental setup in the water channel in side-view and plan-view planes.

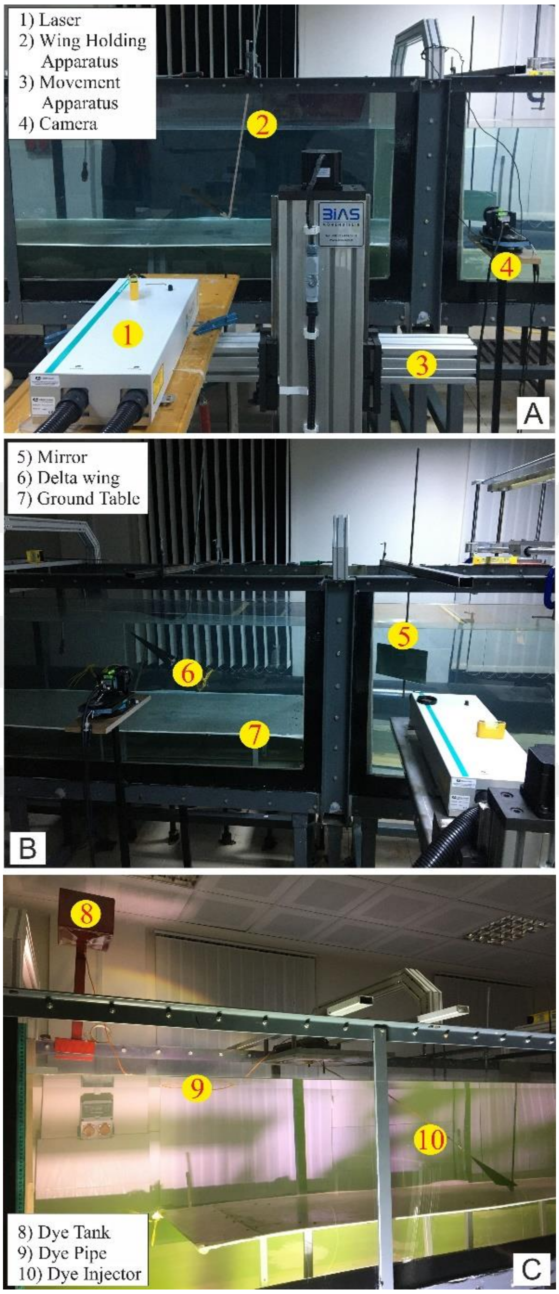

Figure 3.6. Photographic illustration of a) and b) the experimental setup for the PIV method in the end-view and side-view planes, c) the experimental setup for the dye visualization method

3.2.2. Particle Image Velocimetry (PIV) Experiments

In fluid mechanics research, it is crucial to analyze and comprehend the flow structure and characteristics by performing instant measurements for a specific flow region under turbulent flow conditions. Single point velocity measurement is possible in a specified flow zone with different velocities such as hot wire or Laser Doppler Anemometer (LDA). While measuring the velocity of different points with these existing methods, it is necessary to make measurements at different times for each point whose velocity will be measured and as a result, the average flow characteristics will be determined. However, the instantaneous flow characteristics at different points in a given time cannot be determined. Thus, this deficiency does not allow us to predict the nature of the flow. To overcome these deficiencies, the instantaneous velocities of the vortical flow with complex geometry can be measured simultaneously in the planar region and the flow characteristics can be accurately determined with the help of Particle Image Velocimetry (PIV) as seen in Figure 3.7. Besides, having a large application area and importance in aerodynamic and hydrodynamic research and not interfering with the flow while taking the necessary measurements gives the PIV method a very important advantage.

The water and the air are used as the fluid in most of the studies in the literature within the scope of flow analysis with the PIV method. The experiments required for flow analysis are carried out in an open water channel system operating as a closed-loop system. To be able to analyze the flow characteristic and measure the velocity with the PIV technique, the particles of plastic with a diameter of 20 μm, whose density is almost the same (varying in the range of 1000-1100 kg/m^3) as the density of water, are added into the flow. The single point laser light produced by the 120 Jm double-pulse laser source (Nd: YAG Laser-neodymium-doped Yttrium Aluminum Garnet) becomes the laser beam of 1-2 mm thickness and different widths with the help of optical lenses. Nd: YAG-type lasers have common usage in PIV applications due to the fulfillment of the required conditions as stated in the study of Tunay (2011). Dual Power 145-15 is the double pulsed PIV laser which has 120 mJ pulse energy at 532 nm wavelength (Nd: YAG laser) and works with CCD camera-based systems. The laser source can produce a maximum of 15 pairs of laser beams per second. In addition, the Litron LPU550-PIV twin power supply can allow 200 Jm outputs from each laser at a wavelength of 532 nm at 15 Hz. A CCD digital camera with a resolution of 1600x1200 and a maximum shooting speed of 299 FPS (frames per second) was used to capture images. The number of images was taken as 1000 for each set of PIV measurements.

Illuminated by laser beams, the flow is transferred to the computer by two images of particles moving in the flow field, taken at a certain time interval, Δt with a CCD (Charge Coupled Device) camera. The time interval, Δt between the two images depends entirely on the flow's speed and turbulence level. The time interval, Δt between the two images depends entirely on the flow's speed and turbulence level, and it was adjusted as Δt=5260μs in the current study. Due to the pulsed laser source, the laser and the camera must work in combination. The device that provides the combination between the laser source and the CCD camera is called a synchronizer and is controlled by a computer. The CCD cameras are used which formed a series of detectors called a pixel. They must work synchronal with a laser system (Karasu, 2015). In the flow field, in other words, the measurement plane is divided into symmetrical partial areas to form the network structure and each section is called a pixel. The distribution of the particles in the pixels in this measurement plane is also very important. Because each pixel of the image plane should contain a certain amount of particle for the correlation process or low error rate instantaneous velocity measurement. Each pixel or interrogation area must include almost 15-20 particles, otherwise, the error rate of the measurements can be high (Ozgoren et al., 2008). These images transferred to the computer are mostly divided into small sub-regions of 32x32 pixels (these dimensions can be reduced or increased when necessary) and the displacement of the particles in each sub-region is calculated using the Fast Fourier transform. Since the time interval, Δt between both images, and the average path traveled by the particles in each sub-region are known, the flow velocity is calculated. After the flow velocity is calculated, the number of vectors in the flow field is calculated by the program. Bad vectors with a small amount of these vectors calculated by the PIV program are found with the help of special software and these vectors are removed from the flow region. Instead of the bad vectors removed by the special software, new vectors are replaced using the least-squares method (bi-linear interpolation) by using the vectors in adjacent pixels. Besides, the compatibility between vectors is achieved by using the Gaussian correction method propounded by Reuss et. al (1989).

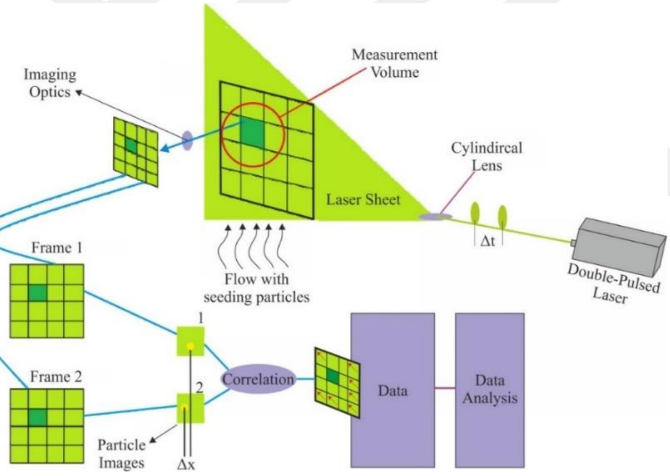

Figure 3.7. Schematic representation of the working principle of PIV

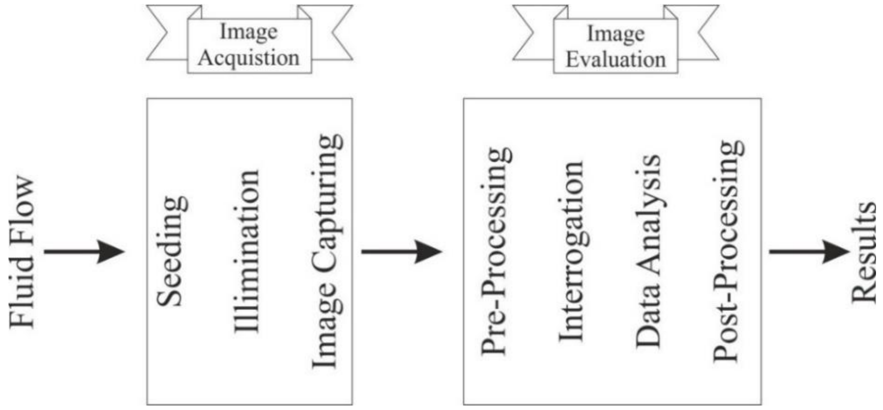

Figure 3.8. Processing steps in PIV application software

First, the delta wing is placed in the water channel and its position is decided according to the image to be taken. Depending on this determined location, the laser location is adjusted and fixed according to the position where the laser will illuminate. Next, the CCD camera is placed perpendicular to the laser light section. The camera focus is adjusted according to the particles by using the shining of the particles in the flow under the laser. Then, a ruler is placed on the delta wing and one photograph is taken. The actual image area is determined using the scale on this ruler. Although two basic principles of PIV are based on the direct determination of velocity and time dimension, this technique initially measures the velocity of particles in the fluid. Therefore, it should be paid attention that the properties of the particles and the movements of the fluid and particle do not differ greatly. While the ideal particles scatter enough light, they follow the motion of the fluid precisely and do not change the flow characteristic. These particles should be small enough to fully monitor the flow, but also large enough for the camera to detect. They must also have nearly the same density as the fluid. This will allow the system to estimate particle positions and displacements based on subpixel sensitivity, thereby effectively increasing the resolution technique. In this study, 20 μm size polyamide-coated particles were used. The density of the particles in the flow is important to achieve a good signal peak in cross-correlation. At least 10 to

25 particles should necessarily be visible in each imaging area. Therefore, if necessary, particles should be added again. After this process, the imaging process is started. A CCD camera having a 60mm NIKON optical focal lens is used for image capture. The laser and CCD camera work together with the help of a synchronizer. An image is obtained as a result of each pulse of the double-pulse laser. These images are converted into a single image as a result of processing the images with the help of cross-correlation.

The Particle Image Velocimetry (PIV) process determines and records the distance the particles move based on the lighting generated by laser pulses based on photography. The most common methods for determining this distance are particle tracking or correlation. The main advantage of the cross-correlation process over autocorrelation: displacement is achieved without any directional ambiguity. The correlation peak signal carries more signal strength and is therefore immune to interference. The main disadvantage of cross-correlation is; that calculation is more difficult and time-consuming because cross-correlation requires a two-dimensional Fourier transformation instead of a one-dimensional. After the images are cross-correlated, post-processing is applied to eliminate bad vectors in the image. Bad vectors cause undesirable effects on the image. It is cleaned with the help of the Cleanvec program written by Meinhart and Soloff (1999). After these processes are completed, outputs such as velocity components, streamline, vorticity, velocity fluctuations, turbulent kinetic energy, and so on are obtained with the help of several data processing software.

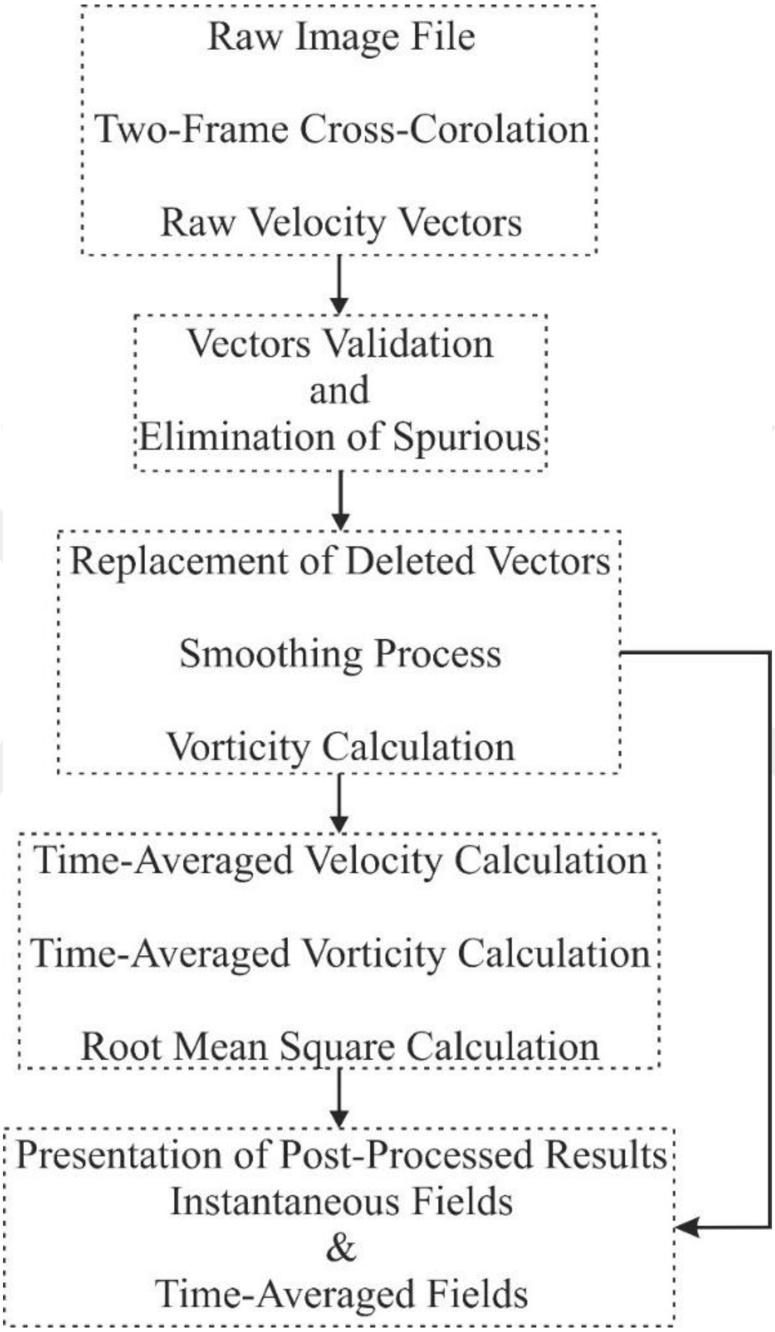

Figure 3.9. Post-processing steps of PIV measurements.

3.3. Wind Tunnel Experiments

The measurements of the aerodynamic properties of the delta wings in the wind tunnel were performed in the Fluid Mechanics Laboratory of the Department of Mechanical Engineering of Niğde Ömer Halisdemir University. The schematic representation of wind tunnel experiments can be seen in Figure 3.10. The airflow comes to the test area of 570mm *x* 570mm square cross-section and 1000mm in length where the test models and measuring elements are located. There is a transducer to convert the 580mm *x* 580mm square zone at the end of the test section to the circular section and to equalize the fan diameter. By using a vibration suppressor, the vibrations from the fan are eliminated. The engine of the fan, which provides flow in the tunnel has a power of 4 kW and has a diameter of 700mm. The air inside the tunnel is discharged from the outlet hose into the atmosphere. To obtain the desired speed in the test zone, the revolution of the fan motor is controlled by the electric current frequency converter. The pitot tube was used to control the desired speed for the experiments. The turbulent intensity of the wind tunnel is lower than 0.1%. Telemecanique Altivar 71 brand (11 kW) frequency converter control unit is used in the range of 0-50 Hz with a 0.1 step size to achieve the desired speed. The required forces, F_L and F_D were measured to determine the lift and drag coefficients, C_L and C_D using the formulas:

$$C_L = \frac{F_L}{0.5\,\rho\,{U_\infty}^2\,A}$$

$$C_D = \frac{F_D}{0.5\,\rho\,{U_\infty}^2\,A}$$

where ρ (kg/m^3) is the density of water, U_∞ (m/s) is the free stream velocity, A (m^2) is the projection area with the help of F_L and F_D values received by a load cell. The turbulence intensity of the wind tunnel was measured below 0.1%. Also, the uncertainty of the measurements of the performance characteristics of the delta wing was calculated lower than 5% as specified by Akbiyik et al (2017).

The air velocity was taken as 10.6 m/s corresponding to the Reynolds number of $Re=1\text{x}10^5$ based on the chord length of the delta wing, c. The measurements of the aerodynamic properties of the delta wings were carried out at angles of attack within the range of $5°\leq\alpha\leq45°$ with the step sizes of 3° and 5° depending on the importance of the measured angle of attack, in other words, it was aimed to detect the stall angle under the ground effect by taking it at more frequent intervals as the angle of attack approaches and passes the stall region. The normalized ground distances were taken as h/c=0.1, 0.25, 0.55, and the GFE case.

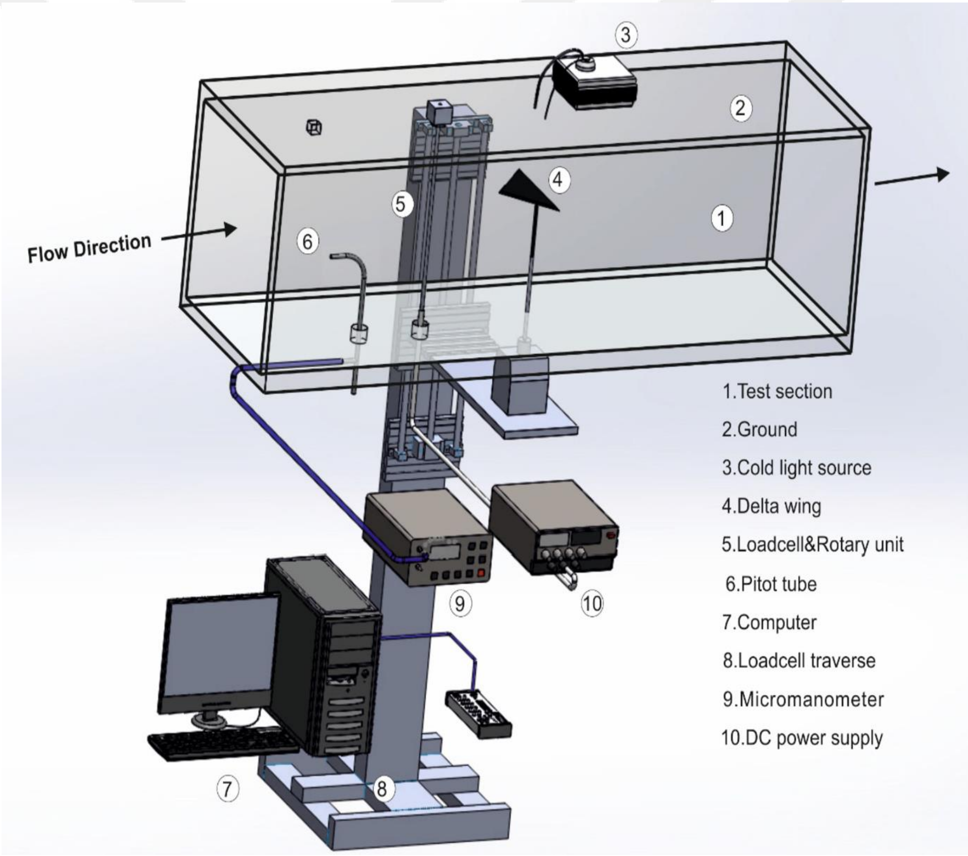

Figure 3.10. Schematic representation of experimental set-up in the wind tunnel (Tumse et. al, 2021)

4. RESULTS AND DISCUSSION

4.1. The Ground Effect on the Slender Delta Wing

Figure 4.1 demonstrates the GE on the change of VB location and the interaction of vortices with the wing's surface at an angle of attack, α=35° for different nondimensionalized distances, *h/c*= 0.1, 0.55, and the GFE case using the dye visualization method. The dye visualization experiments in the end-view plane were taken at *x/c*=0.8. As seen in Figure 4.1, the earlier breakdown location of the LEVs was detected over the wing under the GE compared to the GFE case. For instance, while the leading-edge vortices break at mean positions *x/c*=0.55 and 0.64 for *h/c*=0.55 and GFE case, respectively, the leading-edge vortices break at *x/c*=0.49 for the delta wing under GE for *h/c*=0.10. The GE induces an earlier breakdown of LEVs due to an increase of adverse pressure gradient on the suction side of the delta wing along the chord direction. In Figure 4.1, the distance between the LEVs and the delta wing surface is denoted as *z*, and it is normalized with the span length of the wing, *s*. While the distance of *z/s* is equal to 0.052 for the slender delta wing at *h/c*=0.10, the ratio of *z/s* is 0.057 and 0.069 for *h/c*=0.55 and GFE case, respectively. It shows that the distance between the LEV and the surface of the delta wing, *z/s*, decreases when the wing moves from the GFE region to the extreme ground region, *h/c*=0.1. In other words, the interaction between the LEV and the wing's surface diminishes when *h/c* increases. Dye visualizations, which reveal influences of GE on the LEV size and structure in an end-view plane, are also presented in Figure 3 for *h/c*=0.10, 0.55, and GFE cases at α=35°. Here, well-defined primary and secondary vortices were detected on the suction side of the delta wing. The secondary vortices with opposite signs of primary vortices occupied the delta wing's upper surface due to boundary layer separation. As observed from the Figure, the size and extent of primary and secondary vortices enlarge when the delta wing lowers from the GFE field into the GE field, i.e., from *h/c*=0.10 to 0.55 as a result of earlier VB compared with the GFE case. The GE induced larger size of the LEVs is coherent with the earlier VB over the suction surface of the delta wing for both side and end-view planes. Also, in Figure 4.2, the GE on the diameter of the primary vortex, d_{pv}, normalized with the span length, s is demonstrated at α=35°. The ratio of d_{pv}/s is the ratio of diameter, d_{pv}, from the primary vortex core to the span of the wing, s as stated in Hall (1961). It is revealed that the diameter of the primary vortex enlarges when the wing approaches the ground as a result of the GE, which induces earlier VB. For instance, when the normalized diameter of the primary vortex core was found as 0.172 for the unrestricted flow field, it gets higher to the value of 0.198 in GE with h/c=0.1.

In Figure 4.3, the GE on the expansion of the Leading-edge vortex core is demonstrated at α=35° and x/c=0.8 for h/c=0.1, 0.55, and GFE case. As indicated in Figure 4.3, y is the distance between the core of the primary vortex and the leading edge of the delta wing. It is normalized with the span length s of the slender delta wing. Figure 4 is drawn based on the vortices passing through the wing’s leading edge. As seen in Figure 4, the GE gives rise to the inboard movement of LEVs, which means that both LEVs move from the leading edge toward the wing's central axis. For instance, while the normalized distance, y/s, is measured as 0.082 for the delta wing out of the GE field, the y/s is measured as 0.093 and 0.108 for h/c=0.55 and 0.1 at α=35°, respectively. The inboard movement of vortex trajectory with the GE could be dependent on the greater ram pressure applied over the rear side than on the delta wing's front side. The inboard movement of vortex trajectory by GE was also pointed out in the studies of Lee and Ko. (2018) and Qu et al. (2015).

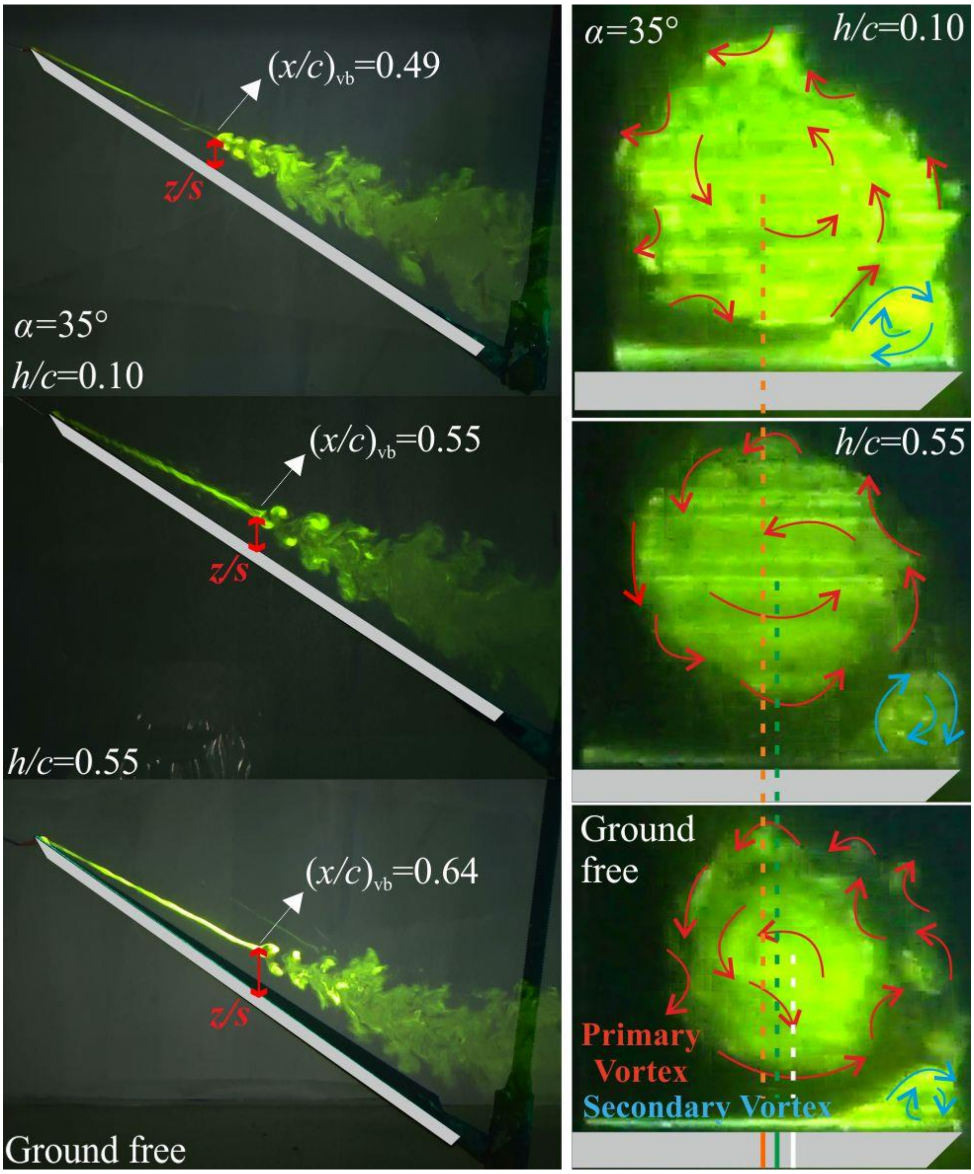

Figure 4.1. The ground effect on the expansion of the leading-edge vortices and visualization of the size and structures of the leading-edge vortices in the end-view plane at α=35° and x/c=0.8 for h/c=0.1, 0.55, and the ground-free effect case

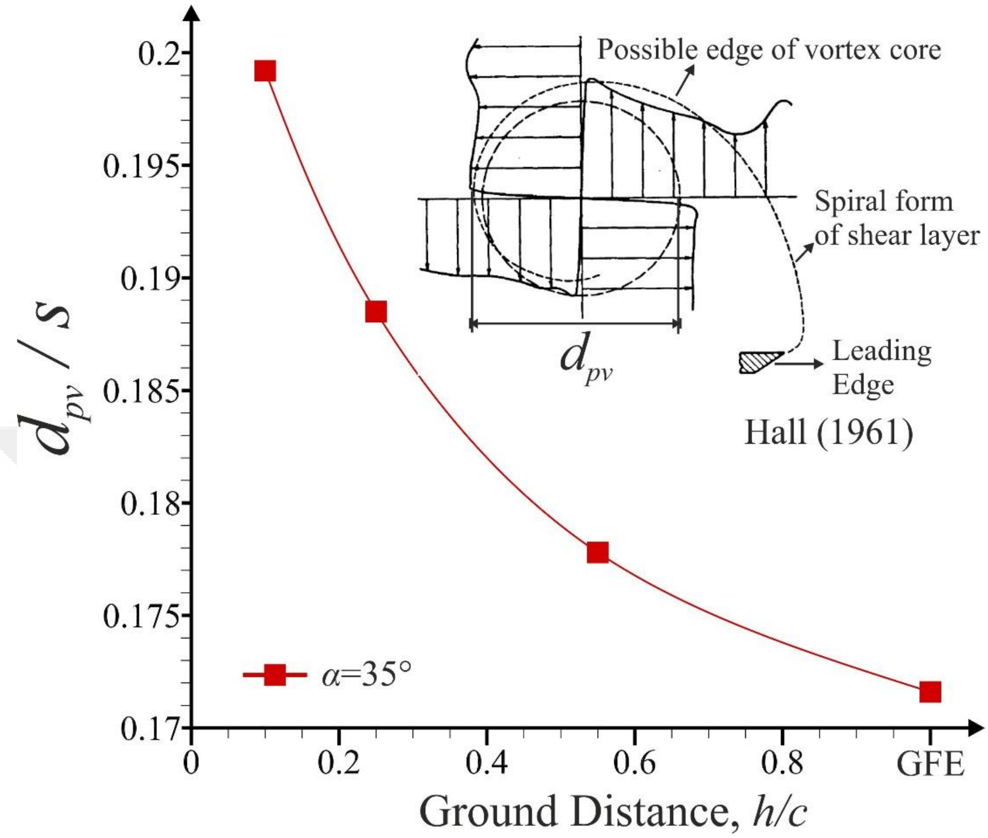

Figure 4.2. The representation of the drawing (Hall, 1961) and the variation of the diameter for the primary vortex under the ground effect for *h/c*=0.1, 0.25, 0.55, and the ground-free effect case

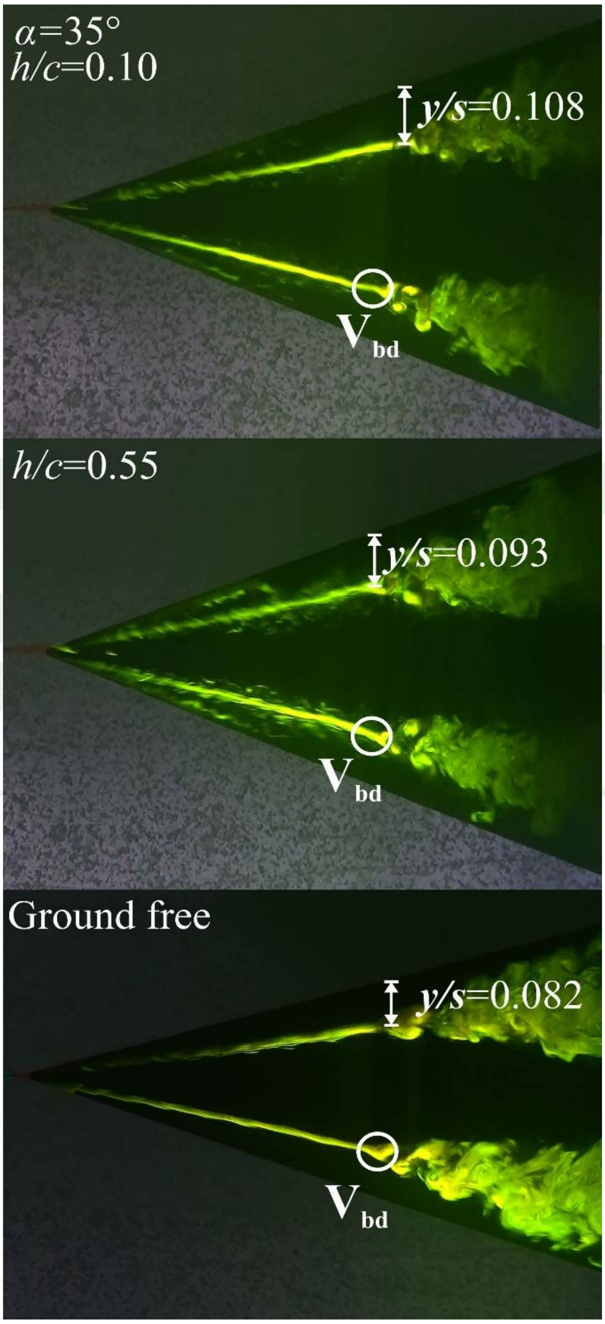

Figure 4.3. The movement of leading-edge vortices in plan-view under the ground effect at α=35° for h/c=0.1 and 0.55 and the ground-free effect case

Figure 4.4 depicts the GE on contours streamlines based on time-averaged velocity distributions at α=25° and 35° for *h/c*=0.1, 0.25, 0.55, and the GFE case. Here, *F* is used to define the location of the foci of the LEVs. As realized from Figure 4.4, the GE causes the inboard movement of the LEV along the spanwise of the delta wing, which means the focal points, *F* of the LEVs, move toward the wing's central axis when the delta wing approaches the GE field closely, for example, *h/c*=0.1. In addition, the core region diameter of the time-averaged streamlines at α=35° increases with lowering the ground distance, *h/c,* which is coherent with the GE induced earlier VB. Because the LEVs expand during the VB phenomena. Thus, earlier VB in GE, which is also denoted in Figure 4.1, causes an increment in the size of LEVs with GE. Since the slender delta wing is in the pre-stall field, α=25°, the change in the size of the leading-edge vortex core region is not as pronounced as the change in the post-stall region, α=35° although there is a slight enlargement in the vortex core region at α=25°. However, it has been observed that the outer vortex region expands as a result of the VB moving towards the delta wing tip when the ground proximity increases at α=25° as seen in Figure 4.4. In Figure 4.4, the distance between the delta wing surface and the focal point is denoted as *z*, and this, *z*, is nondimensionalized with the delta wingspan length, *s*. The vertical dimensionless distance, *z/s* from the focal point to the surface of the delta wing, decreases when the ground proximity increases, causing significant interactions between the intensified LEV and the turbulent boundary layer that developed over the wing's surface in the case of *h/c*=0.1 compared to the unrestricted flow field. Furthermore, the focal area size expends by lowering the ratio of *h/c*, which is coherent with the GE inducing the earlier breakdown of the LEVs.

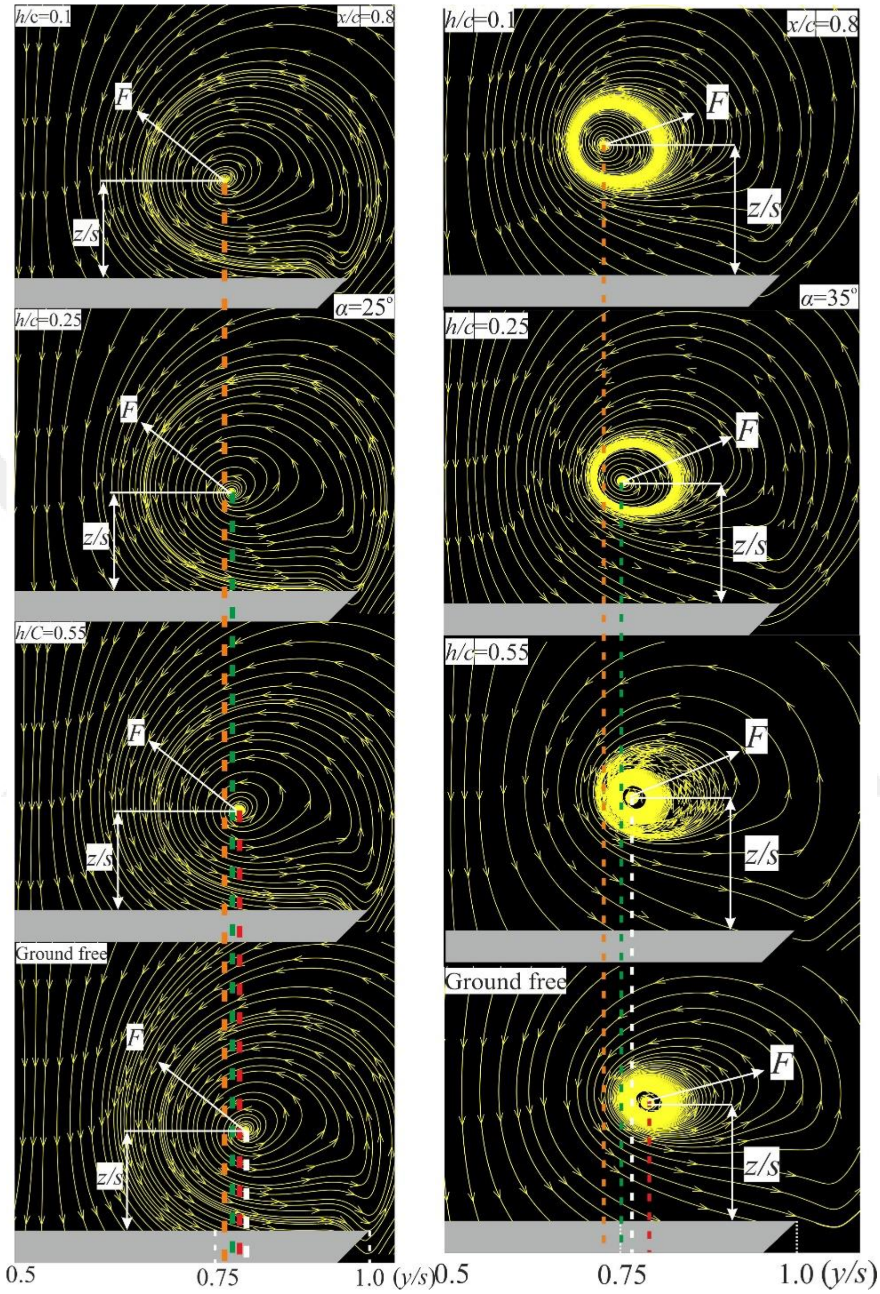

Figure 4.4. The time-averaged streamline patterns in the end-view plane under the ground effect for *h/c*=0.1, 0.25 0.55 and the ground-free effect case at *x/c*=0.8 and the angles of attack of *α*=25° and 35°

Figure 4.5 demonstrates the GE on the time-averaged streamline patterns for *h/c*=0.1, 0.55, and GFE case at α=35° on the side-view plane. The experiments on the side view plane were not carried out along the chord of the delta wing, only focused on the VB region (one-third of the chord length). The VB locations can be examined in Figure 4.1. In Figure 4.5, the distance, *z* between the VB location and the delta wing surface is nondimensionalized with the delta wingspan length, *s* as *z/s*. The dimensionless vertical distance, *z/s*, between the VB location and the surface of the delta wing decreases when the ground proximity increases. In other words, the fluid-structure interaction gets higher as the delta wing approaches the ground. For instance, while the vertical distance between VB's location and the wing's surface is detected as z/s=0.174 in the GFE case, the nondimensionalized distance descends to z/s=0.158 0.147 when the slender wing lowers to *h/c*=0.55 and 0.1, respectively. In addition, an increase in interactions between the delta wing surface and vortical flow leads to an increase in irregularities as a result of the earlier VB. These flow structures mainly cause aggressive unsteady flow behaviors, which may result in vibrating wings causing retardation of aerodynamic performance. Hence, the control of the aircraft aerodynamics can be adversely affected by unstable flow load buffetings as also reported by Gursul (2005). Also, the vortex symmetry is seen at α=35° under the GFE case. However, the vortex symmetry and coherency are observed to deteriorate as the delta wing moves from the unrestricted flow field into the GE field.

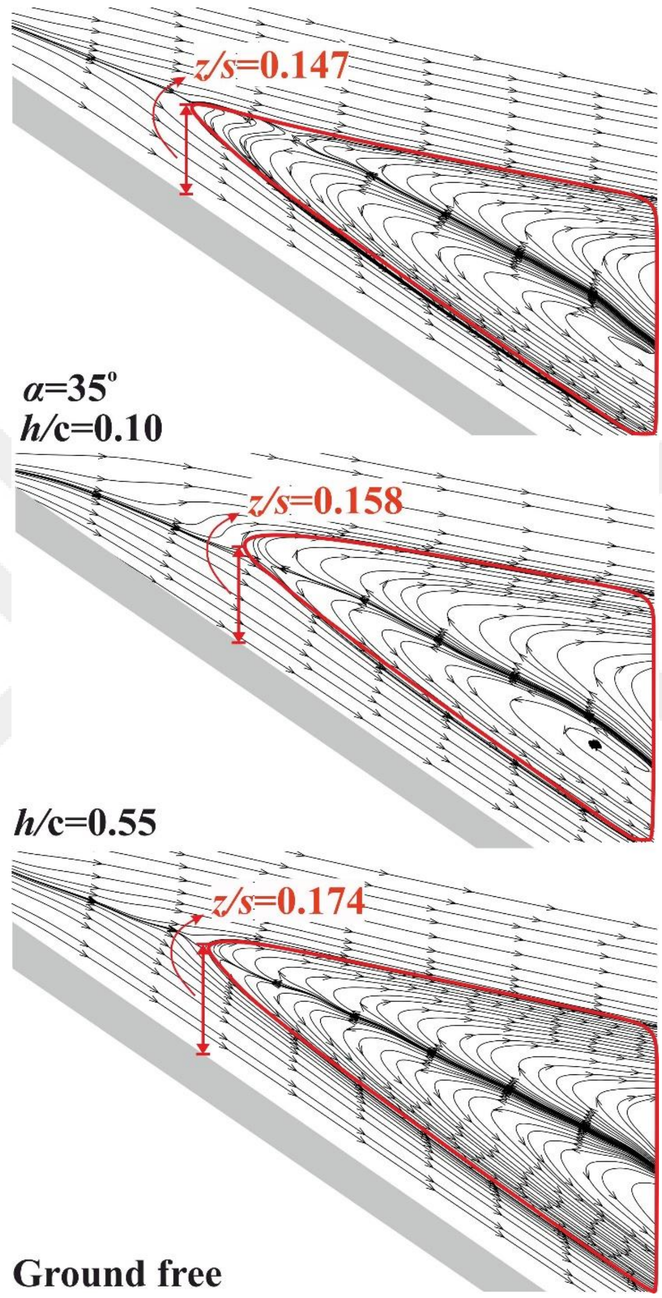

Figure 4.5. The variation of the time-averaged streamline patterns in the side-view plane under the ground effect for *h/c*=0.1, 0.55, and the ground-free effect case at *α*=35°

Figures 4.6 and 4.7 demonstrate the ground effect on the structure, distribution, and magnitude of LEV concentrations, $w*$ at α=25° and 35°. Primary and secondary vortices were prominently detected over the slender delta wing. The secondary vortices are vortices that swirl in the opposite direction of the primary vortices and are formed due to the separation in the boundary layer thickness caused by the interaction between the primary vortices and the surface of the slender delta wing. The secondary vortex rotates in the opposite direction of the primary vortex and is formed due to boundary layer thickness separation caused by the interface between the primary eddies and the boundary layer of the slender delta wing. The value of the LEV concentration is normalized in the equation as:

$$w^* = \frac{wc}{U_\infty}$$

The peak value of the LEV at the location detected, in other words, in the region very close to the leading-edge of the slender delta wing on the suction surface, diminishes as the height of the delta wing is lowered towards the ground. Furthermore, the maximum value of the concentration in the core region of the LEV attenuates gradually when the ground distance decreases, as seen in Figure 4.6. For instance, the dimensionless vorticity of primary and secondary vortices is detected as 95.73 and -30.71 in the GFE case. Also, it is seen that the values of the primary vorticities, $w*$ gradually decrease such as $w*$=91.98, 85.43, and 72.15, and also, the magnitudes of secondary vortices decrease such as $w*$=-29.28, -28.14, and -26.89 at h/c= 0.55, 0.25 and 0.1, respectively. The decrease in the peak value of LEV concentration with the GE is also observed at α=35° as seen in Figure 4.7. This situation may be due to the lack of sufficient space between the delta wing and the ground for the flow to develop adequately. This, in turn, causes the inhibition of LEV formation. Also, the reduction in the value of the peak concentration of the leading-edge vorticity may be due to GE causing the earlier onset of VB because of the increment in the reverse pressure gradient between the upper and lower sides of the wing. Besides, it is seen that the intensity of $w*$

decreases for both primary and secondary vortices with increasing the angle of attack, from α=25° to 35°, under the case of the GE induced earlier VB. The GE induced earlier VB on the time-averaged dimensionless vorticity concentration in the side-view plane can be also seen in Figure 4.8 as a result of the enhancement in the adverse pressure gradient between the surface of the slender delta wing and the ground. The colors represent the motion direction of the vortices as clockwise (CW) for blue and counter-clockwise (CCW) for red. The motion direction is also valid for Figure 4.9. As seen from Figure 4.9, the GE on the instantaneous streamline patterns for extreme ground and GFE cases in the side-view plane at α=35° was conducted. F^- and F^+ define the focal points that move in clockwise and counterclockwise rotation, respectively. It is indicated that the interaction between the wing surface and the vortical flow structure increases when the delta wing descends to the ground field. While the Kelvin-Helmholtz (K-H) vortices, F^+ and F^- move in a certain order without the ground effect, the order deteriorates as the delta wing gets closer to the ground. However, the instability and the irregularity of K-H vortices increase as a result of the interaction between the wing surface and the LEV when the ground distance, *h/c* decreases.

Figure 4.10 demonstrates the GE on the instantaneous streamline patterns for *h/c*=0.1 and GFE case at α=35° and *x/c*=0.8 on the end-view plane. The instantaneous frames were captured to present patterns of streamlines at three different times for both *h/c*=0.1 and GFE cases. As seen in Figure 4.10, the size of the LEVs is significantly extended when the delta wing altitude is lowered towards the ground. While the LEV diameter is visible within the image area for the GFE case, the LEV diameter expands much further out of the focused region as it gets too extended in the case of *h/c*=0.1. As a result of instability and increased interaction between the LEV and the delta wing surface, multiple focal points, F_{m}, are observed at *h/c*=0.1. As seen in Figure, the complex flow structure is observed for the wing in extreme GE due to the multiple focal points, F_m and deterioration of vortex coherency, and increased interaction between the delta wing surface and the

LEV. Also, the inboard movement of the focal area of the instantaneous streamlines occurs with reducing in *h/c*, which is coherent with the time-averaged streamlines.

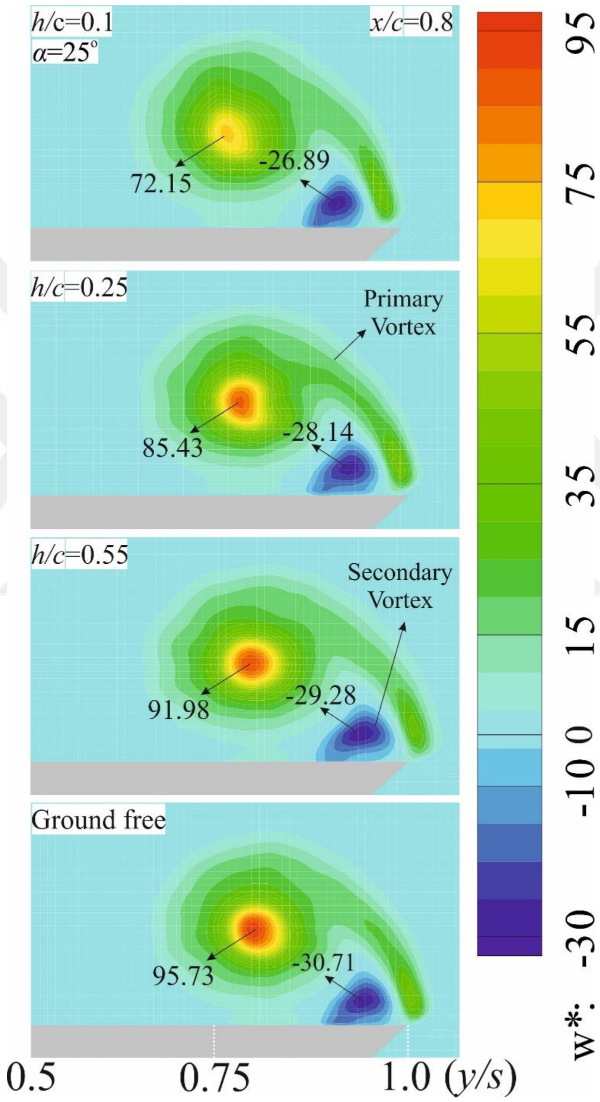

Figure 4.6. The time-averaged dimensionless primary and secondary vorticity, w^* concentrations in the end-view plane under the ground effect for h/c=0.1, 0.25 0.55, and the ground-free effect case at α=25° and x/c=0.8

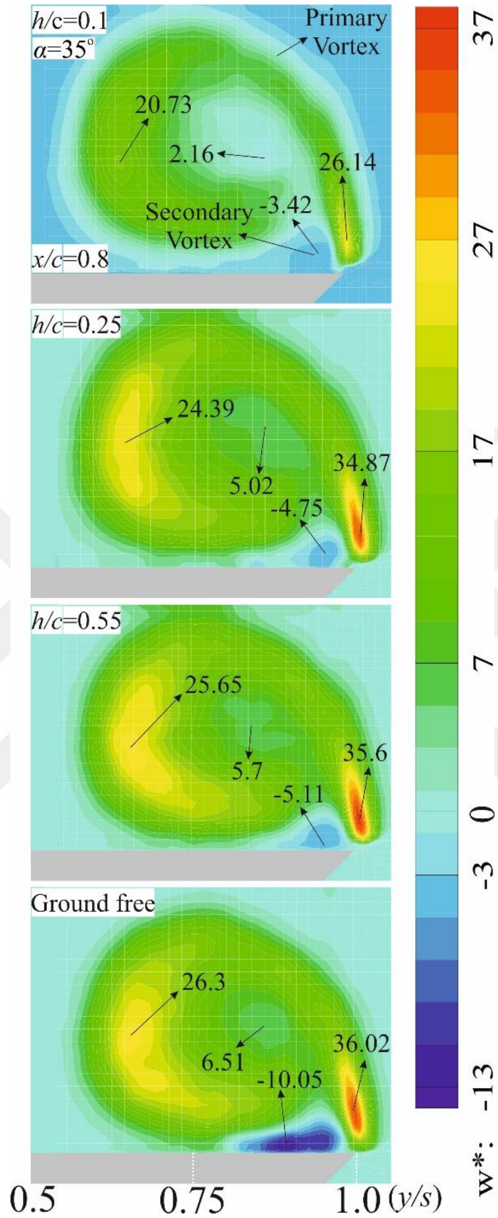

Figure 4.7. The time-averaged dimensionless primary and secondary vorticity, w^* concentrations in the end-view plane under the ground effect for h/c=0.1, 0.25 0.55, and the ground-free effect case at α=35° and x/c=0.8

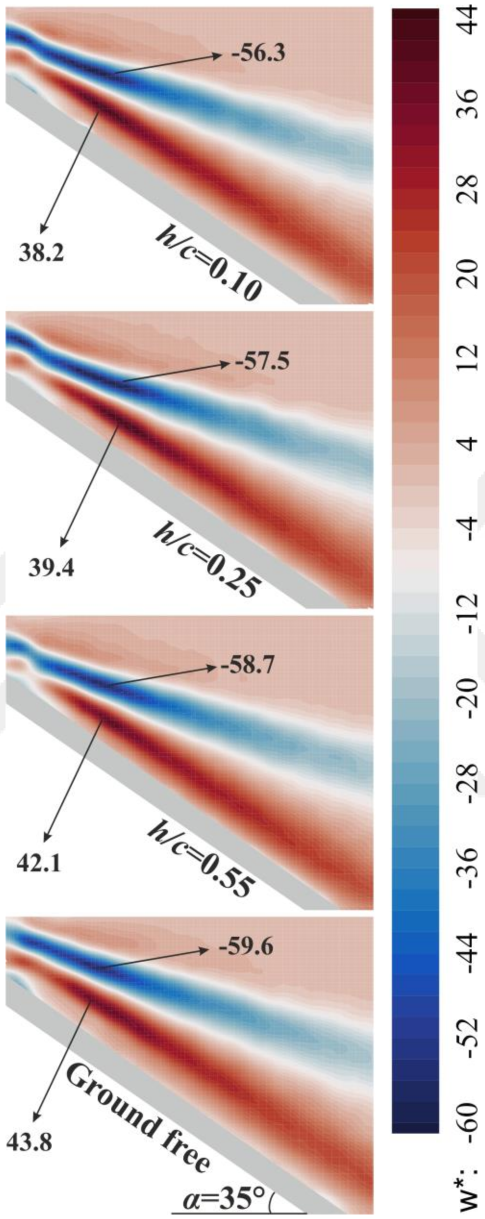

Figure 4.8. The time-averaged dimensionless vorticity, w^* concentrations in the side-view plane under the ground effect for h/c=0.1, 0.25 0.55, and the ground-free effect case at α=35°

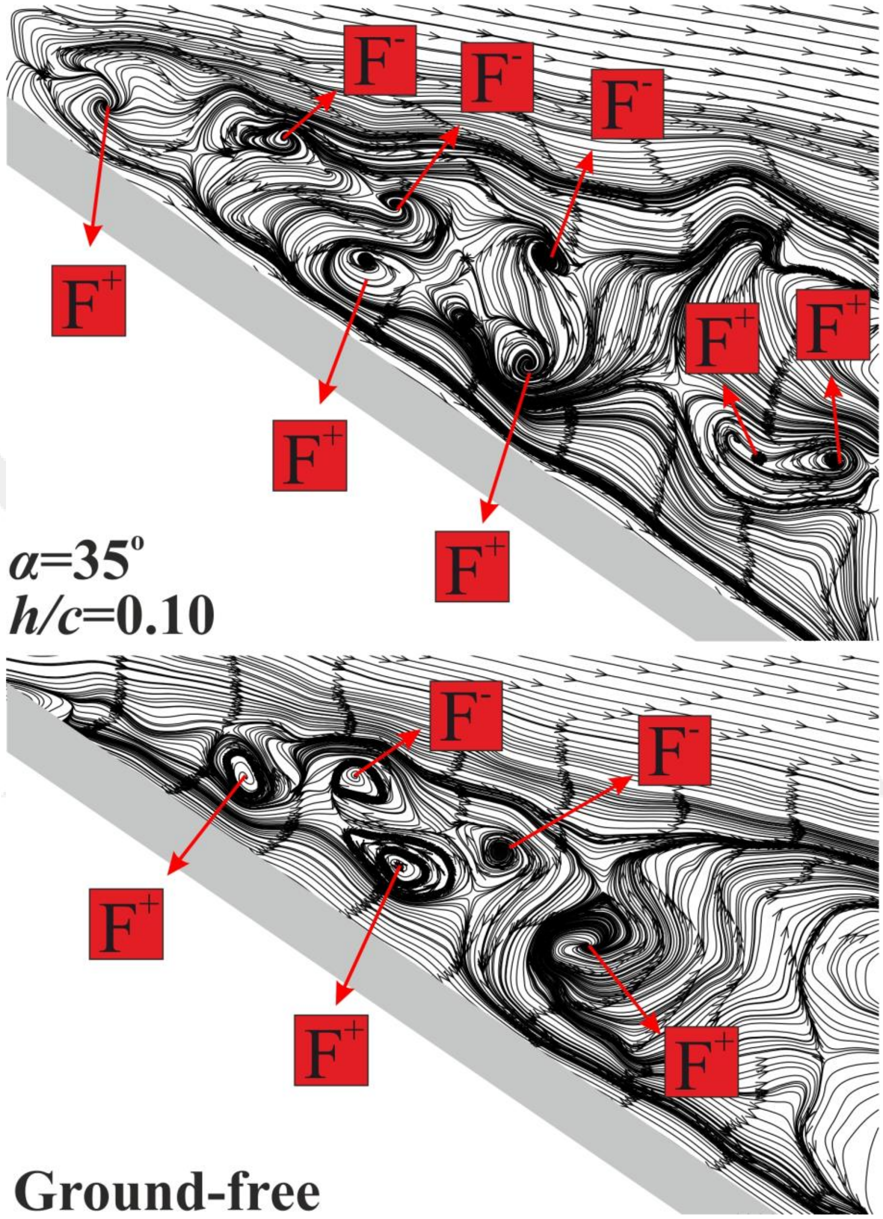

Figure 4.9. The variation of the instantaneous streamline patterns in the side-view plane under the ground effect for *h/c*=0.1, and the GFE case at *α*=35°

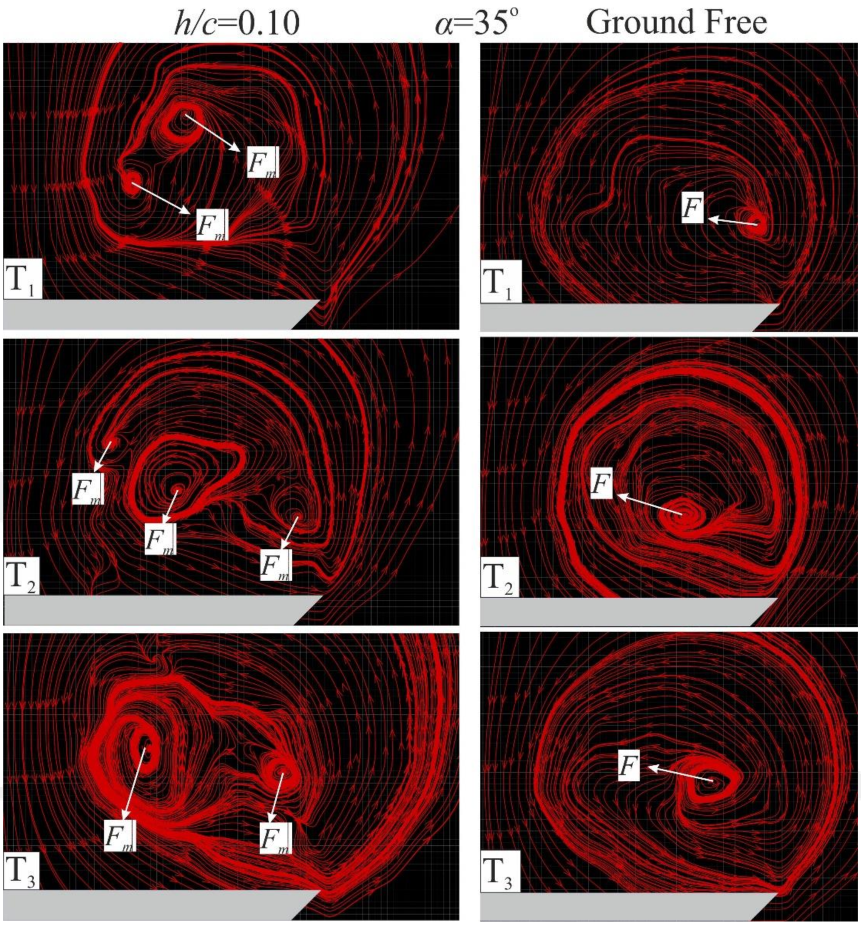

Figure 4.10. The instantaneous streamline patterns of the leading-edge vortices in the end-view plane under the ground effect for *h/c*=0.1 and the ground-free effect case at *α*=35° and *x/c*=0.8

In Figure 4.11, the instantaneous vorticity concentration was captured at three different times at *α*=35° and *x/c*=0.8 for both *h/c*=0.1 and GFE cases. The location of the VB was observed at the location before the test section, *x/c*=0.8 for all cases as specified in dye visualization results. It is revealed that the integrity of the vortex deteriorates as the delta wing moves from the unrestricted flow field into the GE field, and the LEV spreads over the wider region along the trailing edge of the slender wing compared to the GFE case. Furthermore, it was exposed that the concentration of LEVs attenuates with descent from the unrestricted flow field into the extreme GE field, *h/c*=0.1. Also, as seen from Figure 4.11, although the concentration of the secondary vortex decreased compared to the GFE case as a result of the GE, the secondary vortices were observed to be more widely distributed along the wing surface when the wing approaches the ground.

The influence of the ground on the contours of the time-averaged dimensionless turbulence kinetic energy is formulated in the equation as;

$$TKE = \frac{1}{2}\left(\frac{\sqrt{\overline{u'}^2 + \overline{v'}^2}}{U_\infty^2}\right)$$

for positions of delta wing as *h/c*=0.1, 0.25, 0.55 and GFE having an angle of attack of α=25° and 35° and cross-flow plane at *x/c*=0.8 is indicated in Figures 4.12-14. The transformation of flow energy into heat as a result of the work done by viscous stresses can be demonstrated by the change in turbulent kinetic energy dissipation, which is related to the extent of turbulence generation in shear flows, as stated in the study of Canpolat et al. (2012). The change of the large VB regions induced by the adverse pressure gradient along the chord of the suction side of the slender delta wing is related to the ground proximity. The flow separation expanding under the GE is related to the flow blockage caused by the reduction in the gap between the delta wing and the ground, as indicated by Qu et al. (2015). As a result of this flow phenomenon, the magnitude of the turbulent kinetic energy increases when the delta wing positions descend to the ground. Also, the area where the peak magnitude of the TKE spread widens as the delta wing moves from the unrestricted flow field into the GE field. For instance, the magnitude and the distribution of TKE at the wing's surface for extreme GE, *h/c*=0.1, is higher and compared to the GFE case. Furthermore, the region where the peak value of the TKE takes place on the wing's surface enlarges with decreasing *h/c*. Besides, it was observed that the peak magnitude of the LEV at α=25° and 35° increases both in the core region and in the region where the transition from the wing suction surface to the wing upper surface began. Likewise, while the delta wing approaches the ground, the increase in the peak TKE value before the VB locations can be seen in Figure 4.14. The image area was adjusted as one-third of the chord length for all cases. The region where the TKE value increased also represents both before *x/c*=0.8, which is the location of the experiments performed on the end-view plane, and the VB location region. And this region shows that it is coherent with both PIV experiments and Figure 4.12-13.

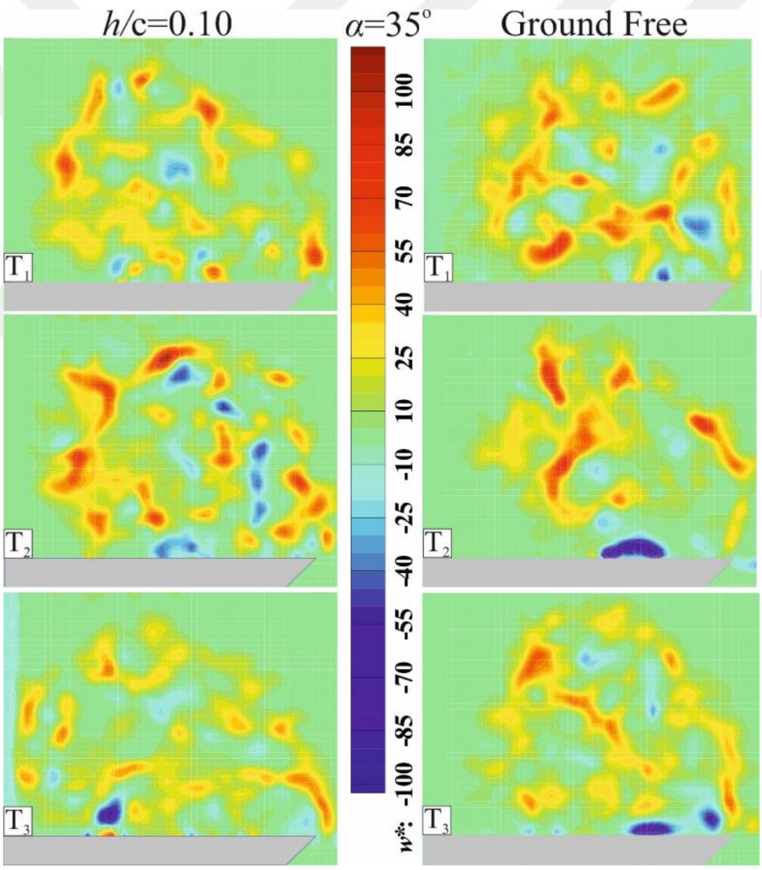

Figure 4.11. The instantaneous vorticity concentrations of the leading-edge vortices in the end-view plane under the ground effect for *h/c*=0.1 and the ground-free effect case at *α*=35° and *x/c*=0.8

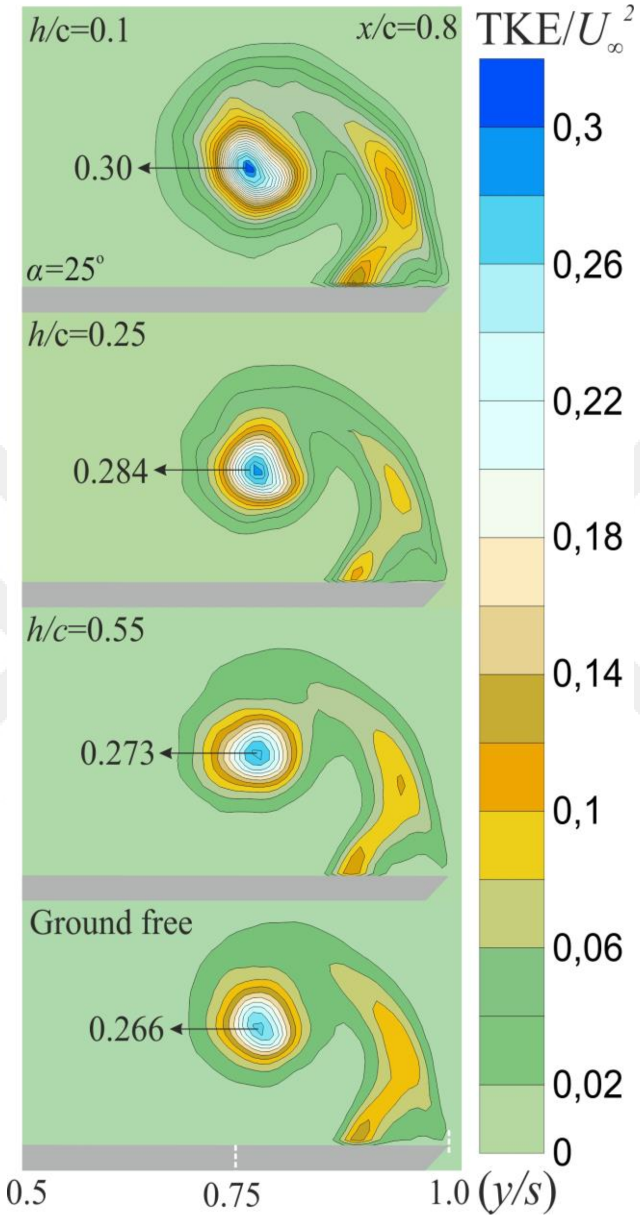

Figure 4.12. The variation of the time-averaged turbulence kinetic energy, TKE in the end-view plane under the ground effect for *h/c*=0.1, 0.25, 0.55, and the ground-free effect case at *α*=35° and *x/c*=0.8

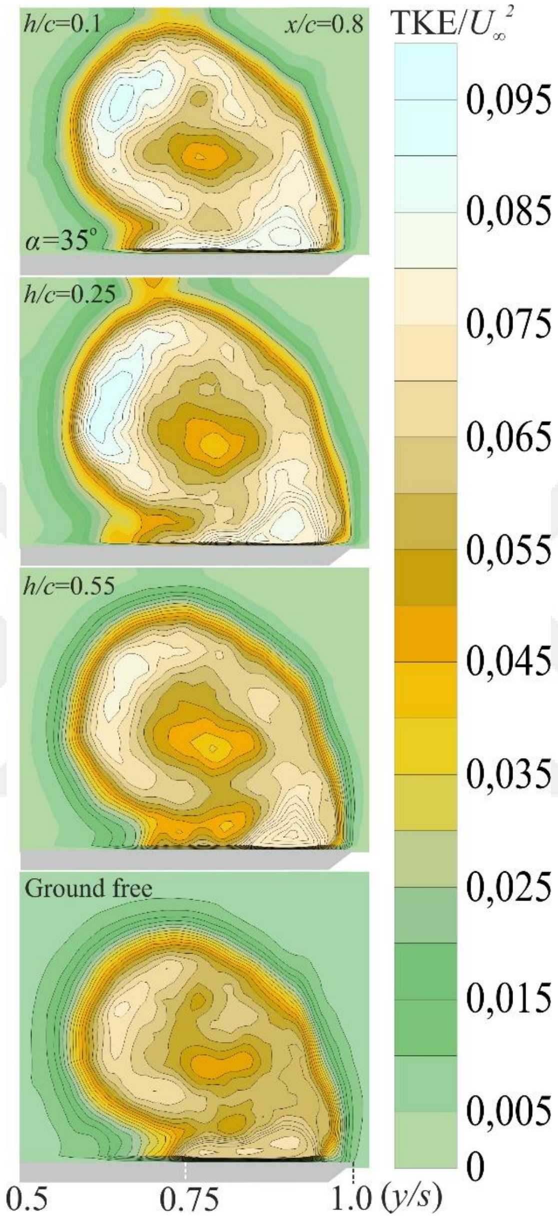

Figure 4.13. The variation of the time-averaged turbulence kinetic energy, TKE in the end-view plane under the ground effect for *h/c*=0.1, 0.25, 0.55, and the ground-free effect case at α=35° and *x/c*=0.8

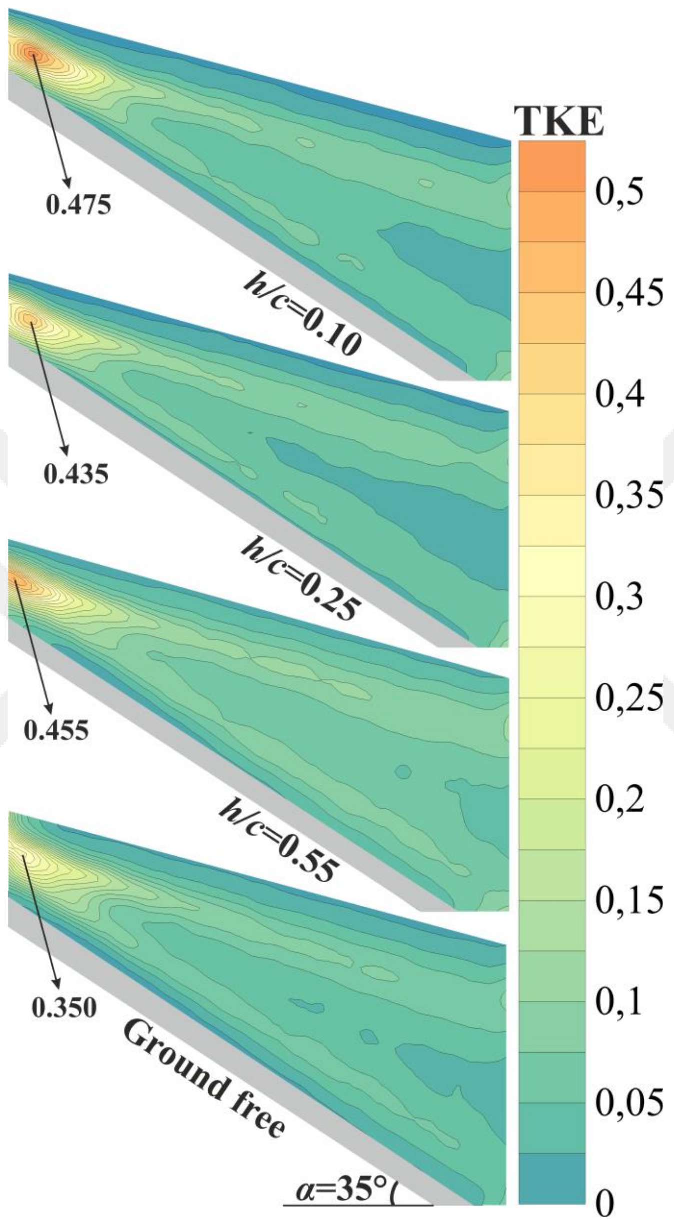

Figure 4.14. The variation of the time-averaged turbulence kinetic energy, TKE in the end-view plane under the ground effect for *h/c*=0.1, 0.25, 0.55, and the ground-free effect case at α=35°

The GE on the power spectral density (PSD) of the velocity component of *w* in end-view and side-view planes at α=35° is demonstrated in Figures 4.15-18 and 4.19-22, respectively. As seen in end-view figures of PSD (Figures 4.15-18), it is hard to acquire predominant peak frequencies over the slender wing under extreme GE, *h/c*=0.1 and 0.25, although the predominant peak frequencies are observed over the slender wing for GFE and *h/c*=0.55. A PSD distribution with lower magnitudes of the local peaks spread over the wing surface is observed with the decrement of *h/c*. This condition can be dependent on the complicated and disorganized flow structures caused by the GE-induced premature VB. The complex flow structure and the immature LEVs caused by the GE were also stated by Ozden et al. (2020). Moreover, it has been observed that the frequency decreases in the region where the fluctuations (RMS) increase. The magnitude of peak frequencies gets lower when the ground distance lowers from *h/c*=0.55 to 0.25 and 0.10. The peak frequencies decrease with increasing the GE because of the enlargement of the LEV due to the premature VB, as demonstrated by the patterns of streamlines and dye visualization images. Figures in the side-view plane (Figures 4.19-22) indicate that the scattered structure of the local frequencies was observed as a result of GE induced premature VB, causing a sophisticated flow structure over the slender delta wing for all cases, although the peak frequencies are predominant for GFE case and *h/c*=0.55 at points of a, b and c. In figures of PSD in the side-view plane (Figures 4.19-22), a PSD distribution with lower magnitudes of the local peaks spread over the wing surface is observed at points *d* and *e* due to strong interaction between the wing surface and the LEV compared to other locations *a*, *b,* and *c,* which are away from the wing surface. This situation can be interpreted as the unsteady and sophisticated flow structure resulting from fluid-structure interaction. When the ground proximity increases, only multiple peaks over the delta wing are distributed instead of one predominant peak in all cases measured. The large-scaled vorticity concentrations took place further downstream of the breakdown location of the LEVs. These large-scaled vorticity concentrations are separated into smaller swirls by striking each other. And, it is difficult to observe a predominant peak at PSD distribution when the interaction near the delta wing surface increase.

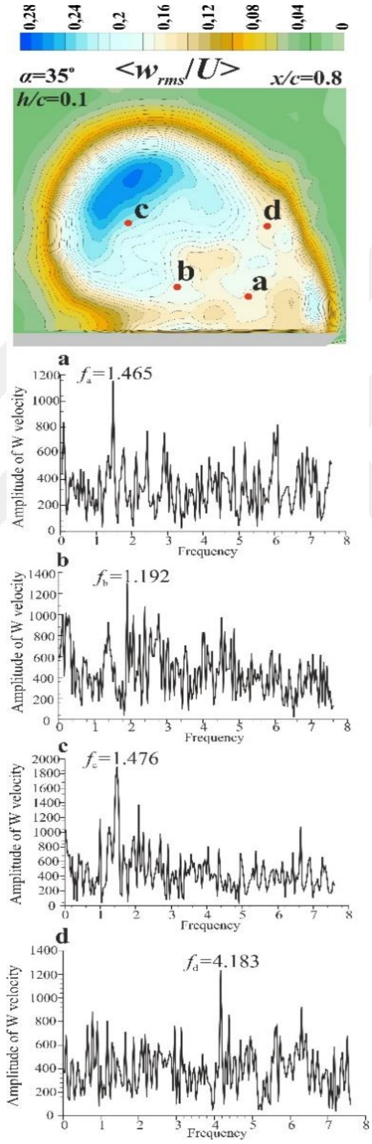

Figure 4.15. The power spectral density (PSD) of velocity component in the vertical direction, w_{rms} in the end-view plane under the ground effect for h/c=0.1 at α=35° and x/c=0.8

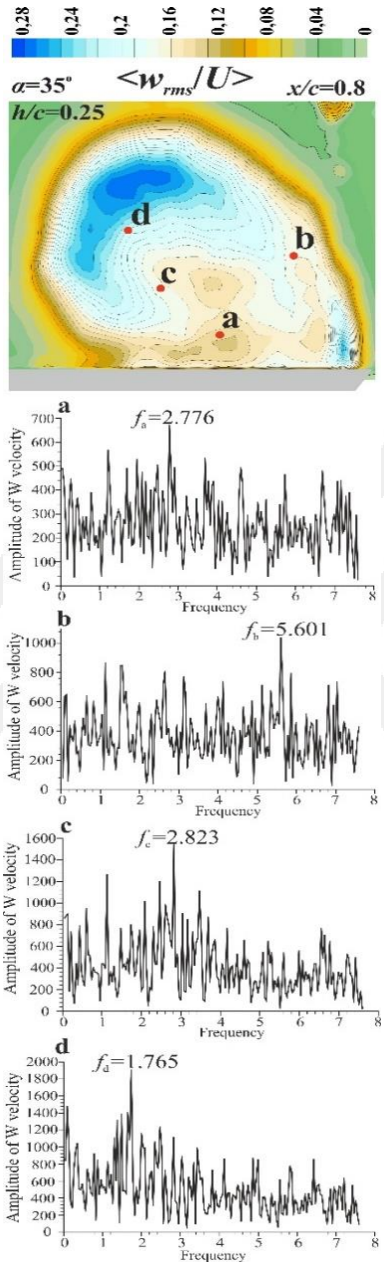

Figure 4.16. The power spectral density (PSD) of velocity component in the vertical direction, w_{rms} in the end-view plane under the ground effect for *h/c*=0.25 at *α*=35° and *x/c*=0.8

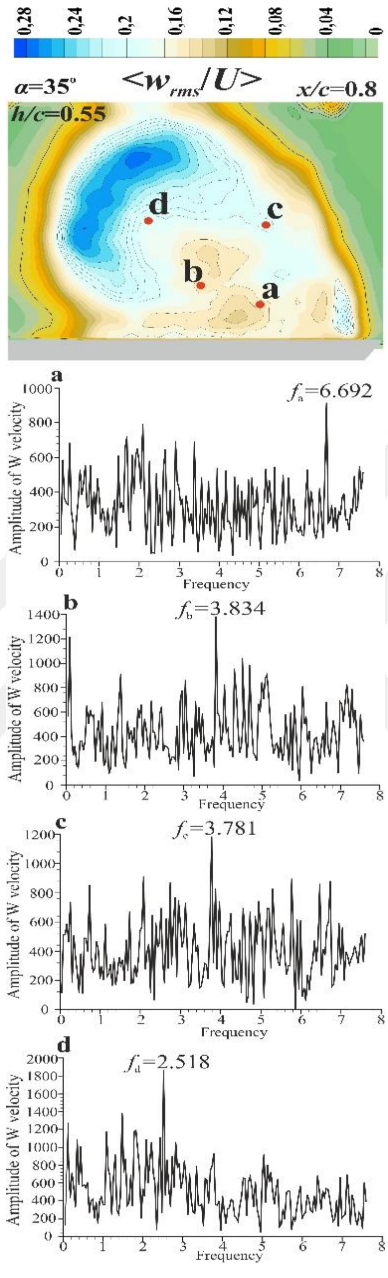

Figure 4.17. The power spectral density (PSD) of velocity component in the vertical direction, w_{rms} in the end-view plane under the ground effect for *h/c*=0.55 at *α*=35° and *x/c*=0.8

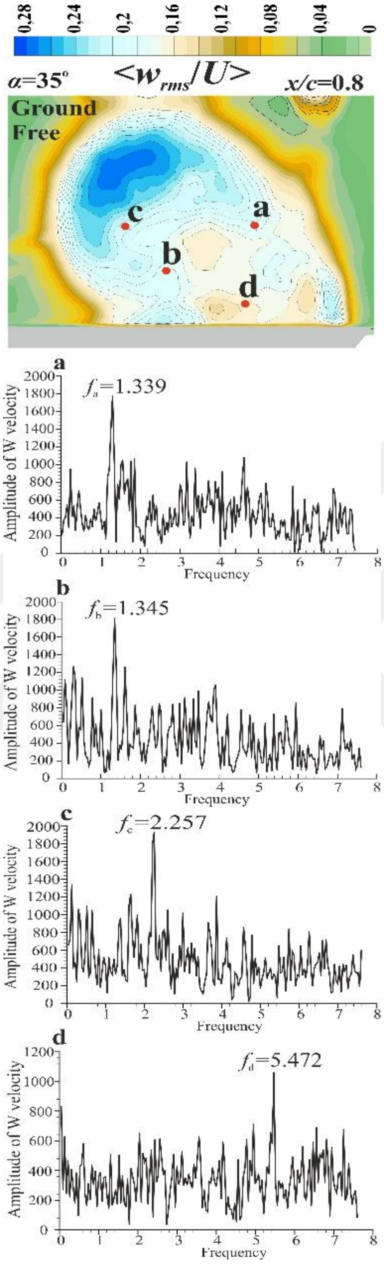

Figure 4.18. The power spectral density (PSD) of velocity component in the vertical direction, w_{rms} in the end-view plane under the ground effect for the ground-free effect case at α=35° and x/c=0.8

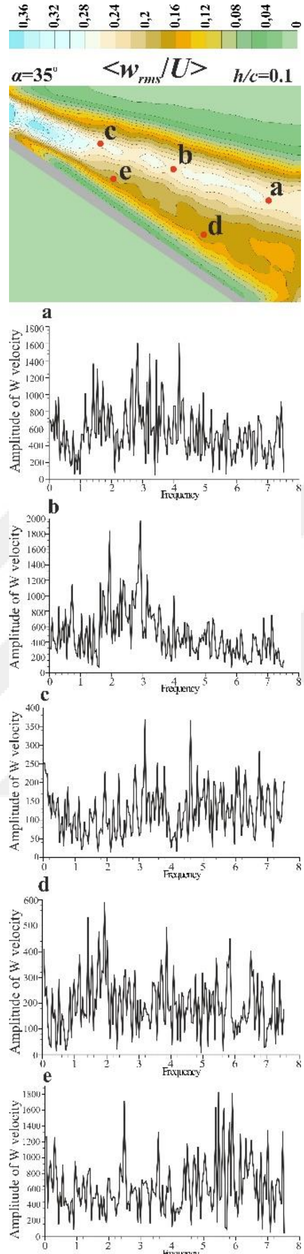

Figure 4.19. The ground effect on the power spectral density (PSD) velocity component in the vertical direction, v_{rms} in the side-view plane for h/c=0.1 at α=35° and x/c=0.8

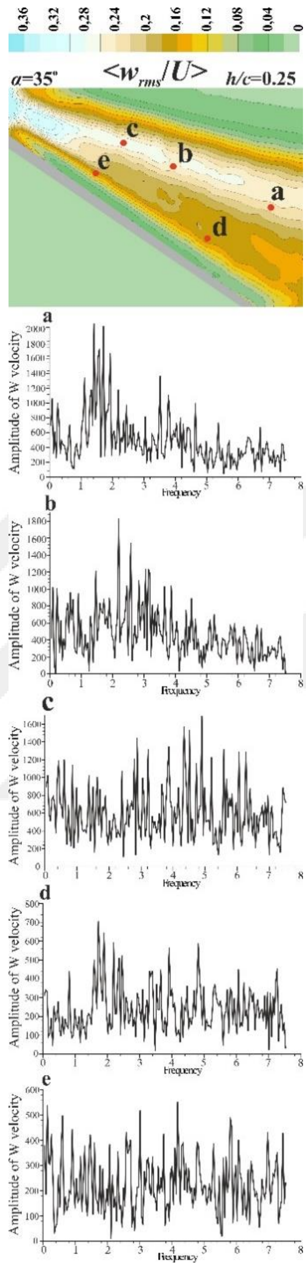

Figure 4.20. The ground effect on the power spectral density (PSD) velocity component in the vertical direction, v_{rms} in the side-view plane for h/c=0.25 at α=35° and x/c=0.8

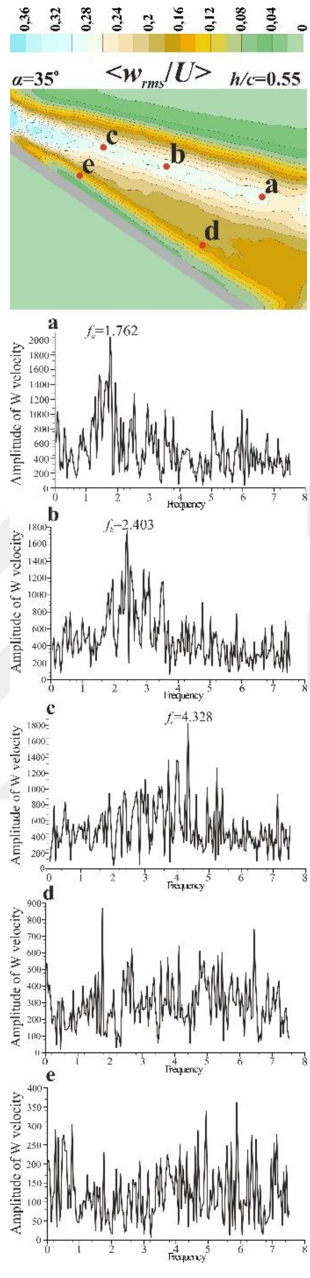

Figure 4.21. The ground effect on the power spectral density (PSD) velocity component in the vertical direction, v_{rms} in the side-view plane for h/c=0.55 at α=35° and x/c=0.8

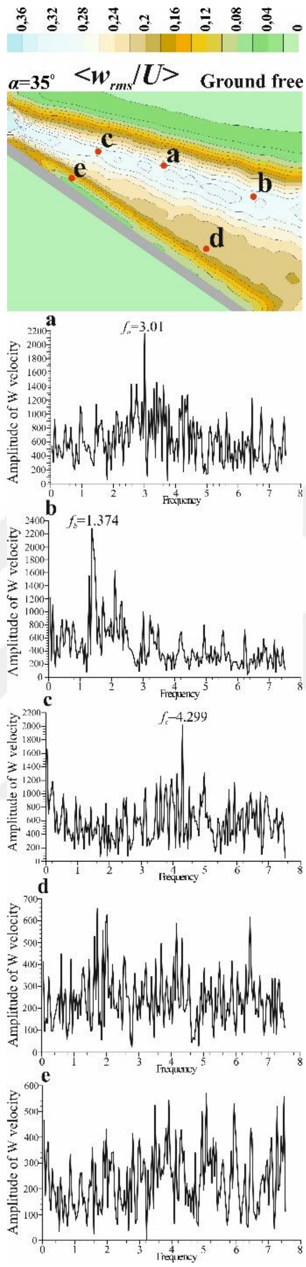

Figure 4.22. The ground effect on the power spectral density (PSD) velocity component in the vertical direction, v_{rms} in the side-view plane for the ground-free effect case at α=35° and x/c=0.8

A comparison of the lift coefficient, C_L of a non-slender delta wing with a sweep angle of Λ=40° at four different angles of attack of α=5°, 10°, 23°, and 30° reported by Tumse et al. (2021) is compared with the lift coefficient, C_L of the slender delta wing with Λ=70° conducted in the present work as demonstrated in Figure 4.23. There is a significant difference in C_L between these two delta wings at higher α. For instance, C_L was detected as 0.642 for the non-slender wing, while C_L was measured as 1.208 for the slender wing at α=23° and GFE case. However, the lift coefficient C_L variation under the ground effect is more significant for the non-slender delta wing than the slender delta wing in all cases due to the effectiveness of the sweep angle, Λ. In the case of the larger wing surface area with a low sweep angle, the interaction between the pressure side of the wing and the ground is higher than the slender wing. Also, the large surface of the non-slender wing area forces the incoming flow rate to swirl towards the suction side of the wing with a large amount compared to the slender delta wing. This situation causes the lift enhancement to be more remarkable for non-slender wings. For instance, the increase in C_L for the non-slender wing was 30.3%, while the increase in C_L was only 8.5% for the slender wing at α=5° when the wing descends from the GFE field to the extreme GE at *h/c*=0.1. On the other hand, the increase in C_L for the non-slender wing was 37.5%, while the increase in C_L was 19.8% for the slender wing at α=30° when the wing lowers from the unrestricted flow field to the GE at *h/c*=0.1. It can be said that the non-slender wings are more sensitive to all α's compared to the slender delta wing. As a result of the examination of non-slender and slender wings, it has been revealed that the flow physics under the GE have substantially different characteristics for each wing. The comparison of lift-to-drag ratio, C_l/C_D between the present study of a slender delta wing with a sweep angle of Λ=70°, which is also coherent with the studies of Lee and Ho (1990), Wentz and Kohlman (1970), and Karasu et al. (2021), and non-slender delta wing with sweep angle Λ=40° reported by Tumse et al. (2021) is also indicated in Figure 4.24-25. As a general trendline for slender delta wings, the values of C_l/C_D were found to be larger than non-slender delta wings. Although the ratio of C_L/C_D for the slender delta wing is greater in the region where the ground effect is not felt or felt less compared to extreme GE, *h/c*=0.1, the ratio of C_L/C_D for the non-slender delta wing is higher under all GE cases compared to GFE case. It can be concluded that the aerodynamic efficiency of the non-slender delta wings, C_L/C_D is higher under the GE compared to slender delta wings.

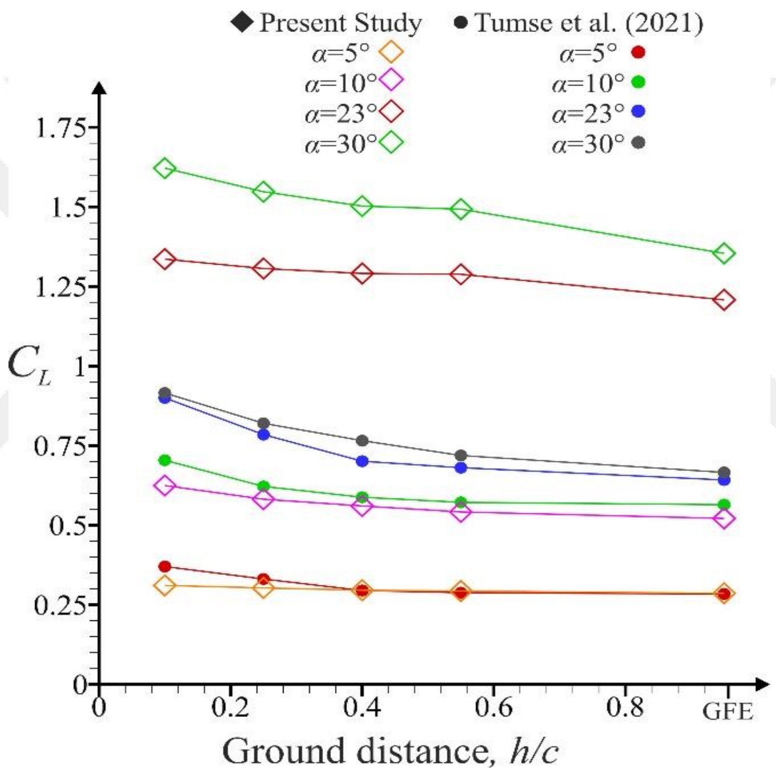

Figure 4.23. The comparison of C_L between the present study of a slender delta wing with a sweep angle of Λ=70° and a non-slender delta wing with a sweep angle of Λ=40° was reported by Tumse et al. (2021)

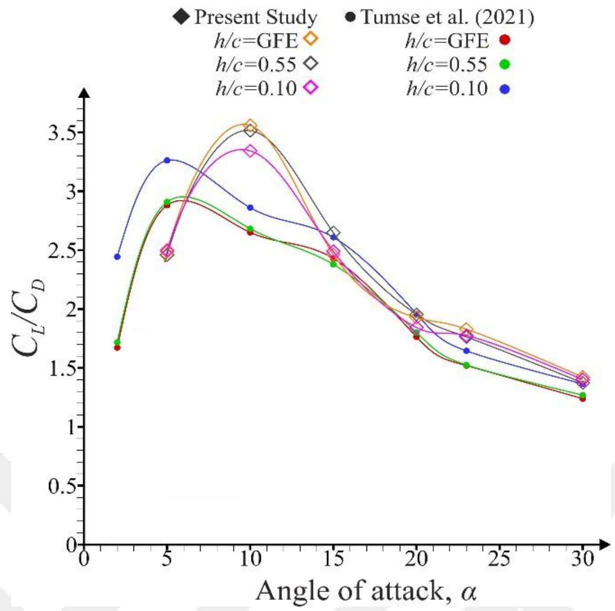

Figure 4.24. The comparison of C_L/C_D between the present study of a slender delta wing with a sweep angle of Λ=70° and a non-slender delta wing with a sweep angle of Λ=40° was reported by Tumse et al. (2021)

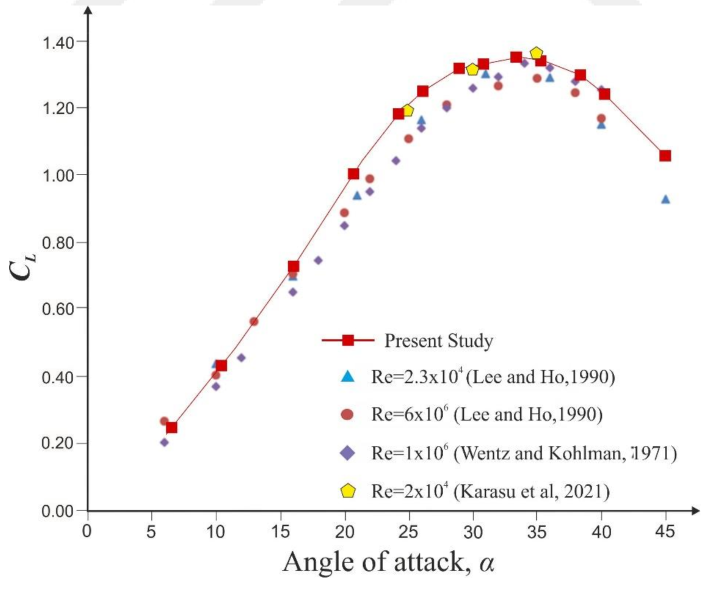

Figure 4.25. The comparison of C_L between the present study and similar studies in the literature

In Figures 4.26-4.28, the GE on the aerodynamic behaviors of the 70-deg-swept slender wing was experimentally conducted for *h/c*=0.1, 0.25 0.55, and GFE cases within the range of angles of attack 5°<α<45°. It is revealed in Figure 4.25 that the current results of lift coefficient, C_L having zero yaw angle, β under the GFE case have good agreement with Tasci et al. (2020) and Karasu et al. (2021), who conducted the measurement of the aerodynamic features on the 70-deg-swept delta wing. Figure 4.26 demonstrates the variations of the lift coefficients, $C_{L,}$ with changing the ground distance, *h*. When the angle of attack α exceeds 20°, the change in values of C_L begins to be seen clearly as a result of the GE. As the delta wing approaches the stall flow region at α=33°, C_L dramatically increases when the ground proximity increases, *h/c*. For instance, the percentage of increase in lift coefficient, ΔC_L between GFE case and extreme ground case, *h/c*=0.1, is 8.4%, 14.3%, 15.5% when the angle of attack, α is set as α=20°, 28°, and 33°, respectively. The C_L values decrease less than the GFE case in the post-stall field as the delta wing moves from the ground free flow field into the ground affected flow field. For example, the percentage of increases in C_L is 15.1% and 14%, at *h/c*=0.1, which is higher than the increase in C_L at α=38°, and 45° in the GFE case. It is evaluated that the increase in C_L induced by the GE is related to the rise in the ram pressure with increasing the ground proximity. Moreover, the aerodynamic features are positively affected by the ground proximity as a result of the dynamic air cushion effect, which is the increase in the pressure on the suction side in the chord direction of the slender delta wing due to the stagnation of air in the gap between the slender delta wing and the ground surface. The dynamic air cushion effect deteriorates by decreasing ground proximity due to lowering the ram pressure effect.

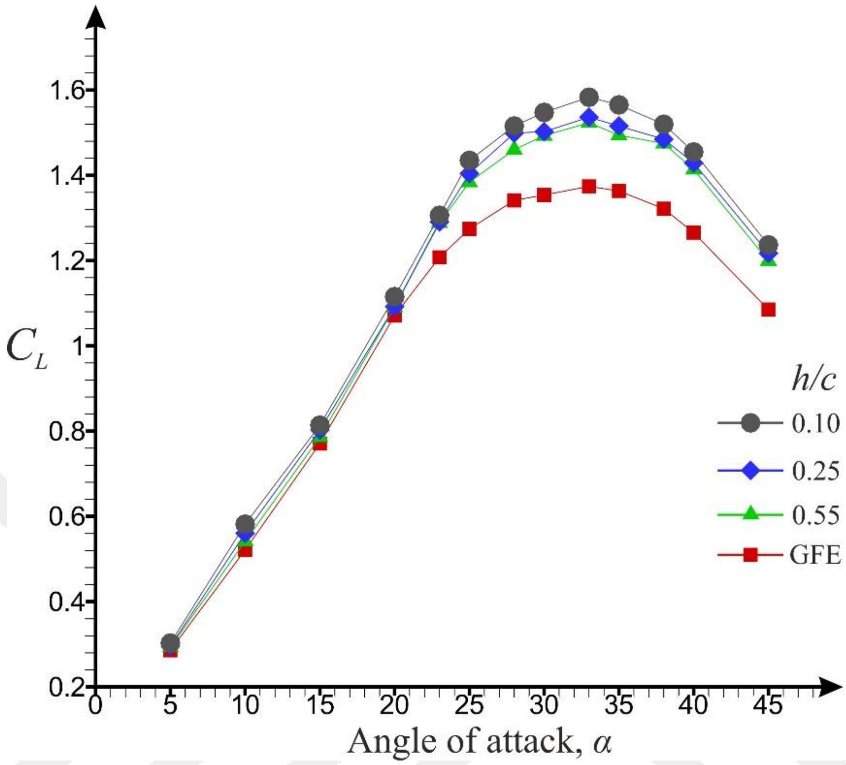

Figure 4.26. The variation of the lift coefficients, C_L of the slender wing under the ground effect within the range of angles of attack 5°<α<45° for h/c=0.1, 0.25 0.55, and the ground-free effect case

In Figure 4.27, it is seen that the augmentation of the GE also causes a persistently higher drag coefficient, C_D regardless of α for all ground distances considered. The lower h/c adjusted; the higher the drag coefficient, C_D occurred. The increase in the measured C_D may be induced by the ram pressure over the suction side of the delta wing as well as the pressure drag generated by the earlier breakdown of the LEVs. As seen in the change of C_L, there is a significant change in C_D having the angle of attack beyond α=20°. The C_D at h/c=0.10 is always higher compared to the GFE case. For instance, the percentage of an increase in the drag coefficient, ΔC_D between the unrestricted flow field and the extreme GE, h/c=0.1 is 15.4% when the angle of attack is set as α=25°.

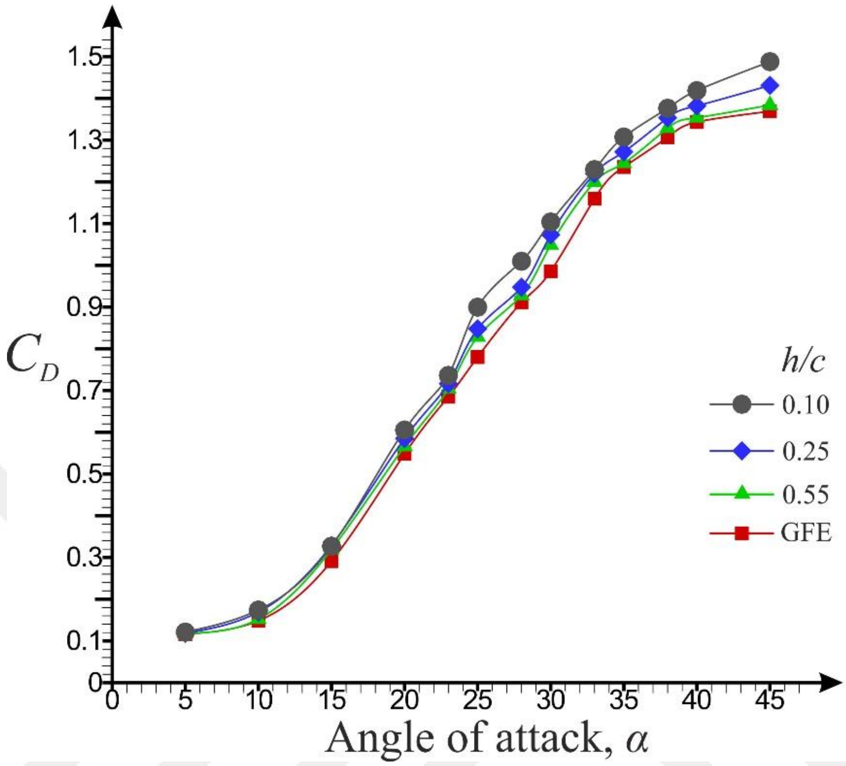

Figure 4.27. The variation of the drag coefficients, C_D of the slender wing under the ground effect within the range of angles of attack 5°<α<45° for *h/c*=0.1, 0.25 0.55, and the ground-free effect case

In Figure 4.28, it is seen that the augmentation of the drag coefficient, C_D, is overwhelmingly higher than the augmentation of the lift coefficient, $C_{L,}$ for higher α's. In other words, the increment in C_D is suppressed by the increment in C_L at lower α. This situation causes the existence of a higher lift-to-drag ratio, $C_L/C_{D,}$ which recommends that the delta wing in-ground to fly in high ground proximity has higher performance at lower α as also defined by Lee and Ko (2018).

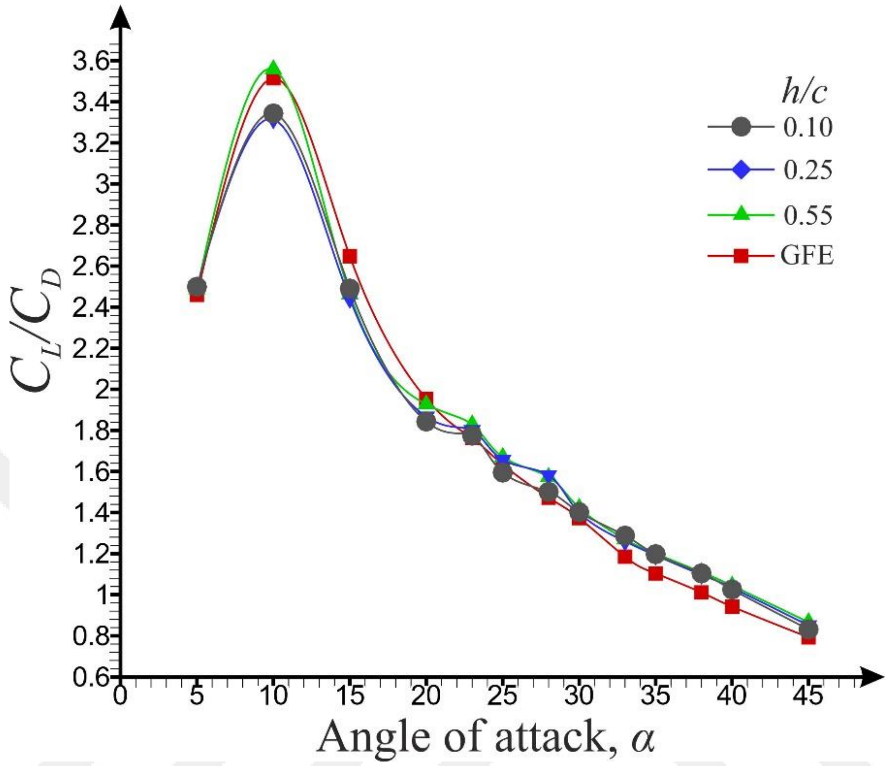

Figure 4.28. The variation of the lift-to-drag ratio, C_L/C_D for the slender wing under the ground effect within the range of angles of attack 5°<α<45° for *h/c*=0.1, 0.25 0.55 and the ground-free effect case

The total circulation of leading-edge vortices, Γ_o was computed with the Stokes theorem which is shown in the equation as;

$$\Gamma_o = \oint_C \vec{u}\,.\,d\vec{x} = \int_A [\nabla \times \vec{u}].\hat{n}dA = \int_A \vec{\omega}.\hat{n}dA$$

In the equation, Γ_o denotes the strength of total circulation of leading-edge vortices around a closed curve, *C*, $\vec{u}$ is the randomly directed velocity vector, and the projection of $\vec{u}$ in the direction of $d\vec{x}$ can be acquired by obtaining the scalar product between two vectors. Moreover, $\vec{\omega}$ is the vorticity vector, A is the area confined by the vorticity contour. The magnitude of total circulation, Γ_o is nondimensionalized by the multiplication of the length of the wing chord, *c*, and the freestream flow velocity, U_∞ as $\Gamma_o/U_\infty c$.

The GE on the total circulation, $\Gamma_o/U_\infty c$ of the LEVs for *h/c*=0.1, 0.25, 0.55, and GFE at *α*=35° and *x/c*=0.8, is indicated in Figure 4.29. The change in $\Gamma_o/U_\infty c$ of the LEVs is related to the aerodynamic characteristics of the wing. As seen from Figure 4.29, the total circulation $\Gamma_o/U_\infty c$ of the LEVs augments when *α* dramatically increases from 25° to 35°, which is coherent with the high C_L at high *α*'s. For instance, the total circulation gets higher from the value of $\Gamma_0/U_\infty c$=0.322 to 0.517 when the angle of attack alters from *α*=25° to 35°. An increase in $\Gamma_o/U_\infty c$ with GE is also compatible with the enhancement of the C_L. The total circulation, $\Gamma_o/U_\infty c$, gradually increases when the wing approaches the ground as a result of the effect of the ram pressure, as stated by Gursul and Wang (2018). When the wing lowers to the ground, the dynamic air cushion increases, and this causes an increase in the total circulation value. For instance, the overall increase in $\Gamma_0/U_\infty c$ is 27.5% when the ground distance is altered from the GFE case to *h/c*=0.1 at *α*=35°.

In Figure 4.30, the GE on the magnitude of dimensionless time-averaged velocity vectors, $\langle V\rangle/U_\infty$ for three different locations along the end-view plane at *α*=35° and *x/c*=0.8 under the variations of the ground distance as *h/c*=0.1, 0.25 0.55 and GFE case was demonstrated. The measured locations were selected regarding the important locations on the time-averaged streamline patterns for the slender wing. For example, line *2* is the center of LEV, and it is also called the focal point, *F*. Furthermore, the lines with numbers *1* and *3* are selected to be able to observe the change of time-averaged velocity vectors on the close region to the wing surface and away from the wing surface with GE, respectively. The value of $\langle V\rangle/U_\infty$ is higher in the region towards the wing's center compared to the leading edge of the wing for all measured locations on the wing. Also, it was seen that the magnitude of $\langle V\rangle/U_\infty$ decreases in the region far from the wing surface, Line *3*, compared to Lines *1* and *2*. As seen in Figure 4.30, the magnitude of $\langle V\rangle/U_\infty$ is observed to get higher in most of the flow fields, especially in the vicinity of the wing's leading edge for all selected locations of *1, 2,* and *3*. The effect of the ram pressure, which is induced by the air cushion between the pressure surface of the wing and the ground, gives rise to a slow down of fluid flow near the wing's central axis and causes the flow to move from the wing's central axis to leading edge of the wing along the spanwise. Therefore, the flow velocity increases towards the leading edge of the wing as a result of the effect of the ram pressure. Furthermore, the GE induces the magnitude of $\langle V \rangle / U_\infty$ to increase in most of the field, especially near the wing's leading-edge for lines *1* and *3* compared to the GFE case.

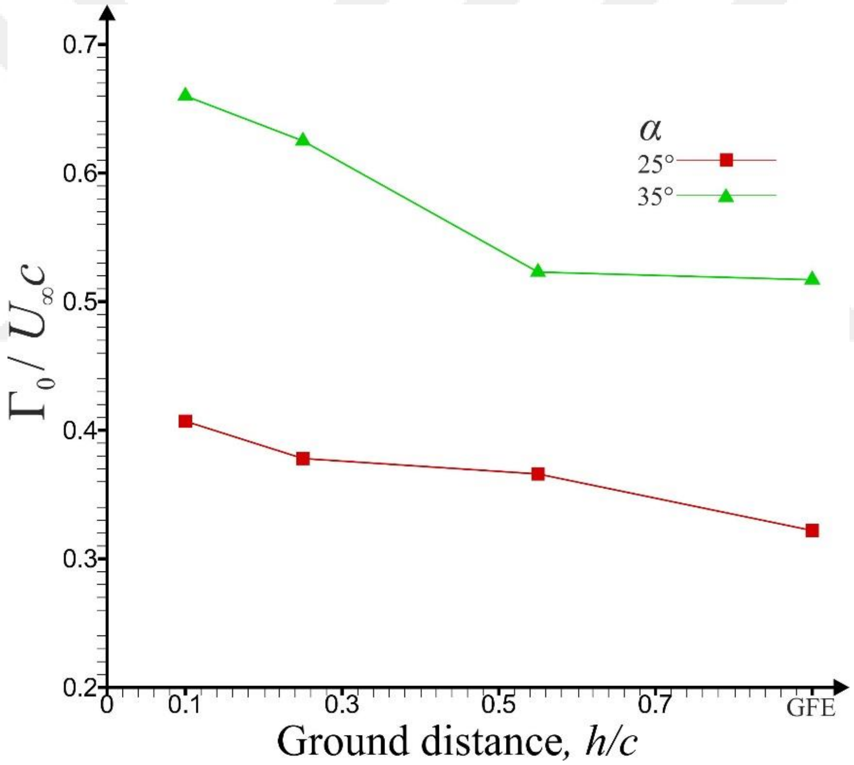

Figure 4.29. The ground effect on the total circulation, Γ_0 for *h/c*=0.1, 0.25, 0.55, and the ground-free effect case at α=35° and *x/c*=0.8

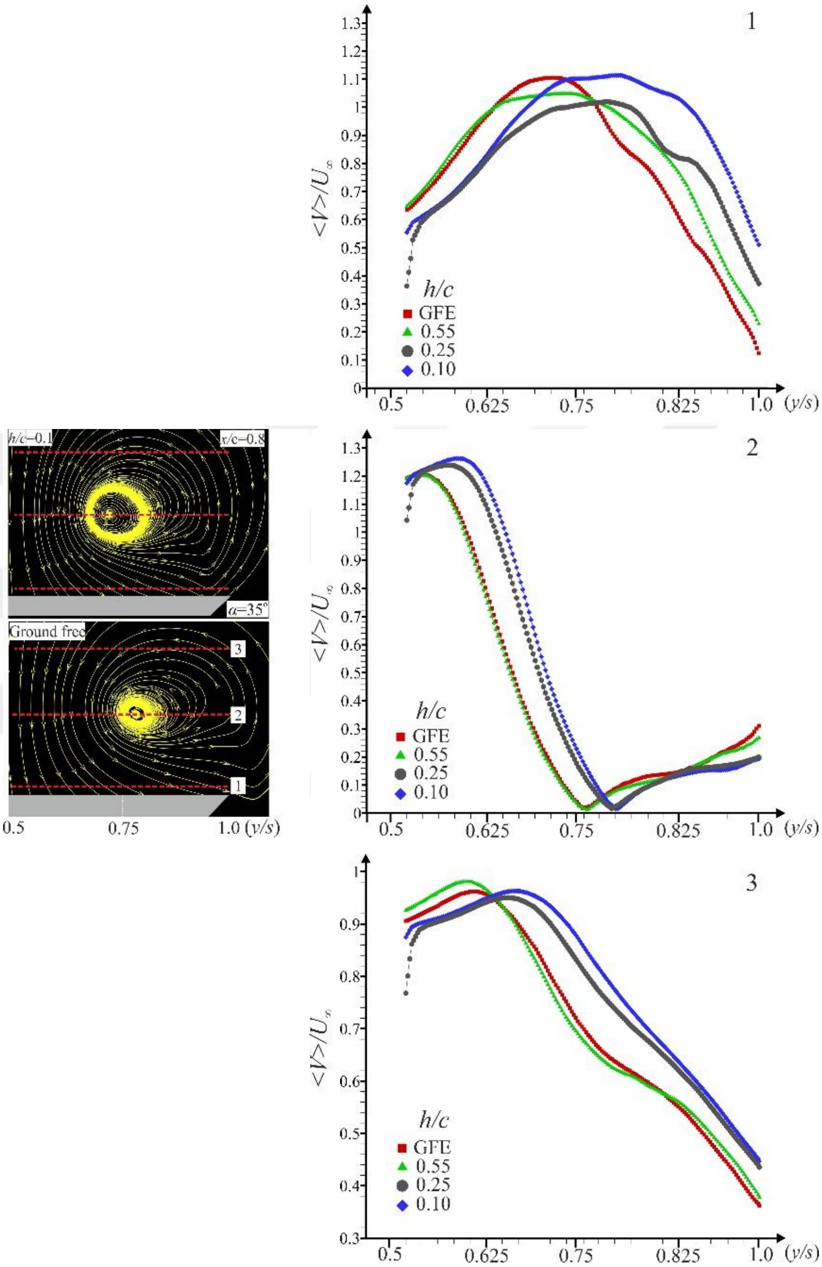

Figure 4.30. The ground effect on the magnitude of dimensionless time-averaged velocity vectors, $<V>/U_\infty$ for three different locations along the end-view plane for *h/c*=0.1, 0.25, 0.55, and the ground-free effect case at α=35° and *x/c*=0.8

4.2. The Ground Effect on the Double Delta Wing

The identification of the strake, the wing, and the secondary vortices over the double delta wing surface at α=10° in the case of the GFC was qualitatively displayed in Figure 4.31. As a flow characteristic of double delta wings, the low and mean angles of attack, *α,* are more suitable for the vortex definitions. Since high angles of attack, *α,* cause the flow to stall over the double delta wing, it is not possible to identify the vortices separately, and it is seen that the vortices begin to turn into a large vortex form, which is called "coiled-up vortex". The slender part of double delta wings is sensitive as a function of high angles of attack, *α,* in the formation of the VB that occurs over the wing. On the other hand, the non-slender part of the double delta wing is even delicate to the low *α* in the formation of the VB, which reveals the flow physics over the wing in detail. Because of the impact of the sweep angle, *Λ* on the formations of the vortical flow over the double delta wing, all types of vortices on the double delta wing are visible at a mean *α* as seen in Figure 4.31. The effect of the slender part of the double delta wing causes the formation of the strake vortex. On the other hand, the wing vortex is formed as a result of the non-slender part of the double delta wing and the interaction of the flows formed in the slender and non-slender parts of it.

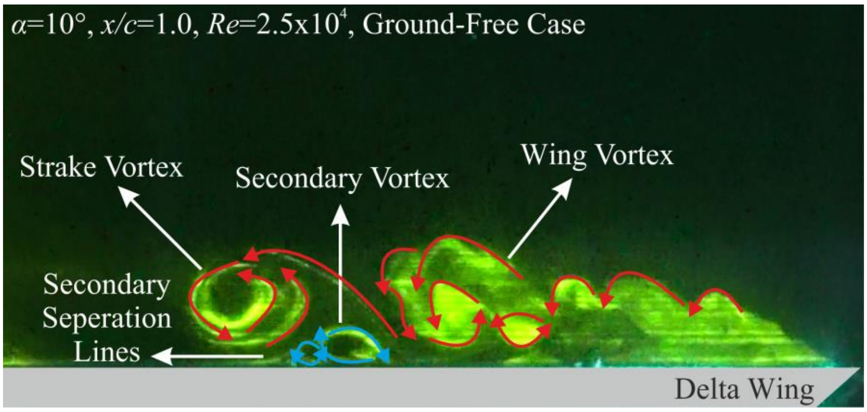

Figure 4.31. The identification of the strake, wing, and secondary vortices over the double delta wing at α=10°

The GE on the alteration of the location of the VB over the double delta wing at α=25° under the variations of *h/c* was qualitatively indicated in Figure 4.32. As shown in Figure 4.32, the location of earlier VB of the coiled-up vortex was noticed over the wing surface under the GE in comparison with the GFC at α=25°. For example, while the VB locations were detected as *x/c*=0.64 and 0.68 for *h/c*=0.55 and GFC, respectively, however, the location of the VB moves towards to apex of the double delta wing, and it is observed at *x/c*=0.59 for *h/c*=0.10. The GE causes the coiled-up vortex to induce an earlier VB because of growth in the gradient of the adverse pressure on the bottom of the double delta wing through the chordwise direction. As seen in Figure 4.32, the amplitude of the fluctuations in the VB location increases as the double delta wing moves towards the ground surface because of the disorganized and irregular flow structures. In the GFC, the amplitude of the fluctuations in the VB location was found more stable compared to the case of *h/c*=0.10.

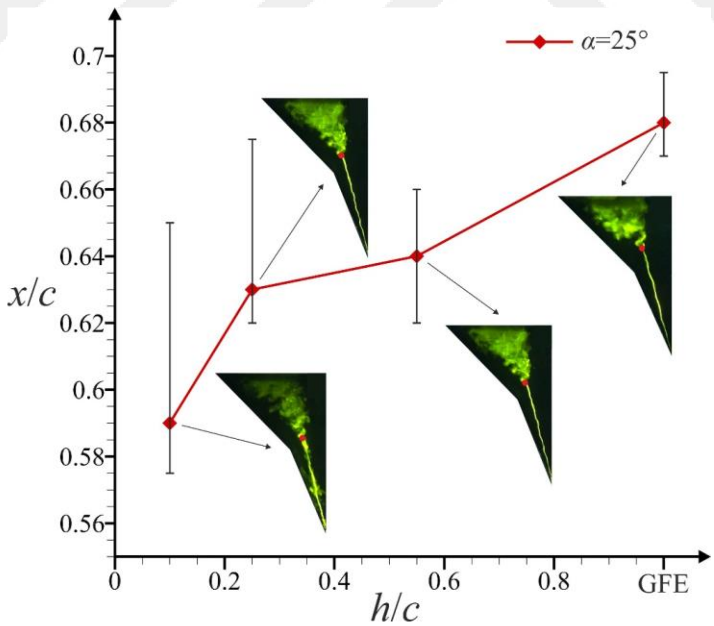

Figure 4.32. The formation of the VB over the double delta wing at α=25° under the variations of *h/c*

Figure 4.33 demonstrates the GE on the time-averaged streamline patterns at α=15° under the variations of h/c. Here, there are the definitions of F_s, F_w, z_s/s, z_w/s, y_v/s, and θ_{sw}. z_s/s and z_w/s, which are used to define the distance between the foci of the strake and wing vortices, F_s and $F_{w,}$ and the wing surface. On the other hand, y_v/s is the distance between the foci of the strake and wing vortices. The distances on the flow characteristics, z_s, z_w, and y_v, are normalized with the semi-span length, s. Finally, θ_{sw} is the rotational angle between the foci of the strake and wing vortices, as also indicated in the study of Zhang et al (2016). It is revealed that z_s/s decreases when the double delta wing descends from the GFC field to the ground region at h/c=0.10. It can be interpreted that the GE causes the intensity of the interaction between the vortical flow and the wing surface to increase with diminishing the ground distance. It is also coherent with the GE inducing the earlier VB. For example, z_s/s was detected as 0.181 at the extreme ground case, h/c=0.10, while the distance was equal to z_s/s=0.196 at the GFC. Although the interaction between the flow and the wing surface increases because of the GE, the impact of the dynamic air cushion, which is the increase in the gradient of the adverse pressure on the bottom of the double delta wing through the chordwise direction because of the air stagnation in the area between the ground and the double delta wing, causes the wing vortex to move away from the delta wing surface. As can be seen from Figure 4.33, the height of the wing vortex, z_w/s, increases as the double delta wing gets closer to the ground surface. For example, while z_w/s was observed as 0.139 in the case of GFC, it was observed that z_w/s is equal to 0.153 at h/c=0.10. Because of air cushioning, there is a decrease in the rotational angle, $\theta_{sw,}$ between the strake and wing vortices. For example, θ_{sw} was detected as 6.4° in the case of h/c=0.10, while θ_{sw} was 10.4° in the case of GFC. In addition, the distance between the strake vortex and wing vortices, y_v/s, also decreases as a result of earlier VB and the vortices converge with each other as revealed in the study of Zhang et al (2016). For example, while y_v/s is found to be equal to 0.338 in the case of GFC, this value decreases to 0.318 when the position of the double delta wing declines from the region of GFC close to the location of *h/c*=0.10.

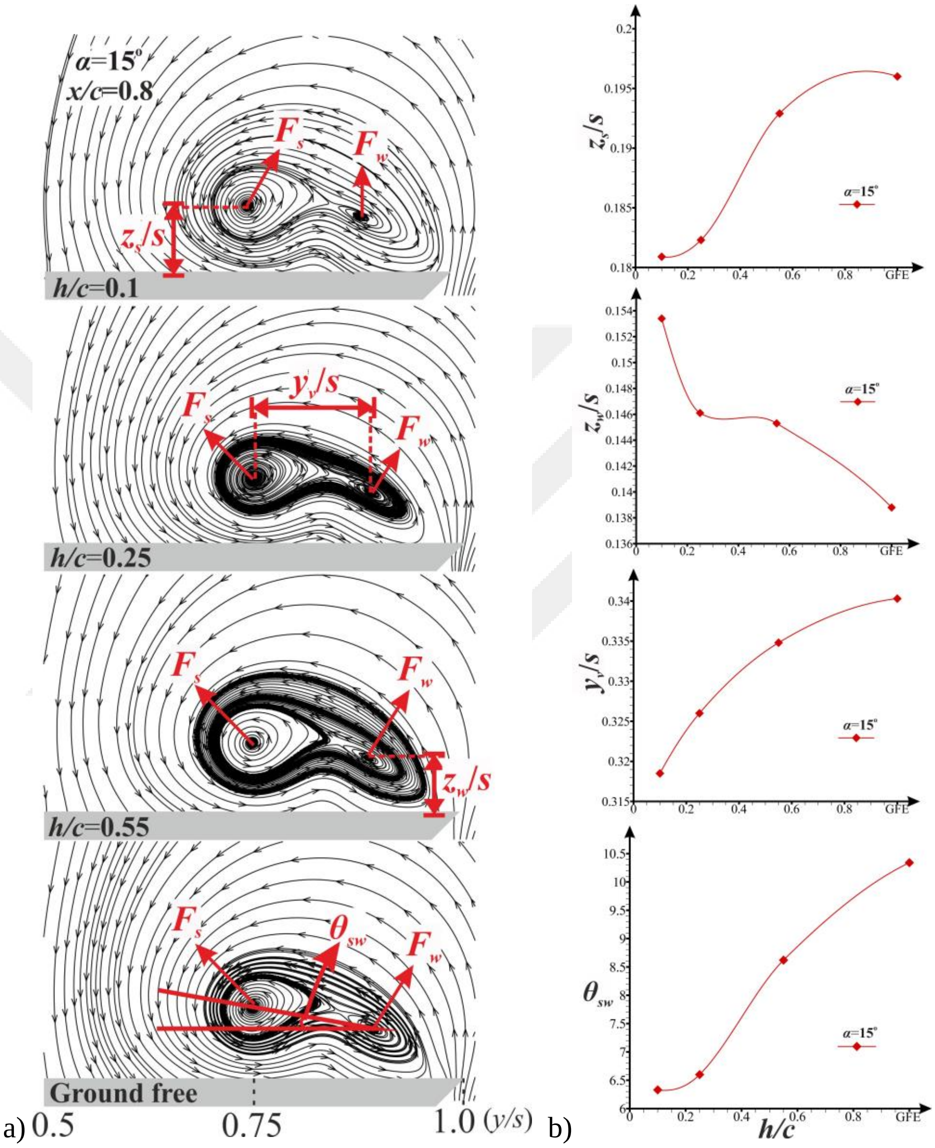

Figure 4.33. a) The patterns of the time-averaged streamline in the cross-flow plane at α=15° under the variations of *h/c*. b) The alteration of the flow characteristics over the double delta wing on the patterns of the time-averaged streamline at α=15°

Figure 4.34 represents the alteration of the flow characteristics over the double delta wing presented by the patterns of the time-averaged streamlines under the GE at α=25° with the variations of *h/c*. Here, F_c is used to describe the focal point of the coiled-up vortex. Also, in Figure 4.34, the ground effect as a function of the distance, y_f between the middle of the semi span of the wing and the location of the foci, *F* is normalized with the semi span length, *s* and symbolized as y_f/s is presented. It is indicated from Figure 4.34 that the inboard movement of the coiled-up vortex along the spanwise direction over the double delta wing occurs under the GE; in other words, the foci of the coiled-up vortex, F_c move toward the central axis of the wing as the location of the double delta wing is lowered to *h/c*=0.1. For example, while the change of the distance between the middle of the semi span and the location of foci is found to be y_f /*s*=0.098 in the region of GFC, the foci of the coiled-up vortex, F_c moves towards the wing center to the locations of y_f /*s*=0.134 and 0.216 when the double delta wing descends from the GFC region to the *h/c*=0.55 and 0.1 cases, respectively.

The patterns of the time-averaged streamlines under the GE with the variations of *h/c* at α=25° in side-view planes were demonstrated in Figure 4.35. The results were measured only over a specified portion of the flow field throughout the complete chord of the double delta wing to define the exact location of the VB and its size, which is one-third of the chord length. The VB locations can also be viewed in Figure 4.32 with the dye observations. The parameter of *z/s* is a normalized distance, and it is expressed as the distance, z between the wing surface and the VB position divided by the span length, *s*. As seen from Figure 4.35, *z/s* decreases when the double delta wing descends from the region of GFC into the region affected by the presence of the ground surface, revealing that the rate of interactions between the wing surface and the vortical flow is magnified. For example, while *z/s* is equal to 0.075 in the region of GFC, then *z/s* is found to be 0.067 and 0.062 when the position of the double delta wing is lowered from the region of GFC to the *h/c*=0.55 and 0.1 cases, respectively. In addition, the interaction between the vortical flow and the wing surface continues to increase in line with the decrease in *h/c*, resulting in early VB formation and, therefore, irregularities in the vertical flow structures downstream of the VB continue to increase. In other words, the amplified irregularities in the vortical flow result in an increment in the complexity and intensity of unsteady flow, which may cause the wings to vibrate, and hence an attenuation of aerodynamic performance takes place as reported by Gursul (2005). However, it is observed that the vortex symmetry worsens as the double delta wing moves from the GFC field to the GE field.

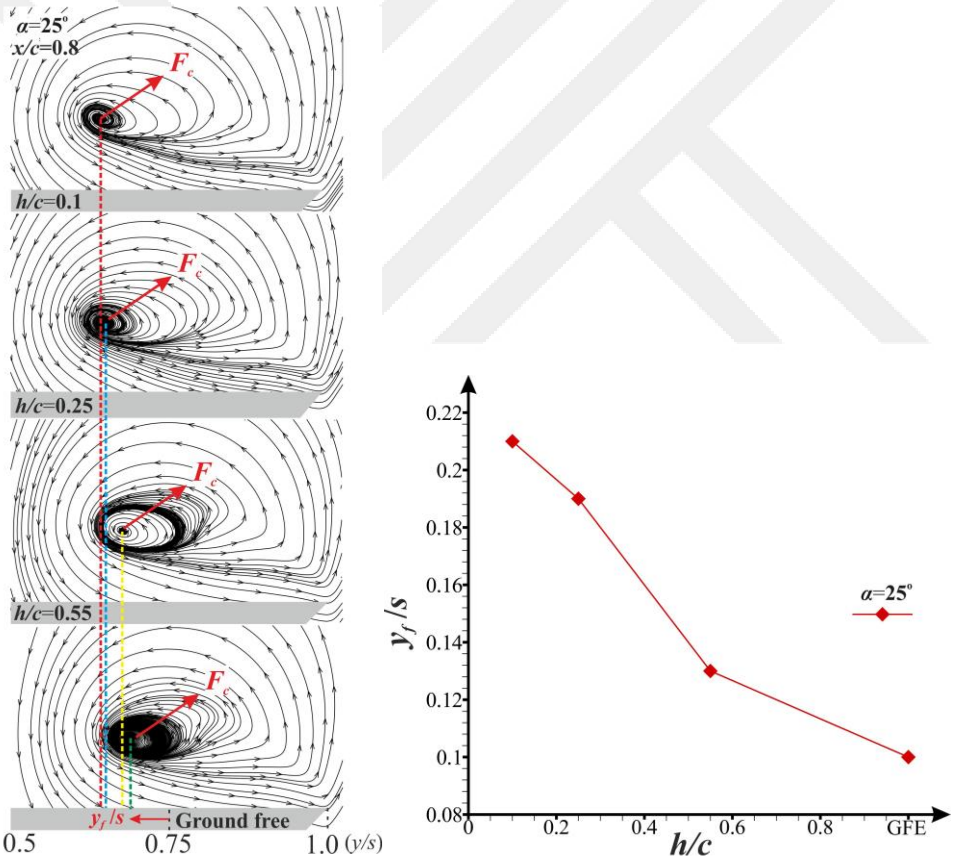

Figure 4.34. The change of the time-averaged streamline patterns at α=25° with the variations of *h*/*c*, and the alteration of the distance from the middle of semi-plan to foci points on the patterns of the time-averaged streamline, y_f/s in the cross-flow plane

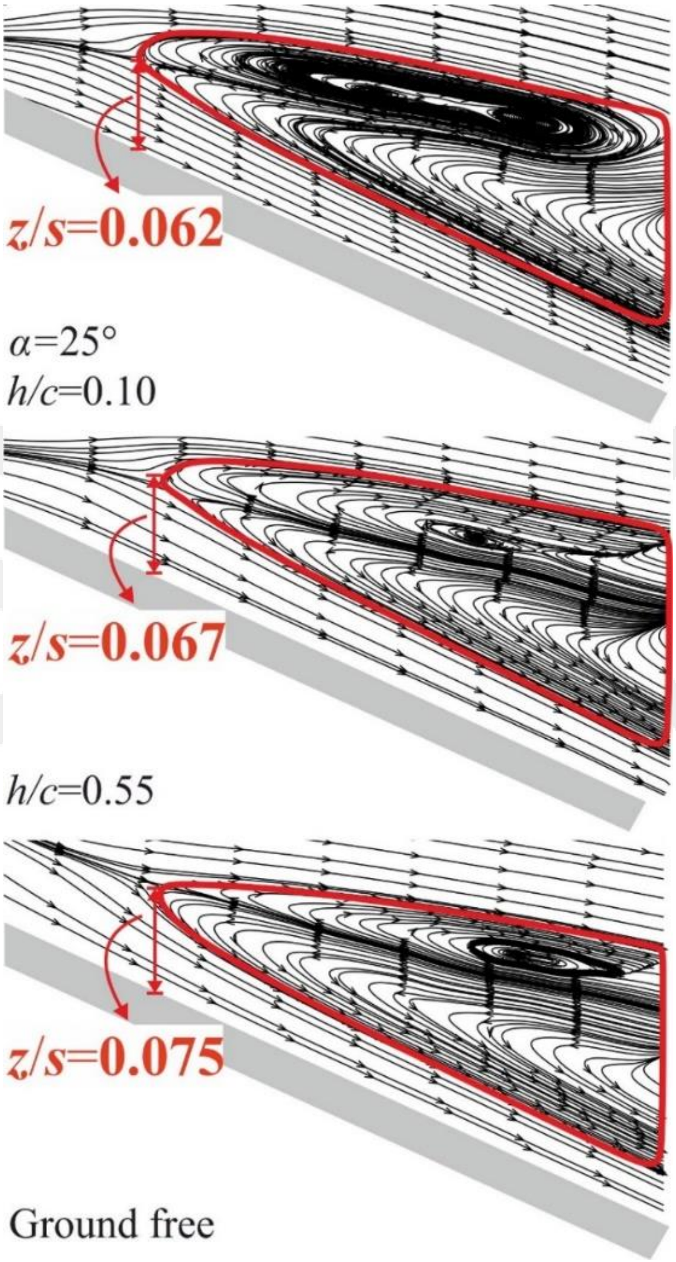

Figure 4.35. The alteration of the distance between the surface of the double delta wing and the VB location of the time-averaged streamline patterns, *z/s* at α=25° with the variations of *h/c* in the side-view plane

As seen from Figure 4.36, the GE on the instantaneous streamline patterns for *h/c*=0.1 and the GFE case in the side-view plane at α=25° was conducted. F^- and F^+ define the foci that act in clockwise and counterclockwise rotation, respectively. It is indicated that the interaction between the LEV and the surface of the double delta wing increases when the delta wing lowers to the ground. While the Kelvin-Helmholtz (K-H) vortices, F^+ and F^- move in a certain order at the GFE case as the delta wing descends to the ground. However, as the ground distance decreases, the unsteadiness and the disorganization of the K-H vortices increase as a result of the interaction between the LEV and the surface of the double delta wing.

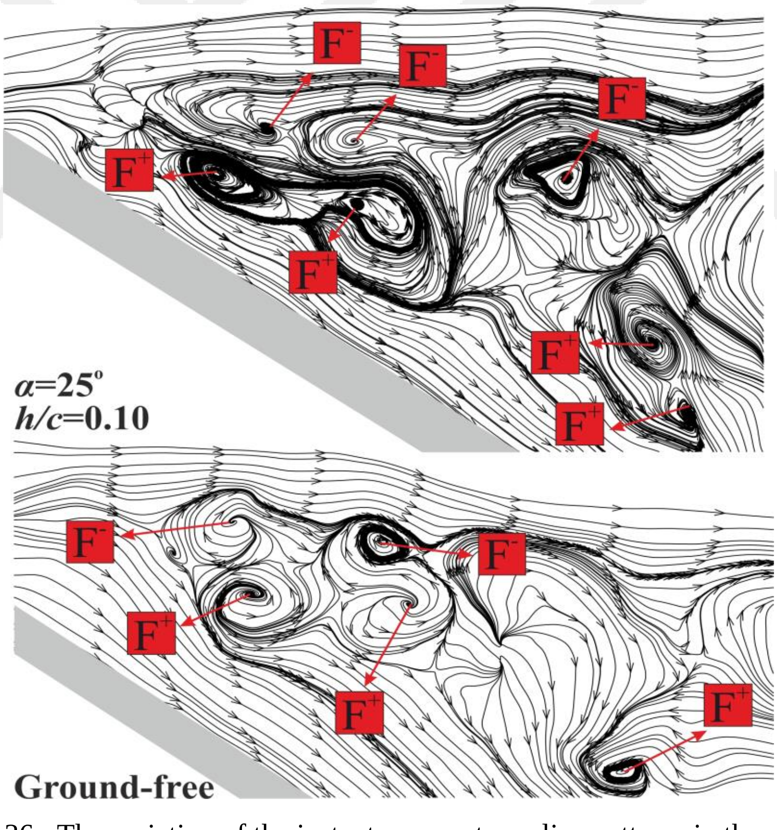

Figure 4.36. The variation of the instantaneous streamline patterns in the side-view plane under the ground effect for *h/c*=0.1, and the GFE case at α=25°

The influences of the ground on the structure and the magnitude of the concentration of the strake, wing, and secondary vortices which are seen over the double delta wing at α=15° and the coiled-up vortex at α=25° were indicated in Figure 4.37-38, respectively. The secondary vortices rotated in the opposite direction of the strake and wing vortices are formed because of the flow separation induced by the interaction between the strake vortices and the boundary layer of the double delta wing. The magnitude of the vorticity concentration is normalized as $w^*=wc/U_\infty$. Furthermore, the maximum magnitude of the dimensionless vorticity concentration, $w^*=wc/U_\infty$, in the core region of the coiled-up vortex slightly increases at α=25° when the double delta wing moves from the GFC flow field to the GE flow field as seen in Figure 4.38. However, the normalized intensity of the strake, wing, and secondary vorticities gradually drops when the double delta wing position is lowered to a level close to the wing surface at α=15° the GE induces an earlier VB. For example, the normalized intensity of the strake, wing, and secondary vorticities are found as w^*=52, 24.2, and -24.1 at α=15° at the GFC, respectively. It was also indicated that the magnitudes of these vorticities, w^* progressively decrease as w^*=51.2, 49.8, and 49.4 as strake vorticity, and w^*=23.4, 22.2, and 21.9 as wing vorticity, and w^*=-23.5, -22.7, and -21.8 for the secondary vorticity at h/c=0.55, 0.25 and 0.1, respectively. The reduction in the peak magnitude of the vorticity, w^* concentration of the coiled-up vortex under the GE was also observed at α=25°. The reduction in the peak magnitudes of w^* may be induced because of the insufficient area for the flow between the wing surface and the ground surface to develop. Furthermore, the coiled-up vorticity, w^* concentration at the core region was seen as very low. The reduction in the peak magnitudes can be attached to the GE, which causes the coiled-up vortex to induce an earlier VB because of growth in the gradient of the adverse pressure on the bottom of the double delta wing through the chordwise direction. Moreover, the intensity of w^* over the wing decreases with the enhancement in the angle of attack from α=15° to 25°.

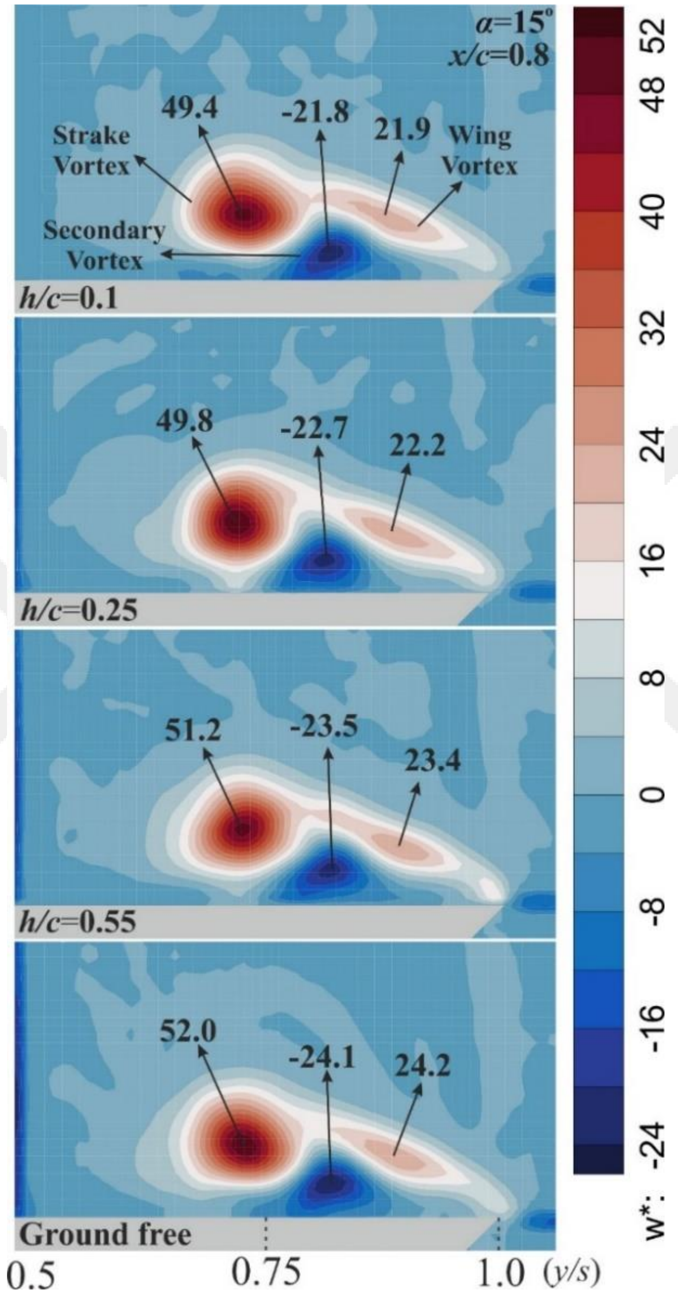

Figure 4.37. The alteration of the time-averaged normalized vorticity concentrations at α=15° under the GE with the variations of *h/c*

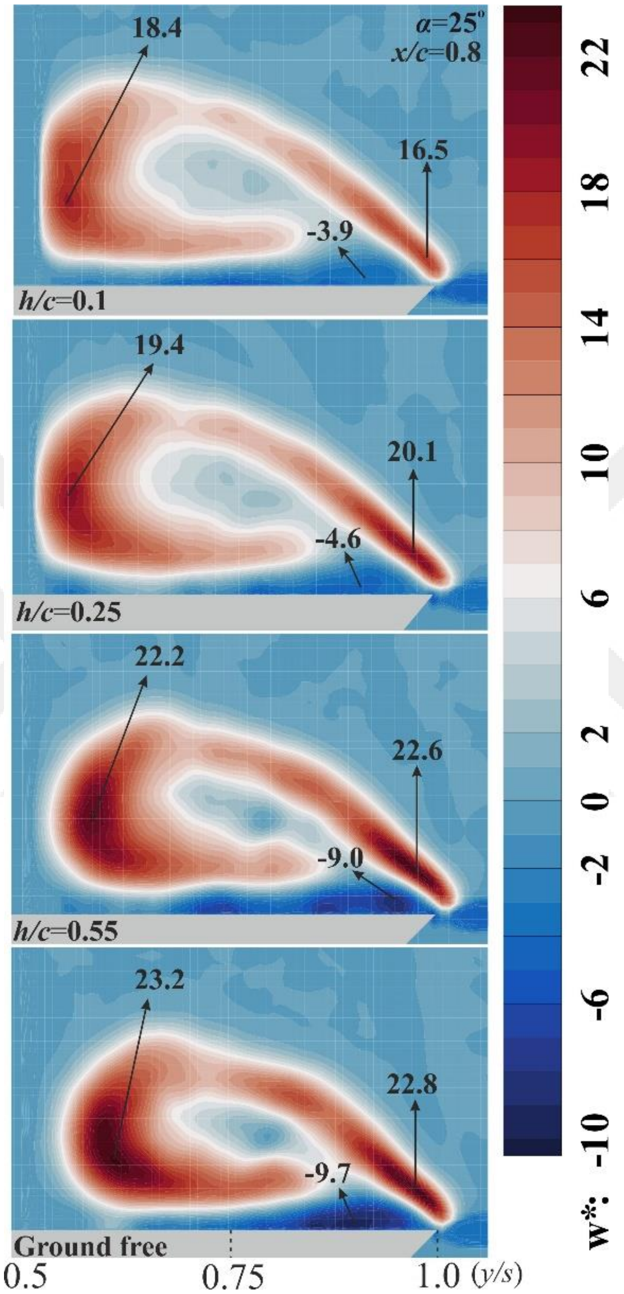

Figure 4.38. The alteration of the time-averaged normalized vorticity concentrations at α=25° under the GE with the variations of h/c

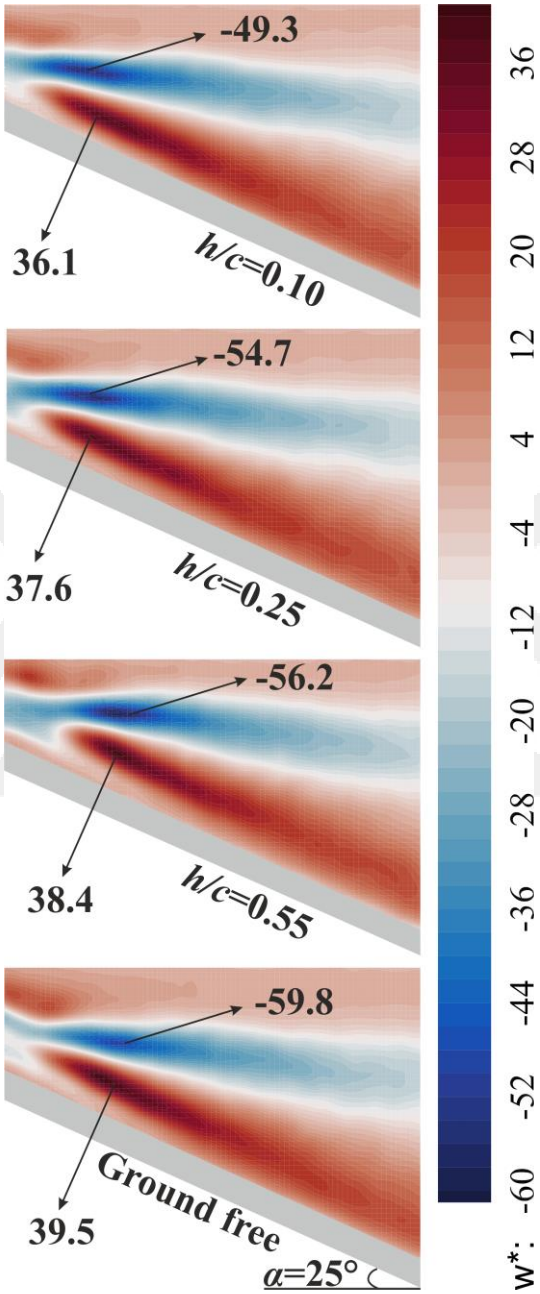

Figure 4.39. The alteration of the time-averaged normalized vorticity concentrations at α=25° under the GE with the variations of *h/c* in the side-view plane

The GE on the flow structure presented in terms of the patterns of the instantaneous streamline for the GFC and *h/c*=0.1 at α=15° are demonstrated in Figure 4.40. The three different frames of the instantaneous patterns of the streamlines were taken to show the instantaneous flow behavior under the GE at different time intervals. It is observed from the instantaneous streamline patterns that the size of the strake vortex is enlarged when the position of the delta wing lowers from the region of GFC to the level of *h/c*=0.1. Also, the descending movement of the foci is defined by the instantaneous streamline patterns of the strake vortex, F_{st} occurs with decreasing the ground distance *h/c*, which is consistent with the patterns of the time-averaged streamline. The foci of the secondary vortex, F_s are detected at *h/c*=0.1 because of the unsteadiness and the growing interaction between the vortical flow and the surface of the double delta wing. The foci of the wing vortex, $F_{w,}$ move away from the wing surface, and the height of the wing vortex increases as the double delta wing gets closer to the ground. Also, the wing vortex moves inboard and interacts more with the strake vortex.

The three different frames of the instantaneous vorticity concentrations presented with patterns of streamlines were taken in the GFC and *h/c*=0.1 case at α=15° and *x/c*=0.8, as shown in Figure 4.41. It has been displayed that the unity of the strake, wing, and secondary vortices deteriorates when the wing position is set from the GFC to *h/c*=0.1. It is observed that the instantaneous vorticity concentration expands the strake vortex resulting in covering the larger region throughout the spanwise direction of the delta wing at *h/c*=0.1 in comparison with the GFC. Besides, it is indicated that the intensity of the vorticity concentration of the strake, wing, and secondary vortices are reduced with the augmentation of the ground proximity when the double delta wing moves from the free-stream flow region close to the ground surface, *h/c*=0.1, because the GE induces an earlier VB.

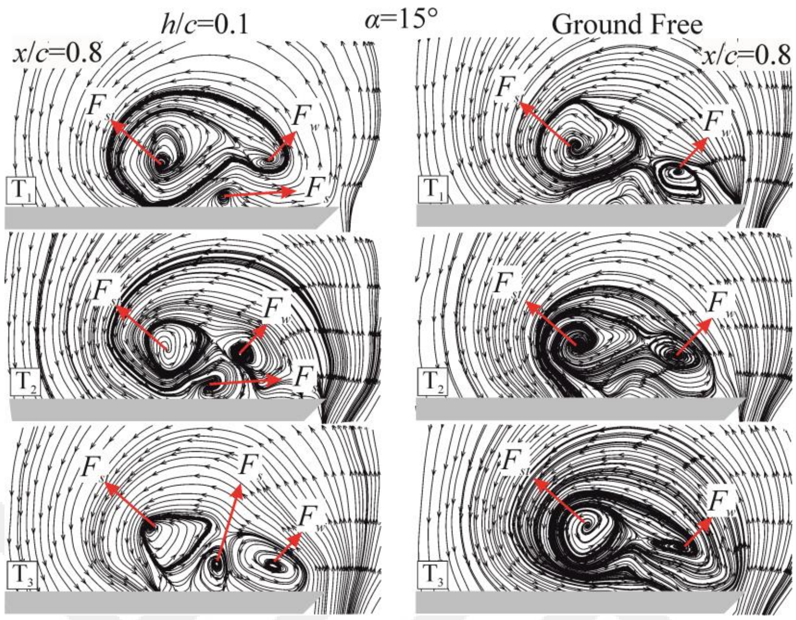

Figure 4.40. The instantaneous streamline patterns in the cross-flow plane at α=15° and *x/c*=0.8 for *h/c*=0.1 and GFE

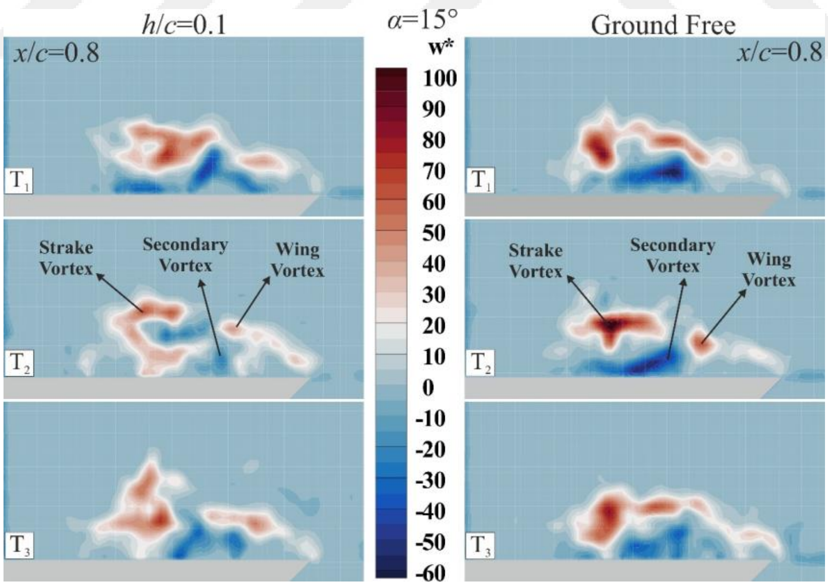

Figure 4.41. The instantaneous vorticity patterns in the cross-flow plane at α=15° and *x/c*=0.8 for *h/c*=0.1 and GFE

As the wing enters the flow region where the ground begins to influence the flow turbulence, the kinetic energy as a function of *h/c* at *α*=15° and 25° was calculated with the equation:

$$TKE = \frac{1}{2}\left(\frac{\sqrt{\overline{u'}^2 + \overline{v'}^2}}{U_\infty^2}\right)$$

The obtained results of *TKE* are given in Figure 4.42-44. The conversion of flow energy to heat because of work done by viscous stresses can be validated by the change in the dispersion of the turbulent kinetic energy, which is associated with the degree of turbulence generation in shear flows stated by Canpolat et al (2012). The variation of large VB fields caused by the gradient of the adverse pressure throughout the chordwise direction on the pressure surface of the double delta wing is dependent on the ground proximity. The widening flow separation is associated with the flow interference induced by the reduction of the area between the wing surface and the ground surface, which is also stated by Qu et al (2015). The magnitude of the TKE gets higher with increasing proximity to the ground because of this flow phenomenon explained above. Also, the peak magnitude field of the TKE enlarges throughout the spanwise direction over the wing with an increase of the GE. In summary, the magnitude and the area of TKE distributions along the surface of the wing with decreasing the ground distance, *h/c*=0.1, is higher in comparison with the GFC. For example, while the value of the pic value of TKE at the GFC was found as 0.09, the value of TKE at *h/c*=0.1 increased to 0.1095. In addition, as seen from Figure 4.44, it was observed that the results in the side-view plane supporting the results in the end-view plane in Figures 4.42 and 4.43 were coherent with each other as well.

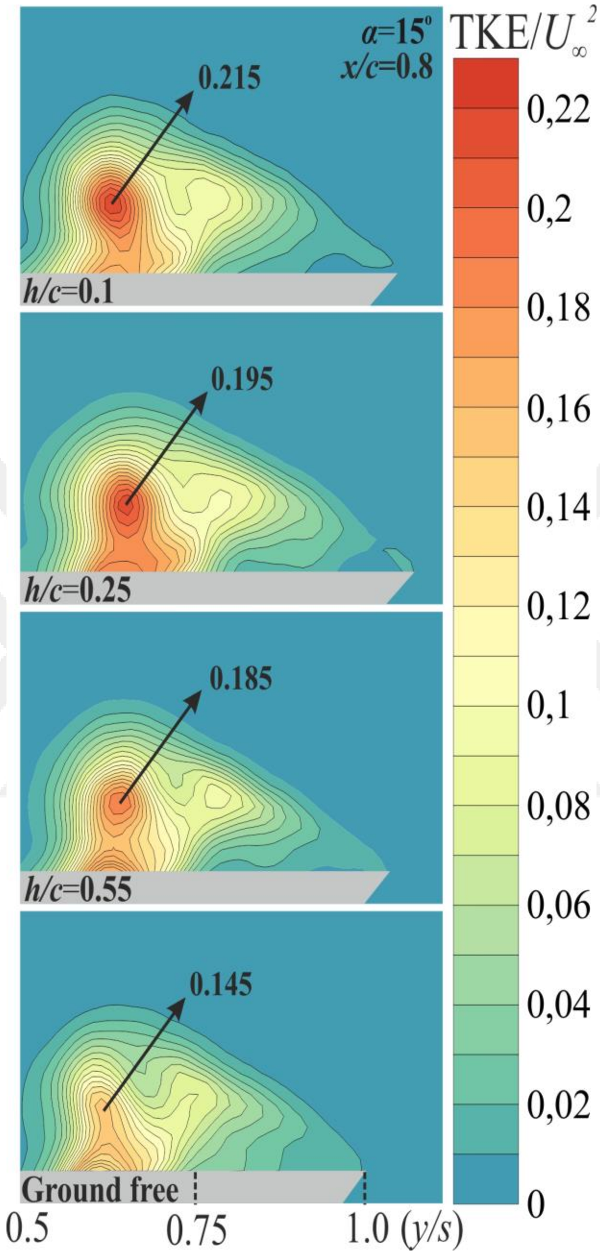

Figure 4.42. The alteration of the time-averaged TKE at α= 15° under the GE with the variations of *h/c*

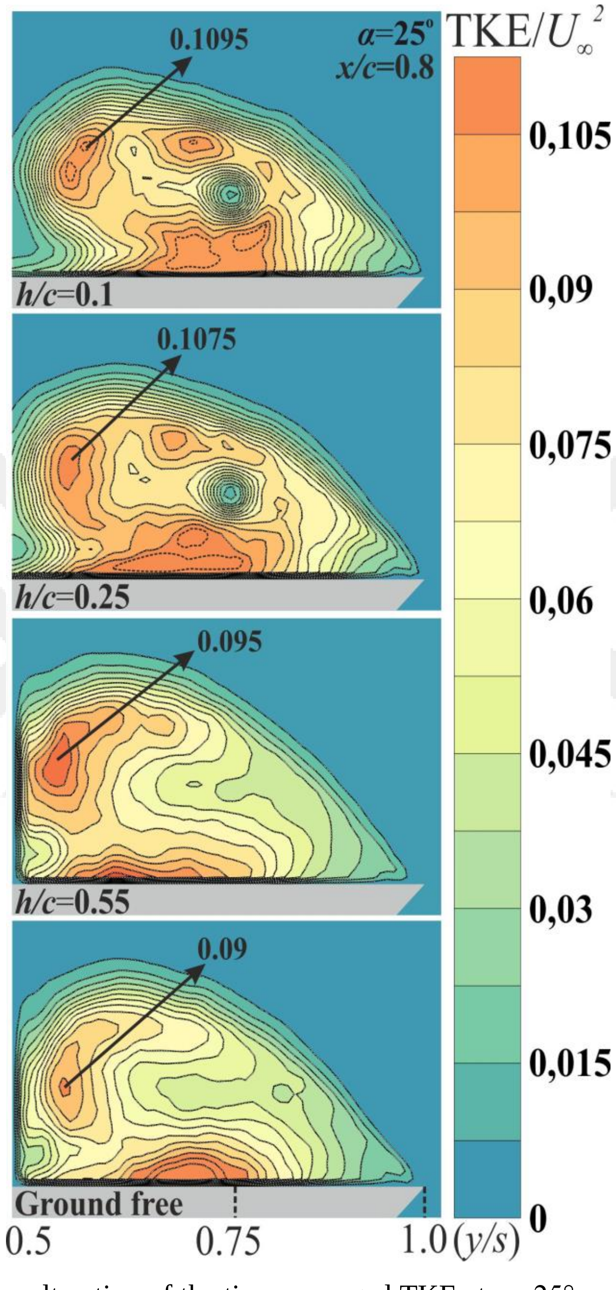

Figure 4.43. The alteration of the time-averaged TKE at *α*= 25° under the GE with the variations of *h/c*

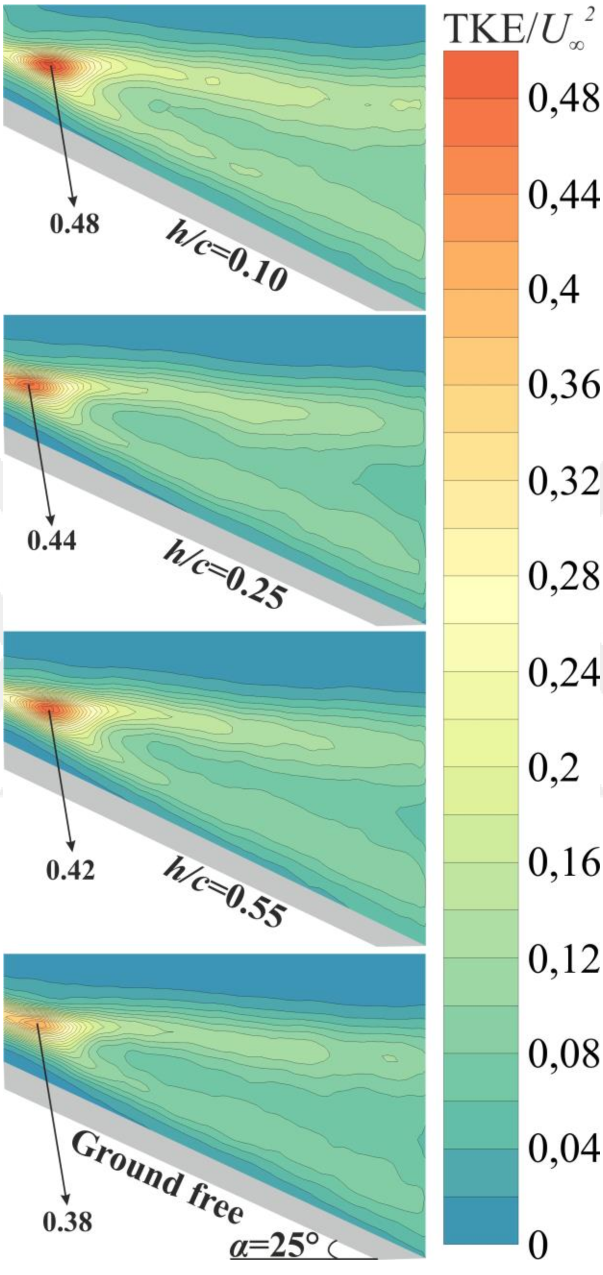

Figure 4.44. The alteration of the time-averaged TKE at *α*= 25° under the GE with the variations of *h/c* in the side-view plane

The GE on the density of the power spectrum (DPS) of the vertical component of the flow velocity, *w,* in a cross-flow plane at α=25° is shown in Figures 4.45-48. The Strouhal number, *St*, is the dimensionless number regarding pulsating flow in the natural environment and is presented as follows:

$$St = \frac{fc}{U_\infty}$$

where *c* is the chord length of the double delta wing, *f* is the frequency of vortex shedding at VB, and U_∞ is the free-stream flow velocity. Since the free-stream flow velocity and the chord length of the double delta wing are constant throughout the experiments, the Strouhal number, *St*, only varies with the frequency of vortex shedding at VB. So that, the change in the Strouhal number, *St* can be interpreted by examining variations in the frequency of these vortex shedding at the VB. The dominant peak frequencies were taken in five points (1 to 5). In Figures 4.45-48, it is seen that the dominant peak frequency, *f* decreases when the double delta wing moves from the GFC field to the GE field. For example, *f* over the wing under the GFC was noticed as 1.54, 2.482, 5.603, 3.371, and 2.939 from points 1 to 5, respectively. Likewise, *f* at the maximum GE case, *h/c*=0.10 was equal to 1.011, 1.093, 1.462, 0.849, and 1.155 from points 1 to 5, respectively. As can be summarized from the results, the value of *St* decreases by the GE; in other words, the frequency of the VB, *f* decreases. The reduction in *St* under the GE can be associated with the slowing down of the formation of vortical flow because of intensive interactions between the vortical flow over the wing and the delta wing surface. The intensive interaction, the augmentation of flow complexity, and the underdevelopment of vortices over the wing under the GE were indicated by Ozden et al (2020). In the study of Prasad and Damodaran (2013), it is expressed that the GE causes a drop in *St*, which means a decrease in the vortex shedding frequency, *f* due to the slower vortex formation through the trailing edge of the NACA-0012 wing.

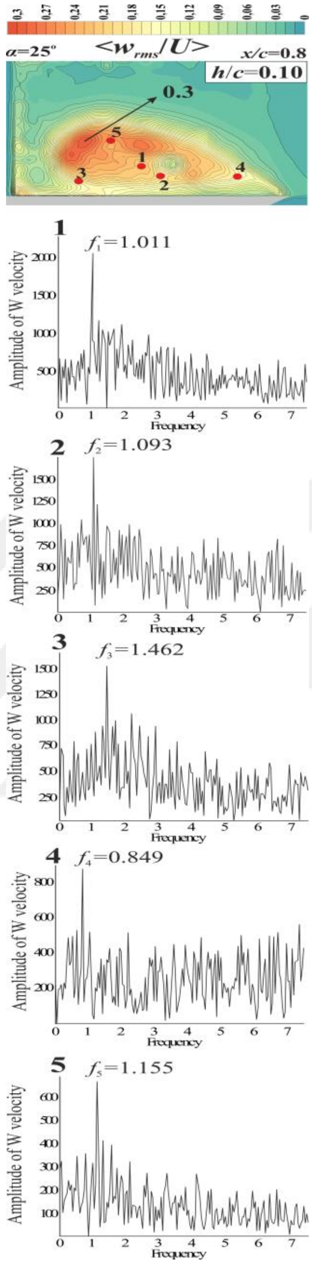

Figure 4.45. The alteration of the density of the power spectrum (DPS) of velocity component in the vertical direction, w_{rms} at α=25° under the GE with the variations of *h/c*

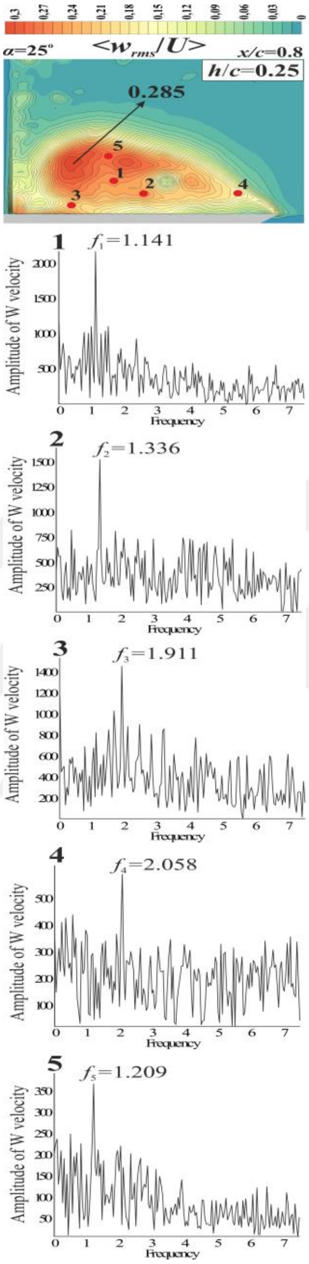

Figure 4.46. The alteration of the density of the power spectrum (DPS) of velocity component in the vertical direction, w_{rms} at α=25° under the GE with the variations of *h/c*

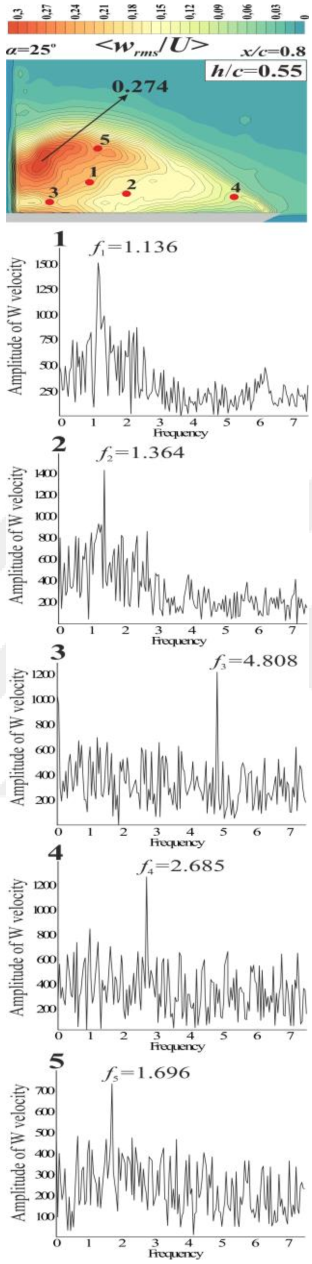

Figure 4.47. The alteration of the density of the power spectrum (DPS) of velocity component in the vertical direction, w_{rms} at α=25° under the GE with the variations of *h/c*

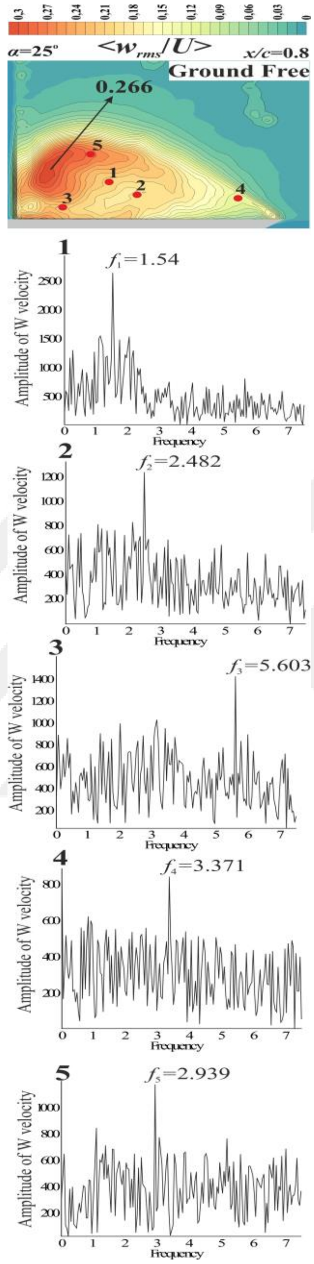

Figure 4.48. The alteration of the density of the power spectrum (DPS) of velocity component in the vertical direction, w_{rms} at α=25° under the GE with the variations of *h/c*

A comparison of the lift coefficient, C_L of double delta wings of Λ=70°/40° reported by Sharma et al (2018) and Λ=65°/35° by Naeini et al (2019) with the present study in the range of angles of attack of 5°≤α≤40° are demonstrated in Figure 4.49. The lift coefficient measurements of Sharma et al (2018) and Naeini et al (2019) were conducted at Re=1.89$x10^5$ and $2x10^6$, respectively. It can be said that the result of the current study is in good agreement with the published studies shown in Figure 4.49. It was also observed that the effects of parameters such as experimental uncertainties, geometrical attachments, the thickness/chord ratio, and the bevel angle of the delta wing did not have great effects on the results presented in Figure 4.49. For example, in the study of Sharma et al (2018), a rectangular part attached to the trailing edge of the double delta wing having Λ=70°/40° was illustrated. Also, the double delta wing having Λ=65°/35° tested by Naeini et al (2019) has a bevel angle of 24° at leading edges.

In Figures 4.50-52, the GE on the aerodynamic properties of the double delta wing having Λ=70°/40° is examined under the variations of h/c within the range of angles of attack 5°≤α≤45°. The variations of the lift coefficients, C_L, with altering α under the GE are demonstrated in Figure 4.50. When α exceeds 10°, the variation in C_L starts to be seen under the GE in comparison with the GFC. While the double delta wing approaches the stall field at α=30°, C_L gradually enhances when the ground distance decreases from the GFC to the case of h/c=0.10. For example, the percentage of increase in the lift coefficient, ΔC_L between the GFC and the h/c=0.1 case is detected as ΔC_L=4.8%, 5.3%, 6.8% when α is adjusted as 15°, 20°, and 30°, respectively. When the double delta wing descends from the GFC region into the GE region, the values of C_L decrease less in the post-stall field in comparison with the GFC. For example, the percentage decrease in C_L is 5.3% and 7.9%, at h/c=0.1 at α=40°, and 45°, which is less in comparison with the GFC. The increase in C_L caused by the GE is considered to be associated with an increase in the ram pressure with increasing proximity to the ground. Moreover, the aerodynamic properties are positively affected by the strengthening of the GE because of the dynamic air cushion that ensued because of an increase in the pressure on the bottom of the wing through the air stagnation in the area between the wing surface and the ground surface. The effect of the dynamic air cushion is impaired by reducing the proximity to the ground because of the diminishing ram pressure.

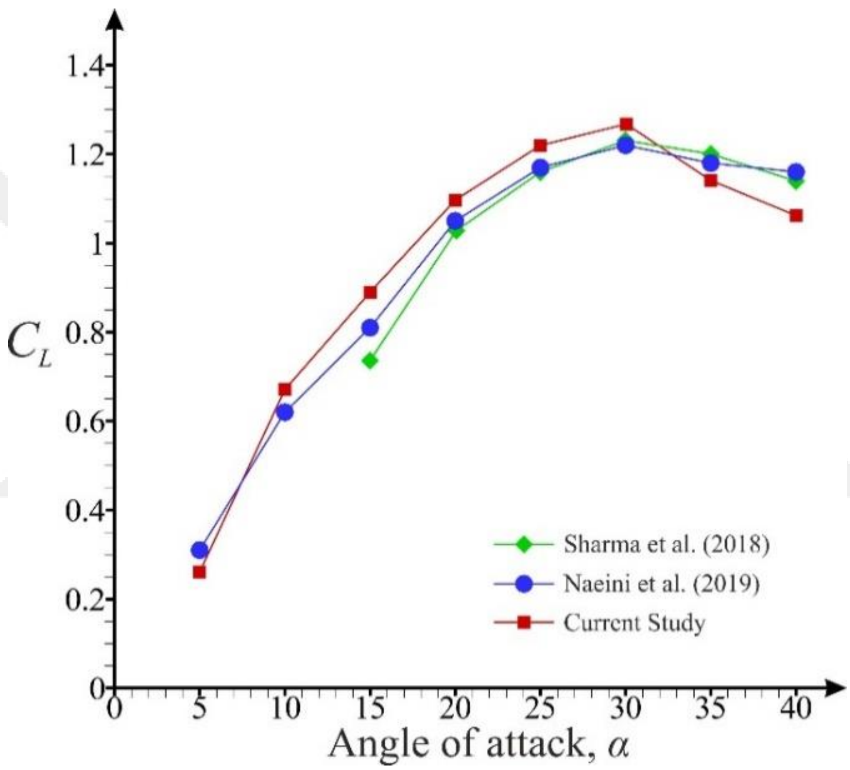

Figure 4.49. The comparison of C_L between the present study of a double delta wing and similar studies reported by Sharma et al. (2018) and Naeini et al. (2019)

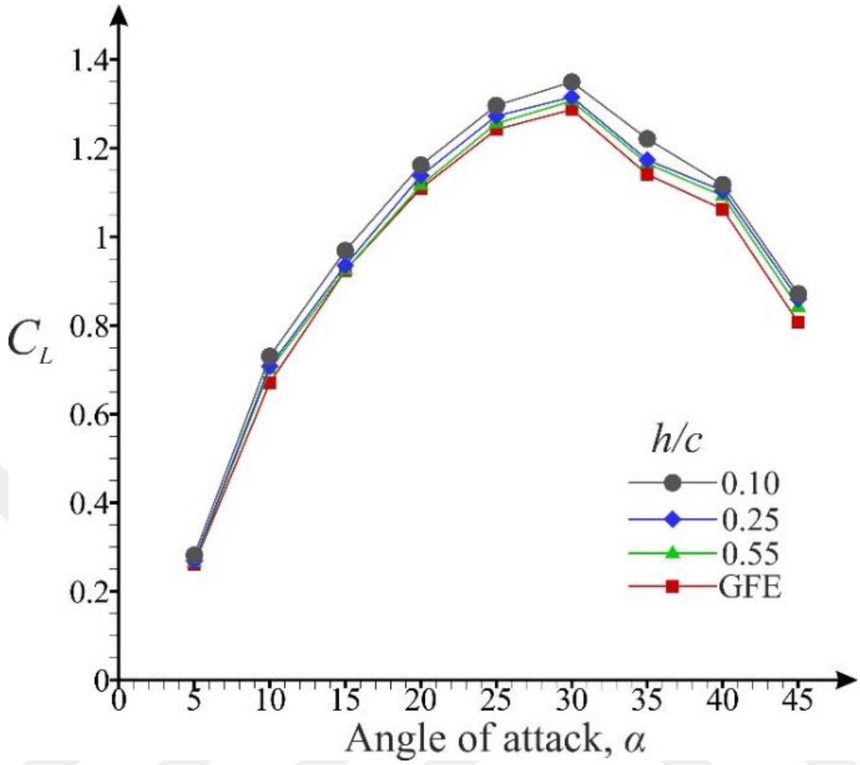

Figure 4.50. The alteration of the lift coefficients, C_L of the double delta wing within the range of angles of attack 5°≤*α*≤45° under the GE with the variations of *h/c*

In Figure 4.51, it is pointed out that strengthening the GE induces a consistently higher drag coefficient, C_D as an independent of α for all ground cases measured. When the higher ground proximity is applied, the higher C_D takes place. The C_D at the extreme ground case, *h/c*=0.10, is continually greater in comparison with the GFC. For example, the percentage augmentation in the drag coefficient, ΔC_D between the GFC and the *h/c*=0.1 case is ΔC_D=14.9% and 18% when α is adjusted as 15° and 20°, respectively.

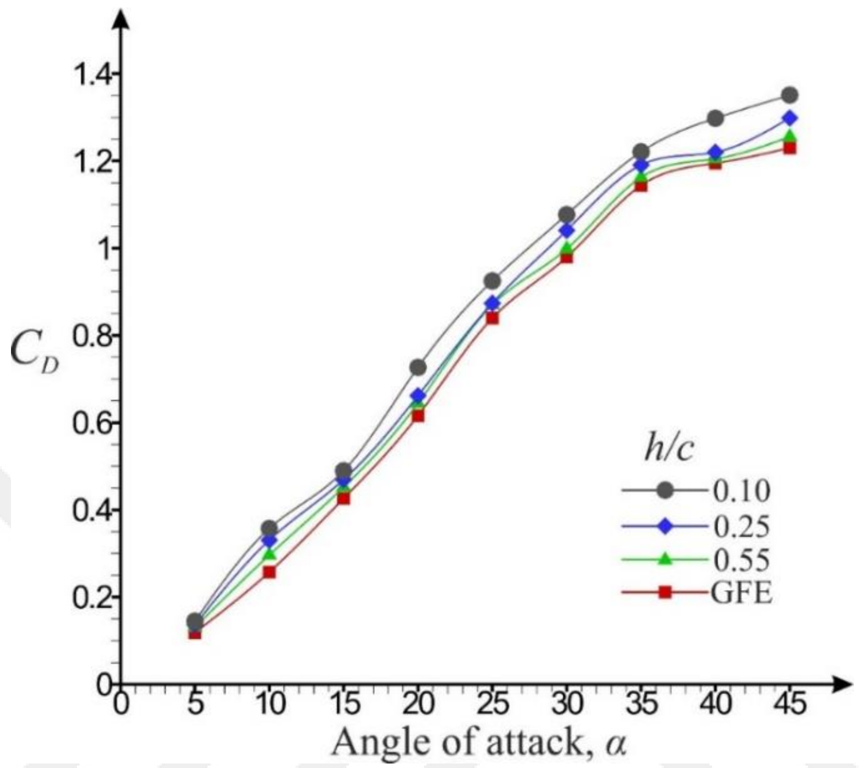

Figure 4.51. The alteration of the drag coefficients, C_D of the double delta wing within the range of angles of attack 5°≤α≤45° under the GE with the variations of *h/c*

It is indicated in Figure 4.52 that the enhancement in the drag coefficient, C_D, is dominantly higher than the lift coefficient, C_L, for higher angles of attack, α, which means that the enhancement in C_D is affected by the enhancement in C_L at lower α. The higher increment in C_L compared to the increment in C_D causes a higher lift-to-drag ratio, C_L/C_D to occur at lower α, which points out that the delta wing in the extreme ground case such as *h/c* has higher aerodynamic performance, as mentioned by Lee and Ko (2018).

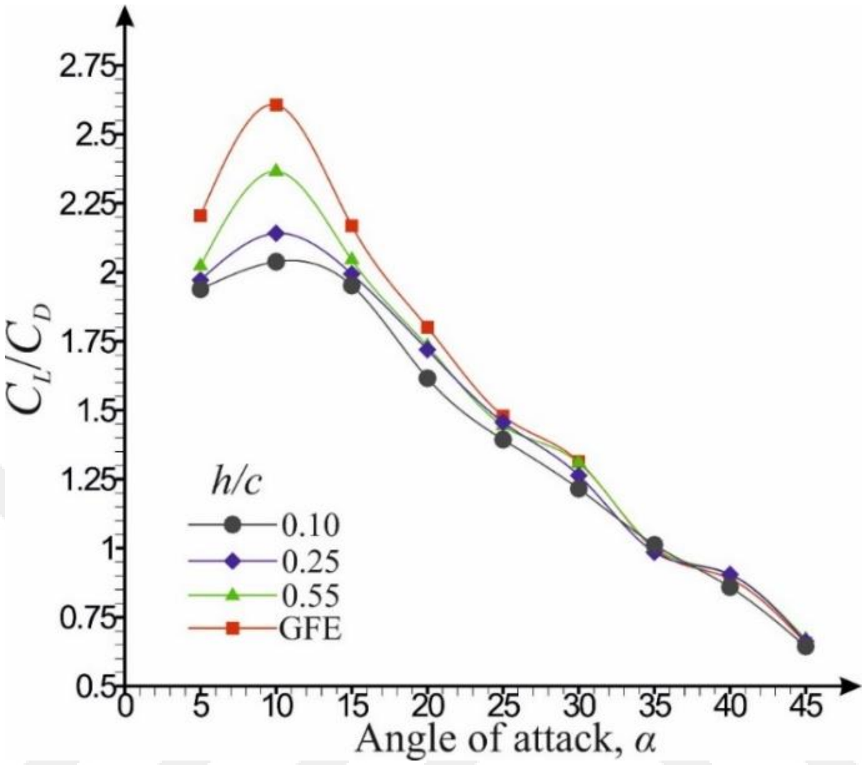

Figure 4.52. The alteration of the lift-to-drag ratio, C_L/C_D for the double delta wing within the range of angles of attack 5°<α<45° under the GE with the variations of*h/c*

The variation of the total circulation under the GE with variations of *h/c* at α=15° and 25° specified in Figure 4.53 is determined using the equation:

$$Total\ Circulation = \frac{\Gamma_0}{U_\infty c}$$

The variation of the total circulation, Γ_o is associated with the aerodynamic characteristics of the vortical flow over the wing, and it is normalized by dividing with free-stream velocity, U_∞ , and, the chord length of the wing, *c*. As indicated in Figure 4.53, the dimensionless total circulation, $\Gamma_o/U_\infty c$ on the double delta wing dramatically augments when the angle of attack increases from α=15° to 25°, which is compatible with the high C_L at a high α. For example, the value of the total circulation increases from 0.285 to 0.44 when α is varied from 15° to 25° at the *h/c*=0.1 case. An increment in dimensionless total circulation, $\Gamma_o/U_\infty c$, under the GE, is also coherent with the augmentation in the C_L. The total circulation, $\Gamma_o/U_\infty c$, progressively enhances when the proximity to the ground increases because of the ram pressure, as pointed out by Gursul and Wang (2018). For example, overall increments in the total circulation are 21.3% and 66% when the position of the double delta wing is varied from the GFC to the GE at α=15° and 25°, respectively.

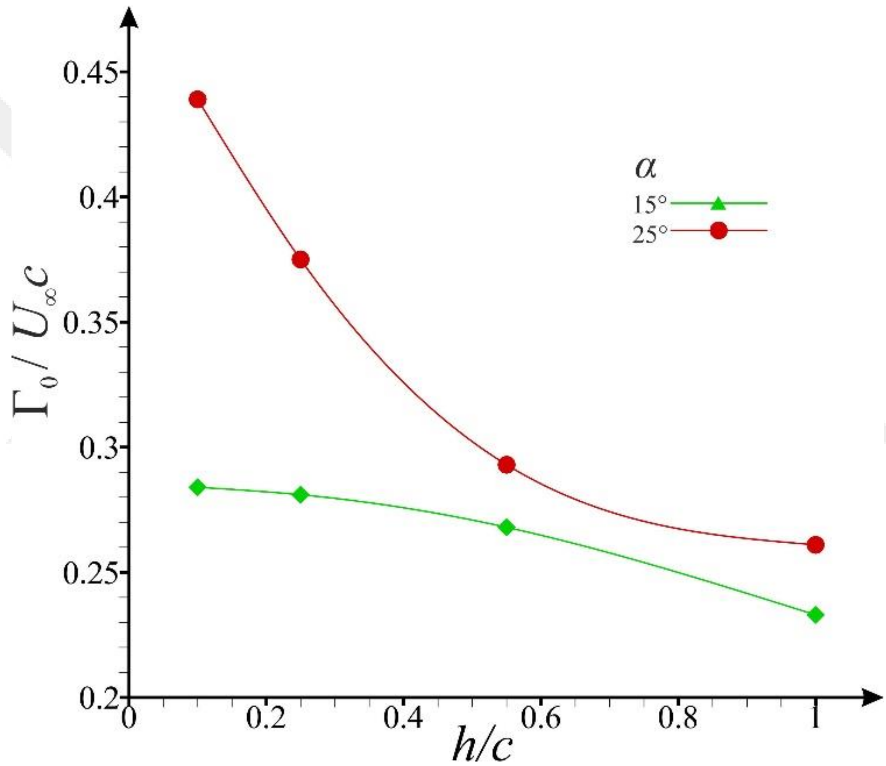

Figure 4.53. The alteration of the total circulation under the GE with the variations of *h/c* at α=15° and 25°

The results of the ground surface impact on the magnitude and the distribution of dimensionless time-averaged velocity vectors, $\langle V\rangle/U_\infty$ over the delta wing under the variations of *h/c* at α=25° are given in Figure 4.54. The selected locations were determined concerning the essential areas on the patterns of the time-averaged streamlines throughout the trailing edge of the double delta wing. For example, line *2* is the focal point of the coiled-up vortex. Furthermore, Lines 1 and 3 are designated as the far region from the wing surface and the near region, respectively. The $\langle V\rangle/U_\infty$ is lower at the leading edge of the wing in comparison with the area towards the central axis for all selected locations on the double delta wing. Moreover, it is indicated that the $\langle V\rangle/U_\infty$ diminishes in Line *3*, in comparison with Lines *1* and *2*. As shown in Figure 4.54, it is observed that the dimensionless value of time-averaged velocity vectors $\langle V\rangle/U_\infty$ increases in most of the vortical flow regions, especially in the close area to the central axis of the wing such as Lines *1*, *2*, and *3*. The ram pressure caused by the dynamic air cushion between the ground and the bottom of the double delta wing slows down the fluid motion near the leading edge of the wing and induces the flow to move inboard towards the wing's central axis along the spanwise. The $\langle V\rangle/U_\infty$ decreases because the GE causes an earlier VB when the double delta wing moves from the GFC field to the GE field. Therefore, the velocity of the flow field increases towards the central axis of the wing because of the ram pressure.

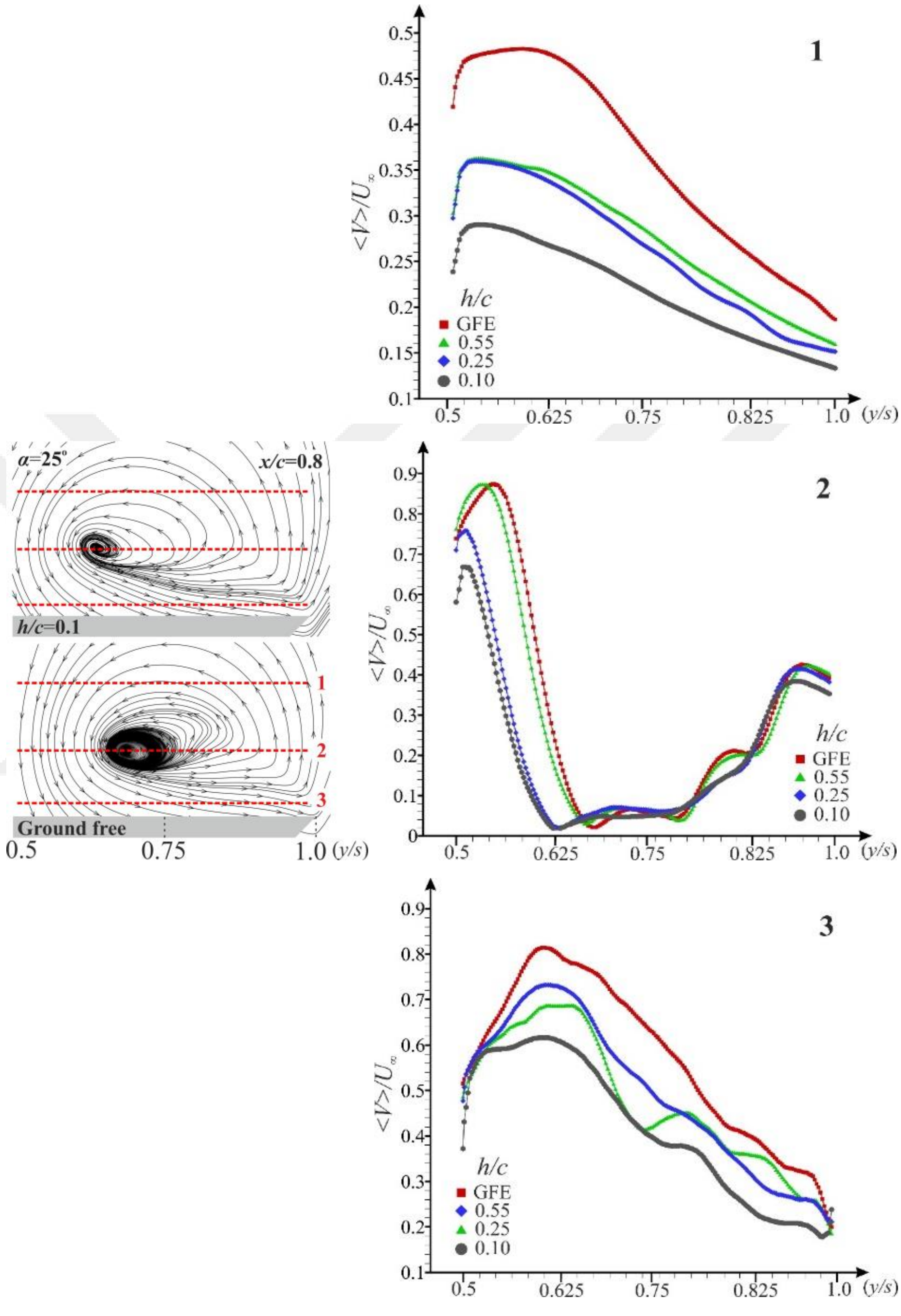

Figure 4.54. The alteration of the total circulation under the GE with the variations of *h/c* at *α*=15° and 25°

5. CONCLUSION

In the part of the investigation of the slender delta wing, the GE on the aerodynamic coefficients and flow behaviors of a 70-deg-swept slender delta wing was studied using dye visualization and the PIV techniques. The angles of attack were applied as α=25° and 35° for the nondimensionalized ground distances, *h/c*=0.1, 0.25 0.55, and GFE case. As seen from the dye images, the GE causes the earlier breakdown location of the LEVs over the delta wing compared to the GFE case. The GE-induced premature VB can be based on an increase in the magnitude of the adverse pressure gradient on the suction side of the delta wing along the chord direction. The interaction between the wing's surface and the LEV decreases when the GE decreases. Also, the inboard movement of LEVs was observed, which means that the central axis of the leading-edge vortex moves toward the wing's central axis when the delta wing descends to the ground. In addition, this inboard movement can also be detected from time-averaged streamline patterns, and it is also observed that focal points, *F*, move towards the central axis of the wing. The vertical distance, *z/s*, decreases when the h/c increases, which indicates that the LEV is in more significant interaction with the boundary layer of the turbulent flow over the surface of the slender wing under the case of *h/c*=0.1 compared to the ground free effect (GFE) of the flow field. Also, this interaction causes a larger vortex core region compared to the GFE case as the delta wing approaches the ground. As a result of instability and increased interaction between the LEV and the delta wing surface, multiple focal points, F_{m}, are observed at extreme GE of *h/c*=0.1. It can be concluded from the vorticity concentrations that the LEVs spread over the wider region along the trailing edge of the delta wing and the intensity of LEVs attenuates with descent from the ground free-flow field into the extreme GE field. The magnitude of the turbulent kinetic energy, TKE increases when the delta wing descends to the ground using a flow phenomenon of the flow separation expanding under the GE related to the flow blockage caused by the reduction in the gap between the delta wing and the ground. Besides, a PSD distribution with lower magnitudes of the local peaks spread over the wing surface is observed due to strong fluid-structure interaction as a result of the GE. This interaction causes the unsteady and sophisticated flow structure over the delta wing. Finally, the aerodynamic coefficients, C_L and C_D, were observed to increase with reducing *h/c*. The increment of the lift-to-drag ratio, C_L/C_D by the GE is higher, and the maximum proportion of C_L/C_D takes place at smaller α's. The value of $<V>/U_\infty$ is higher in the region towards the wing's center compared to the leading edge of the wing for all measured locations on the wing. Also, it was seen that the magnitude of $<V>/U_\infty$ decreases in the region far from the wing surface, Line *3*, compared to Lines *1* and *2*.

In the part of the investigation of the double delta wing, the experimental investigations were conducted to see the influences of the ground surface on the formation of the vortical flow over a double delta wing having a sweep angles ratio of Λ=70°/40° with the alteration of the ground distance, *h/c*. Dye observations and instantaneous flow measurements using the PIV technique in the water channel and force measurements in the wind tunnel were carried out. The chordwise location over the cross-flow plane was taken as x/c=0.8 for all experiments. Since high angles of attack, α cause the double delta wing to develop the stalled flow, the possibility of the identification of the strake, wing, and secondary vortices becomes challenging, and it is also revealed that the vortices start to move in a large coherent vortex form, which is named as "coiled-up vortex" when the angle of attack alters from α=15° to 25°. The occurrence of the VB at an earlier stage over the double delta wing with the alteration of the ground distance, *h/c* under the GE, was noticed in comparison with the GFC at α=25°. The GE induces the VB of the coiled-up vortex to form at an earlier stage due to the increase in the gradient of the adverse pressure on the bottom of the double delta wing through the chordwise direction. The vortex oscillation increases with the irregularities in the flow as the double delta wing descends to the flow field affected by the presence of the ground surface. Here are the definitions of F_s, F_w, z_s/s, z_w/s, y_v/s, and θ_{sw}. z_s/s and z_w/s are used to define the distance between the foci of the strake and wing vortices, F_s and $F_{w,}$ and the wing surface. y_v/s is the distance between the foci of the strake and wing vortices. While the z_s/s decreases, the z_w/s increases because the GE induces the strengthening of interaction between the vortical flow and the wing surface when the ground distance, *h/c,* decreases. The dynamic air cushion causes the wing vortex to move away from the wing surface, although the interaction rate between the wing surface and the ground increases. Also, the inboard movement of the coiled-up vortex from the leading-edge side to the wing central axis along the spanwise direction over the double delta wing occurs when the delta wing position is altered from the region of GFC to the case of *h/c*=0.1. The decrease in the peak magnitudes of the vorticity concentration of the strake, wing, secondary and coiled-up vortices increases the ground distance, h/c occurs at both angles of attack such as α=15° and 25°. Because the insufficient area for the development of the flow between the wing surface and the ground is evident. The peak magnitütes of the TKE appear to spread over a wider area along the spreading direction of the double delta blade. It is seen that the peak magnitudes of the TKE appear to spread over a wider area throughout the spanwise direction of the double delta wing under the strengthening of the GE as a function of *h/c* in comparison with the GFC. It was observed from the density of power spectrum (DPS) analysis that when the delta wing approaches the ground surface, the values of the dominant peak frequency of vortex shedding at the VB decrease. Since the Strouhal number decreases because of the slowing down of the formation of the vortical flow over the double delta wing with increasing the proximity to the ground. The augmentation in C_L begins to occur under the GE compared to the GFC when the angle of attack, α, is taken greater than α=10°. The strengthening of the GE induces the drag coefficient, $C_{D,}$ to increase for all ground cases. As the higher ground proximity is applied, the higher C_D takes place. The higher increment in C_L compared to the increment in C_D causes a higher lift-to-drag ratio, C_L/C_D to occur at a lower α, which points out that the delta wing has higher aerodynamic performance in the extreme ground case arises. The dimensionless total circulation, $\Gamma_o/U_\infty c$ on the double delta wing dramatically augments when the angle of attack increases from α=15° to 25°, which is compatible with a high C_L at high angles of attack, α. The dimensionless total circulation, $\Gamma_o/U_\infty c$, progressively enhances when the proximity to the ground increases because of the ram pressure. Finally, it can be revealed from the values of normalized vectors of the time-averaged velocity, $\langle V \rangle / U_\infty$ at α=25°, that it is lower at the leading edge of the wing in comparison with the region towards the central axis for all selected locations on the double delta wing.

REFERENCES

Ahmed, M. R., and Sharma, S. D., 2005. An investigation on the aerodynamics of a symmetrical airfoil in ground effect, *Experimental Thermal, and Fluid Science*, *29*(6), 633-647.

Ahmed, M. R., Takasaki, T., & Kohama, Y., 2007. Aerodynamics of a NACA4412 airfoil in ground effect, *AIAA Journal*, *45*(1), 37-47.

Akbıyık, H., Yavuz, H., and Akansu, Y. E., 2017. Comparison of the linear and spanwise-segmented DBD plasma actuators on flow control around a NACA0015 airfoil, *IEEE Transactions on Plasma Science*, *45*(11), 2913-2921.

Ali, Z. M., Kuntjoro, W., & Wisnoe, W., 2012. Effect of the canard on the aerodynamic characteristics of blended wing body airplane, In *2012 IEEE Symposium on Business, Engineering and Industrial Applications*, pp. 696-700.

Bleischwitz, R., De Kat, R., & Ganapathisubramani, B., 2018. Near-wake characteristics of rigid and membrane wings in ground effect, *Journal of Fluids and Structures*, *80*, 199-216.

Brett, J., & Ooi, A., 2014. Effect of sweep angle on the vortical flow over delta wings at an angle of attack of 10, *Journal of Engineering Science and Technology*, *9*(6), 768-781.

Canpolat, C., Yayla, S., Sahin, B., & Akilli, H., 2009. Dye visualization of the flow structure over a yawed nonslender delta wing. *Journal of Aircraft*, *46*(5), 1818-1822.

Canpolat, C., Yayla, S., Sahin, B., and Akilli, H., 2012. Observation of the vortical flow over a yawed delta wing, *Journal of Aerospace Engineering*, *25*(4), 613-626.

Canpolat, C., Yayla, S., Sahin, B., & Akilli, H. Ü., 2017. Effects of Trailing-Edge Attachment on the Flow Structure over a Generic Delta Wing, *Journal of Aerospace Engineering*, *30*(5), 06017003.

Chawla, K., Van Dalsem, W. R., and Rao, K. V., 1990. Simulation of a delta wing with two jets in ground effect, *Computing Systems in Engineering*, *1*(2-4), 483-494.

Cui, Y. D., Lim, T. T., & Tsai, H. M., 2007. Control of vortex breakdown over a delta wing using forebody spanwise slot blowing, *AIAA Journal*, *45*(1), 110-117.

Delery J. M., 1994. Aspects of vortex breakdown, *Progress in Aerospace Sciences*, *30*(1), 1-59.

Durhasan, T., & Karasu, I., 2019. Dye visualization over double delta wing with various kink angles, *Journal of Visualization*, *22*(4), 669-681.

Escudier, M., 1988. Vortex breakdown: observations and explanations, *Progress in Aerospace Sciences*, *25*(2), 189-229.

Frost, W., 1983. *Flight in low-level wind shear* (No. NASA-CR-3678), NASA.

Frost, W., & Bowles, R. L., 1984. Wind shear terms in the equations of aircraft motion. *Journal of Aircraft*, *21*(11), 866-872.

Grismer, D. S., and R. C. Nelson., 1995. Double-delta-wing aerodynamics for pitching motions with and without sideslip, *J. Aircr*. 32 (6):1303–1311.

Gursul, I., & Xie, W., 1999. Buffeting flows over delta wings, *AIAA Journal*, *37*(1), 58-65.

Gursul, I., 2003. Review of unsteady vortex flows over delta wings, In *21st AIAA Applied Aerodynamics Conference*, p. 3942.

Gursul I., 2005. Review of Unsteady Vortex Flows Over Slender Delta Wings, *Journal of Aircraft*, *42*(2), 299-319.

Gursul, I., Allan, M. R., and Badcock, K. J., 2005. Opportunities for the integrated use of measurements and computations for the understanding of delta wing aerodynamics, *Aerospace Science and Technology*, *9*(3), 181-189.

Gursul, I., Wang, Z., & Vardaki, E., 2007. Review of flow control mechanisms of leading-edge vortices, *Progress in Aerospace Sciences*, *43*(7-8), 246-270.

Gursul, I., Vardaki, E., Margaris, P., & Wang, Z., 2007. Control of wing vortices. In *Active Flow Control*, pp. 137-151, Springer, Berlin, Heidelberg.

Gursul, I., & Wang, Z., 2018. Flow control of tip/edge vortices, *AIAA Journal*, *56*(5), 1731-1749.

Hainsworth, F. R., 1988. Induced drag savings from ground effect and formation flight in brown pelicans, *Journal of experimental biology*, *135*(1), 431-444.

Hall, M., 1961. A theory for the core of a leading-edge vortex, *Journal of Fluid Mechanics*, *11*(2), 209-228.

Hall, M. G., 1972. Vortex breakdown, *Annual review of fluid mechanics*, *4*(1), 195-218.

Heron, I., & Myose, R. Y., 2005. Impingement of a von kàrmàn vortex street on a delta wing, *Journal of aircraft*, *42*(4), 1084-1087.

International Civil Aviation Organization, 2005. *Manual on Low-Level Wind Shear*.

Jia, Q., Yang, W., and Yang, Z., 2016. Numerical study on aerodynamics of banked wing in ground effect, *International Journal of Naval Architecture and Ocean Engineering*, *8*(2), 209-217.

Jones, B. L., 2005. Experimental investigation into the aerodynamic ground effect of a tailless chevron-shaped UCAV.

Karasu, I., and Durhasan, T., 2020. Flow characteristics over double Delta wings at low Reynolds numbers, *Journal of Aerospace Engineering*, *33*(4), 04020038.

Karasu, I., Tumse, S., Tasci, M. O., Sahin, B., & Akilli, H., 2021. Near-surface particle image velocimetry measurements over a yawed slender delta wing, *Proceedings of the Institution of Mechanical Engineers, Part G: Journal of Aerospace Engineering*, 0954410021999556.

Kawazoe, H., & Morita, S., 2004. Ground effect on the dynamic characteristics of a wing-rock delta wing, In *34th AIAA Fluid Dynamics Conference and Exhibit* (p. 2352).

Ko, L. S., Tremblay-Dionne, V., and Lee, T., 2020. Impact of Ground Proximity on an Inverted Delta Wing, *Journal of Aerospace Engineering*, *33*(5), 04020047.

Lambert, A., & Yarusevych, S., 2019. Effect of angle of attack on vortex dynamics in laminar separation bubbles, *Physics of Fluids*, *31*(6), 064105.

Laynor, W. G., & Roberts, C. A., 1975. A wind shear accident as evidenced by information from the digital flight data recorder, In *Society of Air Safety Investigators, International Seminar, Ottawa, Ont., Canada*.

Le Sueur, M., 1935. Ground Effect on the Take-off and Landing of Airplanes, *Washington, DC: National Advisory Committee for Aeronautics*.

Lee, T., and He, S. M., 2018. The trailing vortices generated by a reverse delta wing with different wing configurations, *Aerospace Science and Technology*, *82*, 378-393.

Lee, M., & Ho, C. M., 1990. Lift force of delta wings, *Appl. Mech. Rev*., 43(9): 209-221.

Lee, T., & Ko, L. S., 2017. Vortex flow and lift generation of a non-slender reverse delta wing. *Proceedings of the Institution of Mechanical Engineers, Part G: Journal of Aerospace Engineering*, *231*(13), 2438-2451.

Lee, T., & Ko, L. S., 2018. Ground effect on the vortex flow and aerodynamics of a slender delta wing, *Journal of Fluids Engineering*, *140*(7).

Liu, J., Sun, H., Liu, Z., & Xiao, Z., 2014. Numerical investigation of unsteady vortex breakdown past 80/65 double-delta wing, *Chinese Journal of Aeronautics*, *27*(3), 521-530.

Lu, Z. Y., & Zhu, L. G., 2004. Study on forms of vortex breakdown over delta wing, *Chinese Journal of Aeronautics*, *17*(1), 13-16.

Lucca-Negro, O., & O'doherty, T., 2001. Vortex breakdown: a review, *Progress in energy and combustion science*, *27*(4), 431-481.

Luo, S. C., and Chen, Y. S., 2012. Ground effect on flow past a wing with a NACA0015 cross-section, *Experimental Thermal and Fluid Science*, *40*, 18-28.

Manshadi, M. D., M. Eilbeigi, M. K. Sobhani, M. B. Zadeh, and M. A. Vaziry., 2016. Experimental study of flow field distribution over a generic cranked double delta wing, Chin. J. Aeronaut. 29 (5): 1196–1204.

Meinhart, and Soloff, 1999. *Cleanvec Software*, Turbulence Laboratory, the University of Illinois at Urbana-Champaign.

Miller, G. D., & Williamson, C. H., 1997. Turbulent structures in the trailing vortex wake of a delta wing, *Experimental thermal and fluid science*, *14*(1), 2-8.

Mitchell, A. M., & Délery, J., 2001. Research into vortex breakdown control, *Progress in Aerospace Sciences*, *37*(4), 385-418.

Munro, C. D., Krus, P., & Jouannet, C., 2005. Implications of scale effect for the prediction of high angle of attack aerodynamics, *Progress in Aerospace Sciences*, *41*(3-4), 301-322.

Musaj, M., & Prince, S., 2008. Numerical and experimental investigation of the aerodynamics of an unconventional w-leading-edge reversed delta wing in ground effect, In *26th Congress of International Council of the Aeronautical Sciences*, Vol. 6, pp. 665-674.

National Transportation Safety Board, 2012. *Crash During Experimental Test Flight, Gulfstream Aerospace Corporation GVI (G650), N652GD, Roswell, New Mexico, April 2, 2011*, Aircraft Accident Report NTSB/AAR-12/02, Washington, DC.

Nelson, R. C., & Pelletier, A., 2003. The unsteady aerodynamics of slender wings and aircraft undergoing large amplitude maneuvers, *Progress in Aerospace Sciences*, *39*(2-3), 185-248.

Ol, M. V. and Gharib M., 2003. Leading-Edge vortex structure of non-slender delta wings at Low Reynolds number, *AIAA Journal*, *41*(1), 16-26.

O'Connor, A., & Kearney, D., 2018. Evaluating the effect of turbulence on aircraft during landing and take-off phases, *International Journal of Aviation, Aeronautics, and Aerospace*, *5*(4), 10.

Ozalp, C., Pinarbasi, A., & Rockwell, D., 2003. Self-excited oscillations of turbulent inflow along with a perforated plate, *Journal of Fluids and Structures*, *17*(7), 955-970.

Ozden, K. S., Karasu, I., & Genç, M. S., 2020. Experimental investigation of the ground effect on a wing without/with trailing edge flap, *Fluid Dynamics Research*, *52*(4), 045504.

Ozturk, N. A., Akkoca, A., and Sahin, B., 2008. Flow details of a circular cylinder mounted on a flat plate, *Journal of Hydraulic Research*, *46*(3), 344-355.

Prasad, R., and Damodaran, M., 2013. Computational Modelling of Steady and Unsteady Low-Speed Wing in Ground Effect Aerodynamics, In *51st AIAA Aerospace Sciences Meeting including the New Horizons Forum and Aerospace Exposition*, p. 497.

Payne, F. M., Ng, T., Nelson, R. C., and Schiff, L. B., 1988. Visualization and wake surveys of vortical flow over a delta wing, *AIAA Journal*, *26*(2), 137-143.

Pevitt, C., and Alam, F., 2014. Static Computational Fluid Dynamics simulations around a specialized delta wing, *Computers, and Fluids*, *100*, 155-164.

Sahin, B., Yayla, S., Canpolat, C., and Akilli, H., 2012. Flow structure over the yawed nonslender diamond wing, *Aerospace Science and Technology*, *23*(1), 108-119.

Qin, Y., Qu, Q., Liu, P., Tian, Y., and Lu, Z., 2015. DDES study of the aerodynamic forces and flow physics of a delta wing in static ground effect, *Aerospace Science and Technology*, *43*, 423-436.

Qin, Y., Liu, P., Qu, Q., and Guo, H., 2016. Numerical study of aerodynamic forces and flow physics of a delta wing in dynamic ground effect, *Aerospace Science and Technology*, *51*, 203-221.

Qu, Q., Lu, Z., Guo, H., Liu, P., and Agarwal, R. K., 2015. Numerical investigation of the aerodynamics of a delta wing in ground effect, *Journal of Aircraft*, *52*(1), 329-340.

Sahin, B., Akilli, H., Lin, J. C., & Rockwell, D., 2001. Vortex breakdown-edge interaction: a consequence of edge oscillations, *AIAA Journal*, *39*(5), 865-876.

Reuss, D. L., Adrian, R. J., Landreth, C. C., French, D. T., & Fansler, T. D., 1989. Instantaneous planar measurements of velocity and large-scale vorticity and strain rate in an engine using particle-image velocimetry, *SAE Transactions*, 1116-1141.

Sarpkaya, T., 1971. On stationary and traveling vortex breakdowns, *Journal of Fluid Mechanics*, *45*(3), 545-559.

Tumse, S., Tasci, M. O., Karasu, I., and Sahin, B., 2021. Effect of ground on flow characteristics and aerodynamic performance of a non-slender delta wing, *Aerospace Science and Technology*, *110*, 106475.

Taylor G. S. and Gursul I., 2004. Buffeting flows over a low-sweep delta wing, *AIAA Journal*, *42*(9), 1737-1745.

Taylor, G., Wang, Z., Vardaki, E., & Gursul, I., 2007. Lift enhancement over flexible nonslender delta wings, *AIAA Journal*, *45*(12), 2979-2993.

Tasci, M. O., Pektas, M. C., Tumse, S., Karasu, I., Sahin, B., and Akilli, H., 2021. The impact of the pitching motion on the structure of the vortical flow over a slender delta wing under sideslip angle, *Journal of Visualization*, *24*(3), 437-442.

Tasci, M. O., Karasu, I., Sahin, B., & Akilli, H., 2020. Investigation of crossflow features of a slender delta wing, *Wind and Structures*, *31*(3), 229-240.

The Aviation History Online Museum, 2015. Ground Effect in Aircraft, http://www.aviation-history.com/theory/ground_effect.htm.

Velte, C. M., Hansen, M. O., and Okulov, V. L., 2016. Multiple vortex structures in the wake of a rectangular winglet in ground effect, *Experimental Thermal and Fluid Science*, *72*, 31-39.

Visbal, M. R. (2004). Computational and physical aspects of UAV vortical flows. *Air Force Research Lab Wrıght-Patterson Afb Oh Air Vehıcles Directorate*.

Wentz Jr, W. H., & Kohlman, D. L., 1971. Vortex breakdown on slender sharp-edged wings, *Journal of Aircraft*, *8*(3), 156-161.

Yaniktepe, B., 2006. Origin and control of vortex breakdown of unmanned combat air vehicles, Doctoral dissertation, University of Cukurova.

Yayla, S., Canpolat, C., Sahin, B., & Akilli, H., 2013. The effect of angle of attack on the flow structure over the nonslender lambda wing, *Aerospace Science and Technology*, *28*(1), 417-430.

Yang, Z., Yang, W., and Li, Y., 2009. Analysis of two configurations for a commercial WIG craft based on CFD, in *27th AIAA Applied Aerodynamics Conference*, p. 4112.

Yun, L., Bliault, A., & Doo, J., 2010. WIG craft and ekranoplan. *Ground Effect Craft Technology*, *2*.

Zhang, X., Wang, Z., and Gursul, I., 2016. Interaction of multiple vortices over a double delta wing, *Aerospace Science and Technology*, *48*, 291-307.

Zhang, X., Wang, Z., and Gursul, I., 2017. Control of multiple vortices over a double delta wing. In *47th AIAA Fluid Dynamics Conference* (p. 4122).

CURRICULUM VITAE

Mehmet Oğuz TAŞCI graduated from Seyran Rotary Anatolian High School in Adana in 2007. He enrolled in the Mechanical Engineering Department of Çukurova University in Adana in 2008. He went to study at Duisburg-Essen University for the spring semester in Germany in 2012. He graduated from the Department of Mechanical Engineering in 2013 and began his Master of Science in 2014. He graduated with a Master of Science in 2017 and began his Philosophy of Doctorate in 2017. He took a role as a researcher in a TÜBİTAK project (114M497). He took two doctorate scholarships from YÖK (100/2000) and TÜBİTAK (2211/C). He is married with Gözde TAŞCI.